The Pennsylvania State University

The Graduate School

Department of Mechanical Engineering

NUMERICAL CHARACTERIZATION OF THE DISCHARGE COEFFICIENT IN CRITICAL NOZZLES

A Thesis in
Mechanical Engineering
by
Aaron N. Johnson

Submitted in Partial Fulfillment
of the Requirements
for the Degree of

Doctor of Philosophy

December 2000

We approve the thesis of Aaron N. Johnson

Date of Signature

Charles L. Merkle Professor of Mechanical Engineering Thesis Adviser Chair of Committee	
Thomas A. Litzinger Professor of Mechanical Engineering	
Anil K. Kulkarni Professor of Mechanical Engineering	
Lance R. Collins Professor of Mechanical Engineering	
Pedro I. Espina Leader of Fluid Flow Group at NIST	
Richard C. Benson Professor of Mechanical Engineering Head of the Department of Mechanical Engineering	

ABSTRACT

For several decades critical nozzles have played an important role in flow measurement science. These devices have been used extensively as gas flow transfer standards to perform inter-comparisons of the primary mass flow standards both internationally and domestically. When used for metrological applications, as well as for some industrial applications, the performance characteristics of critical nozzle flow meters have traditionally been determined by direct calibration against a primary mass flow standard. After calibration, the resulting uncertainty in mass flow is typically 0.25 % or less.

Since the early 1960's researchers have worked to develop closed-form quantitative predictive models in order to assist experimental calibration. These analytical techniques have served as a guide for nozzle design, helped to determine the appropriate calibration parameters, and have proven to be useful for applications where slightly larger error levels are tolerable. Furthermore, these methods have frequently been applied in situations where experimental techniques are prohibitively difficult (*e.g.*, the measurement of toxic or corrosive gases).

Analytic methods for predicting the mass flow passing through a critical nozzle are based on one-dimensional inviscid flow theory as applied to perfect gases. The predicted mass flow is then ameliorated by adding corrections to account for the following physical mechanisms: (1) boundary layer development along the nozzle wall,

(2) the presence of multi-dimensional flow field (*i.e.,* the flow field is not truly one-dimensional), and (3) real gas behavior. This thesis identifies a new mechanism, not previously considered, that affects the mass flow of certain gases (*e.g.,* CO_2 and SF_6) flowing through geometrically small-scale critical nozzles. Specifically, vibrational relaxation effects are shown to affect the discharge coefficient of certain gases by nearly 3 %, an amount too large to be neglected for high accuracy gas flow metrology.

Prior to the vibrational relaxation explanation provided in this thesis, unexplained discrepancies of more than 2 % had existed between traditional analytical models and the calibration data of some gases. A first principles mathematical model was developed by combining molecular theory with gas dynamic processes to account for vibrational relaxation phenomena. Comparison with experimental data indicates that this model predicts the mass flow of gases affected by vibrational non-equilibrium states (*e.g.,* CO_2 and SF_6) and gases unaffected by vibrational non-equilibrium states (e.g., N_2, H_2, O_2, Ar) equally well, to better than 0.4 % of reading. Vibrational non-equilibrium phenomena largely explains the gas *species effect* observed in calibration data, whereby seemingly similar gas species have calibration characteristics that differ by more than 3 % The vibrational non-equilibrium model was validated by two independent experiments, one which varied the flow residence time and the other which varied the vibrational relaxation time of CO_2 gas.

TABLE OF CONTENTS

LIST OF FIGURES

LIST OF TABLES

0.1 Nomenclature

a	sound speed
A	area
C_s	critical flow factor
C_d	discharge coefficient
c_P	specific heat at constant pressure
d	nozzle throat diameter
e	total energy per unit volume, $= \rho[\epsilon + \frac{1}{2}(u_x^2 + u_r^2)]$
E	inviscid flux vector, $= [\rho u_x \ \rho u_x^2 + p \ \rho u_x u_r \ (e+p)u_x]$
F	inviscid flux vector, $= [\rho u_r \ \rho u_r u_x \ \rho u_r^2 + p \ (e+p)u_r]$
g_k	degeneracy for the k^th vibrational mode
H	axisymmetric source vector
k	thermal conductivity
L	viscous operator (see Section 2.2)
$\dot{m}$	mass flow rate
MW	molecular weight
n	normal direction
N	number of vibration degrees of freedom
p	pressure
Pr	Prandtl number, $= \mu c_P / k$

q''	heat flux vector
Q_c	conservative vector, $= [\rho\ \rho u_x\ \rho u_r\ e]^T$
Q_p	solution vector, $= [p\ u_x\ u_r\ T]^T$
r	radius or radial coordinate
R	nozzle throat radius, = d/2
R_c	radius of curvature at nozzle throat
Re	Reynolds number based on diameter
R_{gas}	gas constant, $= R_u/MW$
R_{u}	universal gas constant
R_{xx}, R_{xr}, R_{rx}, R_{rr}	viscous matrices (see Section 2.2)
R_{xx}	viscous matrix (see Section 2.2)
R_{xr}	viscous matrix (see Section 2.2)
R_{rx}	viscous matrix (see Section 2.2)
R_{rr}	viscous matrix (see Section 2.2)
T	temperature
x	axial coordinate
u_r	fluid velocity in the r-direction
u_x	fluid velocity in the x-direction
U_r	experimental expanded uncertainty
Z	compressibility factor

α	inviscid discharge coefficient
β	magnitude of the slope of the calibration curve
γ	specific heat ratio
δ_{th}	thermal boundary layer thickness
δ^*	displacement thickness
ϵ	internal energy
ϵ_{vib}	molecular vibrational energy
η	coordinate in body fitted coordinate system
θ	half angle of nozzle divergent section, = 0.05236 radians, (3^o)
θ_k	vibrational temperature for the k^th vibrational mode
μ	molecular viscosity
ξ	coordinate in body fitted coordinate system
ρ	density
τ	shear stress tensor
τ_{res}	flow residence time
τ_{vib}	vibrational relaxation time
Γ	ratio of vibrational relaxation time to flow residence time, $= \tau_{vib}/\tau_{res}$
Υ	Jacobian matrix, $= \partial Q_c/\partial Q_p$
Ω	ratio of throat radius to radius of curvature, $= R/R_c$

Subscripts

amb	ambient conditions outside nozzle configuration
adia	adiabatic wall condition
hot	constant wall temperature equal to ambient temperature
ideal	based on one dimensional inviscid analysis
o	stagnation condition
real	based on experimental data
wall	conditions at the wall

Superscripts

eq	thermodynamic equilibrium
$*$	conditions at throat assuming one-dimensional inviscid flow

Chapter 1

INTRODUCTION

The ability to measure flow reliably is essential for sustaining many existing technologies in aerospace, chemical processing, the automotive industry, the semiconductor industry, the biotechnology industry, utilities, etc [1]. Moreover, technological advancements and heightened industrial growth within the United States and internationally has created an ever increasing need to improve accuracy and reliability of flow measurements. More than 40 % of a typical company's capital expenditure on instrumentation is dedicated to flow measuring technologies [2]. As a result, the flow metering industry is expanding, producing in excess of three billion dollars worth of flow meters annually [3]. The accuracy and reliability of these flow meters have direct ramifications on process control for numerous industrial flow applications, on health and safety issues for flow of hazardous or toxic fluids, and on custody transfer for the exchange of valuable fluids [4]. In addition, flow metering accuracy and reliability can also have a significant economic impact. For example, of the two trillion dollars spent annually world wide on natural gas consumption, metering uncertainties are estimated to result in more than 60 billion dollars being unaccounted for each year. Therefore, to help ensure that flow meters provide reliable measurements, national metrology institutes (NMI's) have been established [5].

NMI's bear the responsibility of maintaining and disseminating flow measurement standards, as well as conducting research that supports advances in flow measurement standards [6]. One way that an NMI helps ensure reliable flow measurements is by calibrating (less accurate) flow meters to devices referred to as *primary flow standards* [7], [8]. Primary flow standards are devices that measure mass flow at the lowest levels of uncertainty without requiring calibration by another device. These devices achieve their low uncertainties by invoking global mass conservation principles to relate mass flow to the fundamental quantities of length, mass, and time. Traditionally, primary mass flow measurements have been conducted using any one of a number of well documented timed-collection techniques, whereby the quantity of fluid being measured flows into a collection vessel of known volume or mass for a measured time interval.

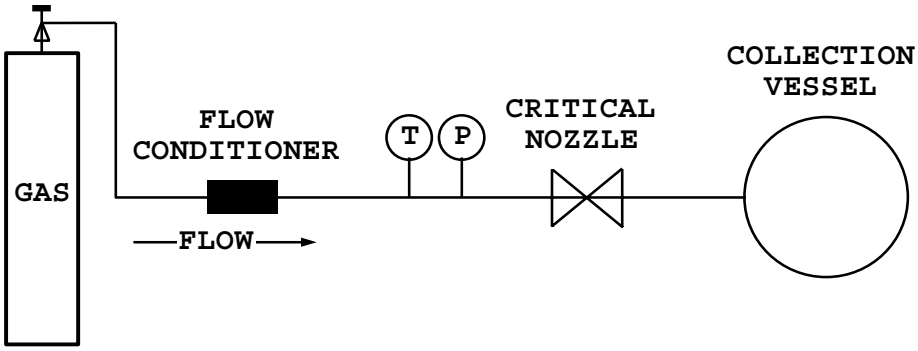

Figure 1.1. Schematic of typical primary standard calibration system

The basic components of a timed-collection primary mass flow standard consist of a source of gas flow, the meter under test (*e.g.,* critical nozzle), a collection vessel to store the collected gas, connecting piping, pressure and temperature instrumentation,

and data acquisition devices. A generic schematic illustrating these features is shown in Fig. (1.1). During calibration, gas passing through the flow meter under test accumulates into the collection tank. The mass flow is determined by dividing the mass accumulated in the tank by the duration of collection. An expression for the mass flow is given by

$$\dot{m}_{exp} = \frac{m_{tank_f} - m_{tank_i}}{\Delta t} \tag{1.1}$$

where m_{tank_i} is the initial mass in the tank, m_{tank_f} is the mass in the tank after collection, and Δt is the duration of the collection. We note that additional corrective terms (*e.g.,* diverter error, storage effects, possible leaks, etc.) may need to be included in Eq. (1.1) depending on the particular calibration standard.

Timed-collection primary standards are classified as either volumetric or gravimetric depending on the method used to quantify the mass of gas before and after collection (*i.e.,* m_{tank_i} and m_{tank_f}). Common volumetric primary standards include piston provers [9], bell provers [10], [11], and pressure-volume-temperature-time (PVTt) systems [12]. Volume based methods determine the gas density via temperature and pressure measurements, and calculate mass by multiplying the density by the volume of collected gas. Gravimetric timed-collection techniques [13], on the other hand, weigh the collection vessel before and after collection to determine the mass of gas. Using the existing volumetric and gravimetric timed-collection primary flow standards NMI's can measure mass flow with uncertainties ranging from as low as 0.01 % to 0.25 %.

The statement of flow measurement uncertainty specifies the maximum expected deviation from the true value at a ninety-five percent confidence level [14]. It is determined by statistically combining all of the relevant sources of error for a given primary flow standard (*e.g.,* measurement of time, flow profile effects, etc.).

The measurement of flow is unique from the measurement of other fundamental quantities such as mass, length, and time. For example, while the measurement of length has a standard reference that can be compared to measured values of length, no standard reference for flow measurements has been established. Therefore, NMI's conduct ongoing inter-comparisons among themselves to validate flow measurement uncertainty estimates. These round-robin testing procedures have helped identify systematic errors in primary flow standards, thereby reducing flow measurement uncertainty. Because critical nozzle flow meters have been used for several decades to perform the vast majority of these comparisons, the detailed flow characteristics of these devices are of great importance.

Critical nozzles (also known as critical flow venturis) have unique flow features that distinguish them from other standard flow meters. Not only do these devices provide a reliable and precise way of measuring gas mass flow, but they are easily portable, robust, offer a high degree of repeatability, and have been demonstrated to stably maintain their calibration performance for a period of up to thirty years [15]. As a result these devices have traditionally been used for performing international comparisons among NMI's and for disseminating flow traceability from NMI's to secondary

laboratories domestically [16]–[18]. In addition, these devices have numerous industrial applications including uses as gas flow meters, mass flow controllers, calibration standards for other gas flow meters [19],[20], and pressure isolators.

In light of the unique flow features of critical nozzles, various NMI's are investigating the possibility of using these devices as a primary flow standard (for direct measurement of flow without prior calibration). We note that there is no intention of replacing the more accurate timed-collection primary standards with critical nozzles. Instead, the purpose is to exploit the unique features offered by critical nozzles in flow applications not suitable or convenient for the more traditional timed-collection methods. For example, a critical nozzle flow standard would have great benefit for metering gases that are either too toxic or corrosive for traditional (timed-collection) methods. Additional applications include the measurement of extremely large flows where existing timed-collection methods require very large collection vessels, the measurement of very low flows where collection times for flow accumulation into the collection vessel can be impractically lengthy, and metering applications not requiring the absolute lowest levels of uncertainty.

The main obstacle preventing the wide spread use of critical nozzles as a primary flow standard can be attributed to their dependence on calibration for accuracy. To achieve the highest levels of accuracy each nozzle must be calibrated over its expected range of operating conditions. Moreover, the calibration is sensitive to gas species (especially in the lower Reynolds number range) so that each nozzle must be

re-calibrated whenever a different gas is used. To determine the mass flow without calibration, quantitative predictive models have been developed. These predictive models work quite well at larger flows (*i.e.,* larger nozzle sizes) where existing analytical theories predict the discharge coefficient to within the experimental uncertainty. However, at lower flows current predictive models deviate from experimental data by as much as 2 % – an error margin well beyond the acceptable limits for high accuracy gas flow metrology.

The objective of this research is to develop a highly accurate first principles predictive model to use as the basis for critical nozzle flow calibration. For timed-collection primary standards the analysis of mass flow is straightforward, yielding an expression for mass flow equal to the change of mass in the collection vessel divided by the elapsed collection time (refer to Eq. 1.1). In contrast, a first principles evaluation of the mass flow through a critical nozzle is more involved, requiring a detailed analysis that conserves mass, momentum, and energy at all locations throughout the nozzle. Ultimately, an evaluation of mass flow through a critical nozzle based on first principles requires solving the governing conservation equations in conjunction with the appropriate boundary conditions.

In this research computational fluid dynamics (CFD) will be used in conjunction with experimental methods to study the detailed flow characteristics of small-scale critical nozzles. We will assess the ability of CFD to improve upon long standing analytical models [21]–[36] that work well for some gases (*i.e.,* within 0.5 % of reading),

but deviate by as much as 2 % for others. Given that primary mass flow standards have uncertainties ranging from 0.01 % to 0.25 %, the proposed CFD model will focus on obtaining mass flow predictions at precision levels better than 0.25 % of data.

Improvements to existing analytical models will be accomplished by including more of the pertinent physics (*i.e.,* wall heat transfer, real gas effects, more physical inlet conditions, possible non-equilibrium effects, etc.) which should further improve the agreement between model and experiment. Thus, the proposed CFD model will include a more complete description of important gas dynamic flow processes which might improve the state of critical nozzle flow measurement, ultimately allowing these devices to be used more reliably over a wider range of gas species and operating conditions. Although the Reynolds number based on nozzle diameter in these flows is relatively high, ranging from 2 000 to 131 000, experimental evidence indicates that the boundary layer remains laminar for Reynolds numbers up to 10^6 [37]. As a result the numerical model discussed in this research is based on laminar flow.

1.1 Critical Nozzle Geometry

The critical nozzle has two prominent designs [39], the toroidal throat nozzle design (Fig. 1.2) and the cylindrical throat nozzle design (Fig. 1.3). Although the overall shape of both designs is that of an axisymmetric converging-diverging nozzle, the nozzle contour differs between the two geometries. An azimuthal cut of the first design installed in a pipeline is shown in Fig. (1.2). The converging section is a

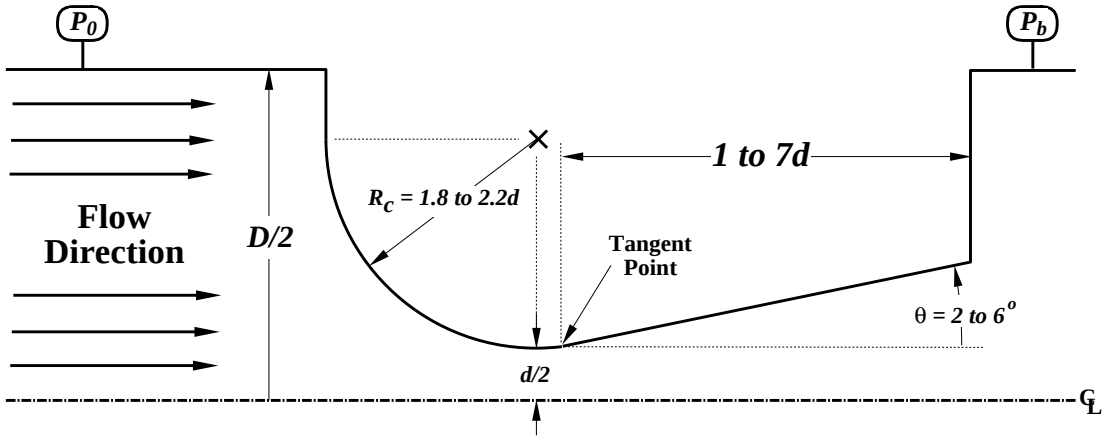

Figure 1.2. Schematic of toroidal throat critical nozzle geometry in pipeline: D = approach pipe diameter, d = nozzle throat diameter, θ = half angle of conical divergent section.

circular arc of constant curvature contracting to a minimum cross sectional area called the nozzle throat. This circular arc extends past the throat to a point of tangency where the shape becomes conical. The second design shown schematically in Fig. (1.3) also consists of a constant curvature converging section. The principle difference is that its minimum cross sectional area extends for one nozzle throat diameter before discontinuously changing slope at the location where the conical divergent section begins.

In past years the extended throat section in the cylindrical design allowed highly accurate measurements of the nozzle throat diameter – an important parameter in analytical and computational predictions of the discharge coefficient. However, due to ongoing advances in computer controlled machining, the throat diameter can be determined to within $\pm 1\,\mu$m in the first design (*i.e.,* toroidal throat geometry) [34]. The toroidal throat geometry avoids both the undesirable discontinuity in the nozzle

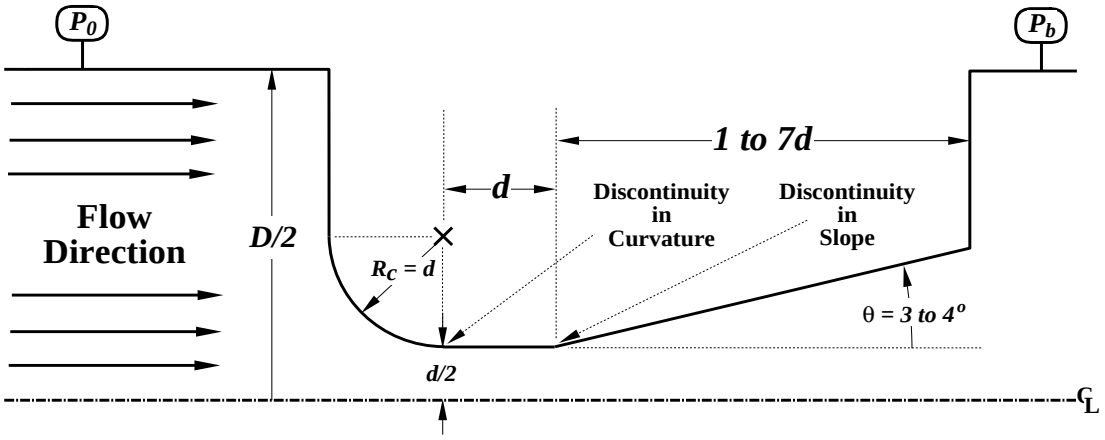

Figure 1.3. Schematic of cylindrical throat critical nozzle geometry in pipeline: D = approach pipe diameter, d = nozzle throat diameter, θ = half angle of conical divergent section.

wall curvature at the end of the converging section as well as the constant area section (compare Fig. 1.2 with Fig. 1.3). As pointed out by Smith and Matz [29], the discontinuous jump to the infinite curvature at the end of the converging section in the cylindrical nozzle results in a locally adverse pressure gradient that will at a minimum thicken the boundary layer, or could possibly even lead to local flow separation. Either of these conditions results in non-ideal nozzle performance and is undesirable, especially if predictive methods are to be used. However, in spite of the disadvantages associated with the cylindrical throat nozzle design, both nozzle designs are used in practice.

In the present research we consider both nozzle designs, but place more emphasis on the toroidal throat design. The nozzle sizes considered have throat diameters ranging from 0.3 mm to 3 mm. The stagnation pressure is varied from 0.5 atm to 3 atm for a nominal stagnation temperature of 298.15 K. This range of operating conditions

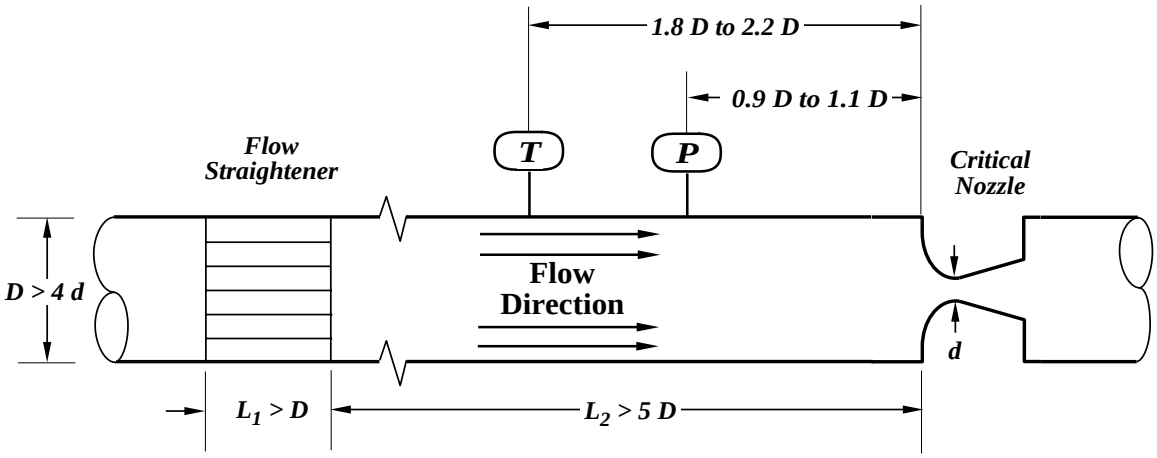

Figure 1.4. Schematic illustrating flow conditioning and static pressure and temperature measurements upstream of a toroidal throat critical nozzle.

corresponds to a mass flow range extending from 0.5 grams/min to 220 grams/min spanning a Reynolds number range from 2 000 to 131 000.

To promote uniformity in the flow metering community, the geometry of both nozzle designs has been standardized by the International Organization for Standardization (ISO) [39]. In addition, the ISO has developed specific requirements for installing critical nozzles into pipelines. These ISO guidelines require that the static pressure be measured using a wall pressure tap located 0.9 to 1.1 pipe diameters upstream of the nozzle entrance and that the temperature be measured 1.8 to 2.2 pipe diameters upstream of the nozzle entrance as shown in Fig. (1.4). Also, a flow straightener is suggested upstream of both the pressure and temperature measurements to minimize installation effects.

1.2 Principle of Operation

During operation of a critical nozzle, subsonic flow in the pipeline upstream of the nozzle inlet must be accelerated to sonic velocity at some location within the nozzle. Based on idealized flow conditions (*i.e.,* one-dimensional inviscid flow of a calorically perfect gas) the one-dimensional gas flow reaches sonic conditions (*i.e.,* $M = 1$) uniformly across the nozzle throat cross section. In the actual multi-dimensional flow field, however, the sonic line is not flat, but has a definite curvature that is related to the nozzle wall radius of curvature at the throat. In either case, once the flow has been accelerated to sonic conditions the flow is commonly referred to as *choked* or *critical* flow, giving rise to the name critical nozzle.

Choked flow is attained by setting the appropriate ratio of back pressure to inlet stagnation pressure (*i.e.,* p_b/p_0) across the nozzle. The level of back pressure ratio that just chokes the nozzle is the maximum allowable pressure ratio to maintain sonic throat conditions, and care must be taken to operate critical nozzles at or below this value. Once the appropriate (choking) pressure ratio is obtained, further reduction of the downstream pressure (*i.e.,* back pressure) propagates a shock structure through the divergent section of the nozzle but has little to no effect on mass flow rate. Physically, the downstream pressure disturbances cannot propagate upstream against the oncoming supersonic flow. Therefore, critical nozzles, unlike many other flow meters, do not need to measure a pressure drop to determine the flow rate. Given the

nozzle geometry and gas composition, critical nozzles have the advantage (at least to first order) of determining the mass flow rate based on upstream stagnation properties alone.

The ratio of the cross sectional area at the meter exit, A_{exit}, to the throat cross sectional area, A^*, dramatically affects the necessary level of the choking pressure ratio. In particular, critical nozzles with larger area ratios, A_{exit}/A^*, have better pressure recovery (*i.e.,* less pressure drop) and allow higher choking pressure ratios, thereby extending the range of operation (especially in pressure limited systems). Since ISO critical nozzles are designed for a fixed range of divergent half angles (see Fig. 1.2), these nozzles take advantage of this principle by having a lengthy divergent section.

An example that illustrates how A_{exit}/A^* affects the choking pressure is considered for N_2 gas. Based on ideal flow theory the choking pressure ratio for N_2 flow through a critical nozzle without a divergent section (*i.e.,* $A_{exit}/A^* = 1$) is approximately 0.523. However, the choking pressure can be increased to approximately 0.9 by implementing an area ratio, $A_{exit}/A^* = 1.62$, which corresponds to a divergent section length of 3.94 nozzle throat diameters and a divergent half angle of 2 degrees. From a practical viewpoint, however, the choking pressure will also be a function of Reynolds number since viscous effects degrade the choking pressure ratio, causing it to be somewhat lower than the idealized value based on area ratio.

1.3 One Dimensional Inviscid Mass Flow Model

A first approximation of the mass flow passing through a choked nozzle can be obtained analytically by solving the one-dimensional Euler equation for a given nozzle geometry. When the gas is assumed to be a calorically perfect ideal gas (*i.e.,* $c_p = constant$ and $p = \rho R_{gas} T$) the choked nozzle mass flow is given by the following relationship

$$\dot{m}_{ideal} = \frac{p_0 A^* C_{s_{ideal}}}{\sqrt{R_{gas}\ T_o}} \tag{1.2}$$

$$C_{s_{ideal}} = \sqrt{\gamma}\left(\frac{\gamma+1}{2}\right)^{\frac{(\gamma+1)}{2(1-\gamma)}}$$

where p_0 is the stagnation pressure, T_o is the stagnation temperature, A^* is the nozzle throat area, R_{gas} is the gas constant for a specified gas composition, and $C_{s_{ideal}}$ is the *ideal* critical flow factor – a function of the specific heat ratio, γ. In the present work the model for mass flow given in Eq.(1.2) will be referred to as the *ideal* flow model as indicated by the subscript in the equation. The details giving the formulation of Eq.(1.2) can be found in standard textbooks of gas dynamics [40]–[42].

The *ideal* mass flow model given by the expression in Eq.(1.2) provides a convenient first order estimate of the actual mass flow through a critical nozzle (*i.e.,* 1–10 % of

reading depending on Reynolds number). Better agreement between theory and experiment can be obtained by incorporating into the theory various *non-ideal* flow mechanisms that affect the actual mass flow. Traditionally, these non-ideal flow mechanisms have included viscous effects, multi-dimensional phenomena, and real gas behavior. In Section 1.5 we will address the mathematical details involved in incorporating these non-ideal effects into theoretical model. Essentially, we will demonstrate that the net effect of these *non-ideal* flow mechanisms is to add higher order correction terms to the *ideal* mass flow prediction given in Eq.(1.2). In the remainder of this section, however, we focus on providing qualitative insight as to how each of these traditional (*i.e.,* non-ideal) flow mechanisms affects the mass flow.

The presence of viscous effects in the nozzle tends to decrease the mass flow below its ideal value given in Eq.(1.2). Physically, the no slip condition existing at the nozzle wall results in a layer of slow moving fluid adjacent to the wall (*i.e.,* the boundary layer). Furthermore, within the boundary layer the fluid's kinetic energy is irreversibly converted to internal energy (*i.e.,* viscous dissipation) so that the boundary layer temperature is larger than the free stream temperature. The larger temperature throughout the boundary layer results in a decrease in the fluid density near the wall. Together, the lower than ideal values of fluid velocity and density in the boundary layer result in a reduction in mass from that predicted by the one-dimensional inviscid flow solution. Generally speaking, the accuracy of the ideal mass flow predictions improves at larger Reynolds numbers since viscous effects are less significant.

The *ideal* flow model approximates the nozzle flow as a one-dimensional flow field. In actuality, the nozzle flow is multi-dimensional. These multi-dimensional effects result in curvature of the sonic line which also reduce the actual mass flow relative to $\dot{m}_{ideal}$. In multi-dimensional flows (neglecting viscous effects) the sonic line follows an approximately parabolic profile that begins just upstream of the throat along the nozzle wall and extends downstream into the diverging section of the nozzle to its vertex on the centerline. Consequently, flow at the throat cross section will have, in general, a supersonic velocity near the wall (*i.e.,* $M > 1$), and a subsonic velocity near the centerline (*i.e.,* $M < 1$). On the other hand, the sonic line is flat for one-dimensional inviscid flow so that a uniform sonic velocity (*i.e.,* $M = 1$) exists everywhere along the throat cross section. Based on isentropic flow theory, the mass flux obtains its maximum value at a Mach number of unity. Therefore the mass flow is greater for one-dimensional flow where sonic conditions (*i.e.,* $M = 1$) exist uniformly across the throat cross section.

In contrast to the reduction in mass flow due to viscous and multi-dimensional effects, the presence of real gas behavior (*i.e.,* non unity compressibility factor) in the flow can either increase the mass flow above the ideal value given in Eq.(1.2) or decrease the mass flow below the ideal value. The effect that real gas behavior will have on the mass flow is determined primarily by the compressibility factor, Z. Under ideal conditions the compressibility factor is unity. However, Z varies with the local thermodynamic conditions in the actual flow. Roughly speaking, the compressibility

factor of gases generally obtains larger than unity values at large pressures and less than unity values at low pressures. For most critical nozzle applications the compressibility factor is less than unity (*i.e.,* $Z < 1$) throughout the flow field since the nozzle upstream stagnation pressure is typically well less than the critical pressure[1] of the gas. Therefore, for $Z < 1$ the actual gas density throughout the nozzle will be larger than the idealized value so that the mass flow is typically increased above $\dot{m}_{ideal}$.

For applications requiring better accuracy than the ideal flow model can provide, the mass flow can either be measured experimentally or determined by more complete mathematical models. Generally speaking, experimental calibration offers advantages over mathematical models given that the experimental errors can be estimated to yield an overall expanded uncertainty for the procedure [14]. For mathematical models, on the other hand, fewer quantitative methods exist for estimating errors resulting from any required simplifying assumptions. Nevertheless, mathematical models are useful, and often serve as a guide to experimental calibration as well as provide physical insight into the processes that cause deviations from ideal behavior. Before discussing the first principles numerical (CFD) calibration procedures, we briefly discuss standard experimental calibration procedures (Section 1.4) and review the existing analytical techniques for calibration (Section 1.5).

[1]Here the critical pressure is the highest pressure under which a liquid can exist in equilibrium with its vapor (*i.e.,* not the nozzle throat pressure).

1.4 Experimental Calibration

Calibration supplements the one-dimensional inviscid flow theory by defining an experimentally determined discharge coefficient. The discharge coefficient is given by

$$C_d \equiv \frac{\dot{m}_{exp}}{\dot{m}_{ideal}} \tag{1.3}$$

where $\dot{m}_{ideal}$ is obtained from the one-dimensional inviscid analysis given by Eq.(1.2), and $\dot{m}_{exp}$ is measured experimentally using any of the previously discussed primary flow standards. Given that the accuracy of critical nozzles derives from experimental calibration, we briefly discuss the calibration procedure and provide as an example typical calibration data.

For a given nozzle geometry, the discharge coefficient changes as a function of the flow rate passing through it. Traditionally, this functionality has been expressed in terms of a reference Reynolds number defined as [31]

$$Re^*_{\rm exp} = \frac{4\,\dot{m}_{\rm exp}}{\pi\, d\, \mu_0} \tag{1.4}$$

where d is the nozzle throat diameter, and μ_0 is a representative viscosity. Since the magnitude of viscosity varies throughout the flow field, custom is to evaluate the viscosity at the upstream stagnation conditions. During calibration the Reynolds number is usually controlled by adjusting the upstream stagnation pressure at a fixed

stagnation temperature. The mass flow is measured at the desired Reynolds number and Eq. (1.3) is used to define the discharge coefficient. A calibration curve (*i.e.,* a plot of $Re^*_{\rm exp}$ vs. C_d) is generated by repeating this procedure at several stagnation pressures. We note that in analytical work it is more convenient to plot the discharge coefficient versus an ideal version of the Reynolds number. The ideal version of the Reynolds number, $Re^*_{\rm ideal}$, is defined by using the idealized mass flow, $\dot{m}_{ideal}$, in the place of $\dot{m}_{exp}$ in Eq. (1.4), and the discharge coefficient, $C_d = Re^*_{\rm exp}/Re^*_{\rm ideal}$ provides the conversion factor between the two Reynolds number definitions.

Figure (1.5) gives an example of experimental calibration data taken by Nakao *et al.* [35] at the National Research Laboratory of Metrology in Japan (NRLM) for several gases flowing through a small throat diameter (*i.e.,* $d = 0.5935\,$mm) critical nozzle at Reynolds numbers in the laminar flow range. For all the gases shown in the figure, the discharge coefficient increases with increasing Reynolds number. Physically, as the Reynolds number increases the boundary layer thins and the discharge coefficient increases. At infinite Reynolds numbers, the discharge coefficient approaches its limiting value of unity.

The size of the symbols used in this Fig. (1.5) is indicative of the 0.2 % experimental uncertainty. The nearly 3 % variation of data among the different gas species (*e.g.,* CO_2 and He) indicates that C_d has a functional dependence on gas species and is not fully characterized by Reynolds number alone. Thus, a more complete characterization of C_d must include additional parameters that account for this gas species

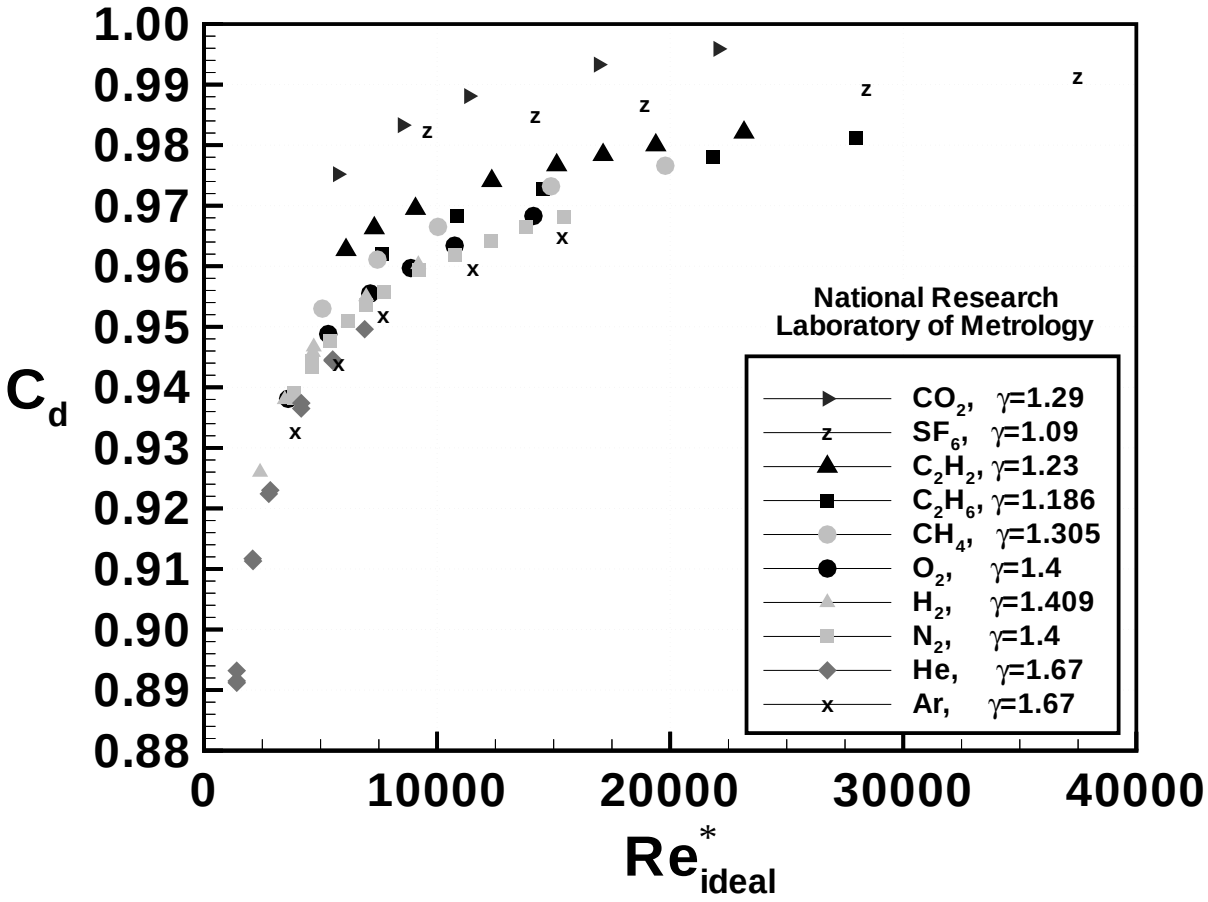

Figure 1.5. NRLM experimental calibration data for several gas species.

effect. Therefore, although experimental calibration procedures enable high accuracy gas mass flow measurements, the resulting calibration curve can only be applied to the specific critical nozzle geometry and gas composition used during calibration.

1.5 Existing Analytical Models

In an effort to diminish the need for calibration, previous research has focused on the development of more complete analytical models capable of predicting nozzle

performance at improved levels of accuracy and providing a better understanding of flow field characteristics. Various researchers [21]–[34] have developed corrections for multi-dimensional effects, viscous effects, and real gas behavior that characterize the discharge coefficient over a wide range of operating conditions as a function of various physical parameters. This section will discuss the theoretical basis and limitations of various analytical models that have been used to predict the discharge coefficient.

Much of the pertinent physics required to make reasonably accurate mass flow predictions for critical nozzle applications is contained within the one-dimensional inviscid flow model (discussed previously in Section 1.3). This fact is evident in the vast majority of published calibration data where the ratio of $\dot{m}_{exp}$ to $\dot{m}_{ideal}$ (*i.e.,* C_d) is between 0.9 and 1.0. As a result, the standard analytical approach for including non-ideal effects uses the ideal flow model (*i.e.,* one-dimensional inviscid flow of a calorically perfect gas) as a baseline. Corrections for non-idealities due to multi-dimensional effects, viscous effects, and real gas behavior are considered as higher order terms that are subtracted from the baseline. Accordingly, the discharge coefficient can be expressed as

$$C_d = 1 - \Delta C_{d_{inv}} - \Delta C_{d_{vis}} - \Delta C_{d_{virial}} \tag{1.5}$$

where $\Delta C_{d,inv}$ is the reduction in C_d due to multi-dimensional effects, $\Delta C_{d_{vis}}$ is the reduction in C_d due to viscous effects, and $\Delta C_{d_{virial}}$ is the reduction (or gain) in C_d due to real gas behavior. Given that each of the first order corrective terms in

Eq. (1.5) is generally small relative to the (unity) baseline, higher order products of these terms usually make a negligible contribution and can be omitted.

The mathematical expression for the discharge coefficient in Eq. (1.5) treats viscous effects, multi-dimensional effects, and real gas behavior as uncoupled phenomena. The combined effect of these non-ideal mechanisms is modeled as a superposition of the individual effects. As a result, each of these non-ideal mechanisms can be analyzed independently from the influence of the other mechanisms. For example, because no coupling is assumed to exist among the non-ideal flow mechanisms, the reduction in C_d due to viscous effects can be expressed as the difference between the unity baseline and a viscous discharge coefficient, $C_{d_{vis}}$. Following this reasoning, $C_{d_{vis}}$ is determined by considering the boundary layer development along the nozzle wall, but neglecting sonic line curvature and real gas behavior. Analogously, an inviscid discharge coefficient, $C_{d_{inv}}$, and a real gas or virial discharge, $C_{d_{virial}}$, can be defined to characterize multi-dimensional effects and real gas behavior respectively. Mathematically, the reduction (or gain) in C_d due to each non-ideal mechanism is given by the following three expressions:

1. $\Delta C_{d_{vis}} = 1 - C_{d_{vis}}$

2. $\Delta C_{d_{inv}} = 1 - C_{d_{inv}}$

3. $\Delta C_{d_{virial}} = 1 - C_{d_{virial}}$

By substituting these definitions into Eq. (1.5) the discharge coefficient can be expressed as

$$C_d = 1 - (1 - C_{d_{inv}}) - (1 - C_{d_{vis}}) - (1 - C_{d_{virial}}). \tag{1.6}$$

A similar equation was derived by Massier *et al.* in 1970 [32]. These researchers considered viscous effects and multi-dimensional effects and derived a form of Eq. (1.6) valid for calorically perfect ideal gases. Since real gas effects were not considered, their expression for the discharge coefficient includes only the first three terms on the right hand side of Eq. (1.6). Their analysis can be extended, however, to reproduce Eq. (1.6) in its entirety by assuming that real gas effects are limited to the inviscid core region. That is, corrections for real gas effects predominately affect the core flow. The validity of this assumption is predicated upon the core flow passing through a much larger area with a higher mean flow velocity than the flow inside the boundary layer.

Throughout the years several other researchers have chosen to express Eq. (1.6) in an equivalent form whereby the discharge coefficient is conveniently expressed as a product of the various non-ideal discharge coefficients

$$C_d = C_{d_{inv}} C_{d_{vis}} C_{d_{virial}}. \tag{1.7}$$

A Taylor series expansion around the baseline (*i.e.,* unity) shows that this expression is equivalent to Eq. (1.6) to second order accuracy.

Based upon Eq. (1.6) or Eq. (1.7), the analytic characterization of C_d reduces to determining a discharge coefficient for each non-ideal effect relative to the baseline. This uncoupled approach is valid when non-ideal mechanisms cause only small deviations from the baseline. Deviations due to real gas behavior will be small when the compressibility factor is near unity. Likewise, corrections for viscous effects will be small when the boundary layer at the nozzle throat is small in comparison to the throat radius. This criteria is satisfied by most high Reynolds numbers flows, with the exception of flows through small-scale critical nozzles where even a thin boundary layer may represent a non-negligible fraction of the throat radius. Such small flows are typical in certain semi-conductor manufacturing applications that use critical nozzle flow meters to control mass flow. Multi-dimensional phenomena will be small when the throat radius of curvature is large relative to the throat diameter (*i.e.,* at least two throat diameters). In the remainder of this section we discuss the methods developed by previous researchers for determining $C_{d_{inv}}$, $C_{d_{vis}}$, and $C_{d_{virial}}$.

1.5.1 Inviscid Discharge Coefficient

Several researchers [26]–[28] have developed closed form analytical expressions for the inviscid discharge coefficient, $C_{d_{inv}}$. Essentially, these formulations correct the ideal baseline model by accounting for curvature of the sonic line attributed to a multi-dimensional flow field. These corrections express the inviscid discharge coefficient, $C_{d_{inv}}$, as a function of γ and $\Omega = R/R_c$ where R is the throat radius and

R_c is the wall radius of curvature at the nozzle throat. The functional dependence of the inviscid discharge coefficient on these parameters is determined by using a perturbation expansion solution of the compressible perturbation-velocity potential flow equation [41] in the transonic regime. Among several works, the most widely used solution is due to Hall [28] who solved the equation in axisymmetric coordinates by implementing a series solution of four terms. In Hall's expression the inviscid discharge coefficient is expressed as

$$C_{d_{inv}} = 1 - (\gamma + 1)\Omega^2 \left(\frac{1}{96} + \frac{8\gamma + 21}{4608}\Omega + \frac{754\gamma^2 + 1971\gamma + 2307}{552960}\Omega^2 \right) \tag{1.8}$$

where each successive term enclosed in the brackets of Eq. (1.8) adds an additional level of refinement. Theoretically, an infinite number of these corrective terms is necessary to obtain an exact analytical solution. However, truncating the series is justified for Ω less than unity since higher order terms contain larger powers of Ω and therefore become smaller. In contrast, the series diverges for Ω greater than unity so that solutions may be less accurate for Ω slightly greater than unity and are invalid for Ω significantly greater than unity. In accordance with ISO specifications toroidal throat critical nozzles are designed with $\Omega = 0.25$. Lastly, these series solutions have been found to be in good agreement with the work of Stratford [26] who used physical arguments to estimate how the wall curvature at the throat influences the inviscid discharge coefficient.

1.5.2 Viscous Discharge Coefficient

Previous researchers [26, 31, 33] have also studied how viscous phenomena affect the mass flow through critical nozzles. Viscous effects can be accounted for by defining an *effective* throat area in such a manner that the mass flow predicted by one-dimensional inviscid flow theory is equivalent to the actual value of mass flow through the nozzle. Given that viscous effects retard the flow near the wall, the effective area will be smaller than the actual throat area.[2] Mathematically, the effective throat radius equals the actual throat radius minus the displacement thickness, δ^*. One-dimensional inviscid flow theory can be used to determine the viscous mass flow once the nozzle wall is displaced inward by δ^*. Given that the density and flow velocity at the sonic throat are independent of the throat size, the viscous discharge coefficient can be defined as the ratio of the effective nozzle throat area to the actual nozzle throat area so that

$$C_{d_{vis}} = \left(1 - 2\frac{\delta^*}{d}\right)^2 . \tag{1.9}$$

where δ^* is the displacement thickness and d is the nozzle throat diameter. To maintain consistency with the previous assumption that viscous effects cause only a small deviation from the baseline, it is necessary that the ratio of the displacement thickness to diameter in Eq. (1.9) be small (*i.e.*, $\delta^*/d << 1$). Most researchers take advantage of this by neglecting the second order term in δ^*/d in Eq. (1.9) and express the viscous

[2]Note that wall cooling can cause a local increase in mass flux through the boundary layer resulting in an effective throat area that is larger than the actual throat area; however, this is not relevant to critical nozzle applications under normal calibration conditions.

discharge coefficient as

$$C_{d_{vis}} = 1 - 4\frac{\delta^*}{d} + O\left[\left(\frac{\delta^*}{d}\right)^2\right]. \tag{1.10}$$

A variety of boundary layer methods have been used to estimate the throat displacement thickness for nozzle flows. In 1964, Stratford [26] used integral boundary layer methods to estimate the momentum thickness for compressible flow over a flat plate. He estimated the displacement thickness, δ^*, by multiplying his expression for momentum thickness by a value of the shape factor valid for an incompressible flow with a favorable pressure gradient. In 1971, Kuluva and Hosack [43] used integral boundary layer techniques to directly solve for δ^* at the throat of a critical nozzle. Other researchers used similarity solutions of the governing compressible, axisymmetric laminar boundary layer equations in order to obtain higher accuracy predictions of the displacement thickness. Geropp [33] and Tang [30] independently developed similarity solutions to predict δ^* by implementing the following simplifying assumptions:

1. perfect gas with a constant specific heat,

2. one-dimensional free stream satisfying a Falkner-Skan type flow profile,

3. Prandtl number equal to unity,

4. adiabatic nozzle wall,

5. molecular viscosity directly proportional to temperature,

6. nozzle wall radius of curvature much larger than the boundary layer thickness.

Using these assumptions, these researchers developed nearly identical expressions for δ^*. When Geropp's expression for the displacement thickness is used in Eq. (1.10) the viscous discharge coefficient is expressed as

$$C_{d_{vis}} = 1 - \left(\frac{\gamma+1}{2}\right)^{1/4} \left[\frac{8(9-4\sqrt{6})}{3(\gamma+1)} + \frac{4\sqrt{6}}{3}\right] \frac{\Omega^{-1/4}}{\sqrt{Re^*_{ideal}}} \tag{1.11}$$

where γ is the specific heat ratio, Re^*_{ideal} is the Reynolds number based on throat diameter given in Section 1.4, and $\Omega = R/R_c$ is the nozzle throat radius, R, to the wall radius of curvature at the throat, R_c. The expression developed by Tang is identical to Eq. (1.11) with the exception that it includes an additional term that is inversely proportional to Reynolds number. This additional term, which is indicative of the Stokes regime, makes only a minor contribution to $C_{d_{vis}}$ (less than 0.1 %) for ISO nozzles (*i.e.,* $\Omega = .25$) at Reynolds numbers above 2000. Consequently, in light of errors introduced by the other simplifying assumptions, this term is generally neglected for high Reynolds number flows.

1.5.3 Virial Discharge Coefficient

The real gas or virial discharge coefficient, $C_{d_{virial}}$, was determined by Johnson [21]–[24]. Johnson's work differs from the analytical investigations of $C_{d_{inv}}$ and $C_{d_{vis}}$ in

that it was done numerically. He numerically integrated the one-dimensional energy equation along an adiabat. Along the integration path the thermodynamic properties were determined by a real gas equation of state. The limits of integration extended from known stagnation conditions (p_0 and T_0) to sonic conditions ($M = 1$). The manifold of thermodynamic states between these limiting conditions is identical to the thermodynamic states experienced by a fluid particle of fixed identity as it is isentropically accelerated from stagnation conditions to sonic conditions in a hypothetical critical nozzle. The flow in such a hypothetical critical nozzle corresponds to one-dimensional inviscid flow of a real gas. At the upper limit of integration ($M = 1$), by definition, the fluid velocity equals the sound speed. Accordingly, Johnson determined the mass flux at $M = 1$ by multiplying the density by the sound speed. For convenience, Johnson lumped all of the real gas effects into a modified critical flow function, $C_{s_{virial}}$, and expressed his mass flow results in a form equivalent to the ideal baseline model given in Eq. (1.2) of Section 1.3

$$\dot{m}_{virial} = \frac{p_0 A^* C_{s_{virial}}}{\sqrt{R_{gas}\ T_0}}. \tag{1.12}$$

The modified critical flow function, $C_{s_{virial}}$, has been aptly named the *Johnson coefficient*. The numerical results for $C_{s_{virial}}$ have been tabulated as a function of p_0 and T_0 for several gases in references [21]–[25]. Moreover, the ratio of mass flow, $\dot{m}_{virial}$ divided by the baseline mass flow $\dot{m}_{ideal}$ (see Eq. 1.2), defines the real gas discharge

coefficient, which is given as

$$C_{d_{virial}} = \frac{\dot{m}_{virial}}{\dot{m}_{ideal}}. \tag{1.13}$$

Because Johnson's work is numerical in nature, it is not convenient to combine his numerical results with the closed-form analytical results for $C_{d_{inv}}$ and $C_{d_{vis}}$. Instead, it has become customary to include Johnson's treatment of real gas effects directly in the experimentally measured discharge coefficients. Therefore, a common practice of many researchers is to amend the definition of the discharge coefficient given in Eq. (1.3) by defining C_d using $\dot{m}_{virial}$ as the normalizing theoretical mass flow instead of $\dot{m}_{ideal}$ as given by

$$C'_d = \frac{\dot{m}_{exp}}{\dot{m}_{virial}}. \tag{1.14}$$

This modified definition of the discharge coefficient, C'_d, is equivalent to using the *Johnson coefficient*, $C_{s_{virial}}$, in the place of the ideal critical flow function, $C_{s_{ideal}}$ (*e.g.,* compare Eq. 1.2 with Eq. 1.12). By normalizing the experimentally measured mass flow in this way, real gas effects are accounted for in the definition of the discharge coefficient and subsequently do not influence calibration data. That is, the functionality of C'_d (as given in Eq. 1.14) is independent of real gas effects. The explanation as to why real gas effects can be accounted for in this fashion is essentially a result of the assumption that each non-ideal flow mechanism is independent from the other non-ideal flow mechanisms. By combining Eq. (1.13) and Eq. (1.14) the

amended definition of the discharge coefficient can be mathematically expressed as

$$C_d' = \frac{C_d}{C_{d_{virial}}} = C_{d_{inv}} C_{d_{vis}} \tag{1.15}$$

where $C_d = \dot{m}_{exp}/\dot{m}_{ideal}$ is the usual definition of the discharge coefficient. Equation (1.15) mathematically shows that C_d' is independent of real gas effects.

The modified version of the discharge coefficient, C_d', should be used when comparing analytical models to experimental data. By using C_d' instead of C_d, closed form analytical models, which do not account for real gas effects, can be used to predict the discharge coefficient even when real gas effects are present in the flow. Fortunately, the numerical procedures used by Johnson to determine $C_{s_{virial}}$ and ultimately C_d', can be supplemented with approximate analytical techniques [62] when thermodynamic conditions do not substantially deviate from those of a perfect gas (*i.e.*, Z very close to unity). Under these conditions, $C_{d_{virial}}$ is approximated by using the ideal version of the critical flow factor with the specific heat ratio, $\gamma_0 = \gamma(T_0, P_0)$, evaluated at the local stagnation temperature and pressure as given by

$$C_{s_{virial}} \approx \sqrt{\gamma_0} \left(\frac{\gamma_0 + 1}{2} \right)^{\frac{(\gamma_0+1)}{2(1-\gamma_0)}} . \tag{1.16}$$

At low enough pressures, there is essentially no difference between this approximate value of $C_{d_{virial}}$ obtained by using Eq. (1.16) and the tabulated values of the *Johnson coefficient*.

1.5.4 Composite Analytical Model

In 1997, Ishibashi and Takamoto [34] used the axisymmetric inviscid flow model developed by Hall [28] (see Eq. 1.8) and the viscous boundary layer model of Geropp [33] (see Eq. 1.11) to predict the discharge coefficient of several commonly used gases. Their model simultaneously accounted for both boundary layer development and curvature of the sonic line. The experimental C_d values were defined according to Eq. (1.14) in order to minimize any real gas effects in the calibration data. This analytic model characterizes C_d in terms of both Re^*_{ideal} and γ, thereby correcting the calibration data by accounting for the changes in γ between different gas species. Nakao *et al.* demonstrated that this correction works quite well for several gases (*e.g.,* He, Ar, H_2, N_2, and O_2), predicting C_d behavior to within a few tenths of a percent [35]. However, for other gases (*e.g.,* CO_2 and SF_6) the Ishibashi and Takamoto model underpredicts C_d by more than 2 % – an error level unacceptable for high accuracy metering applications.

Figure (1.6) compares the analytical predictions of Ishibashi and Takamoto [34] to experimental calibration data of Nakao *et al.* [35] for several gases. The experimental measurements were taken at Reynolds numbers in the laminar flow range using a small throat diameter ($d = 0.5935\,\mathrm{mm}$) ISO critical nozzle. As before, the symbols used in the figure have been scaled to the experimental uncertainty. (Note that uncertainty components due to the nozzle throat diameter are not included.) Following the results of previous analytical investigations [30, 33] and experimental

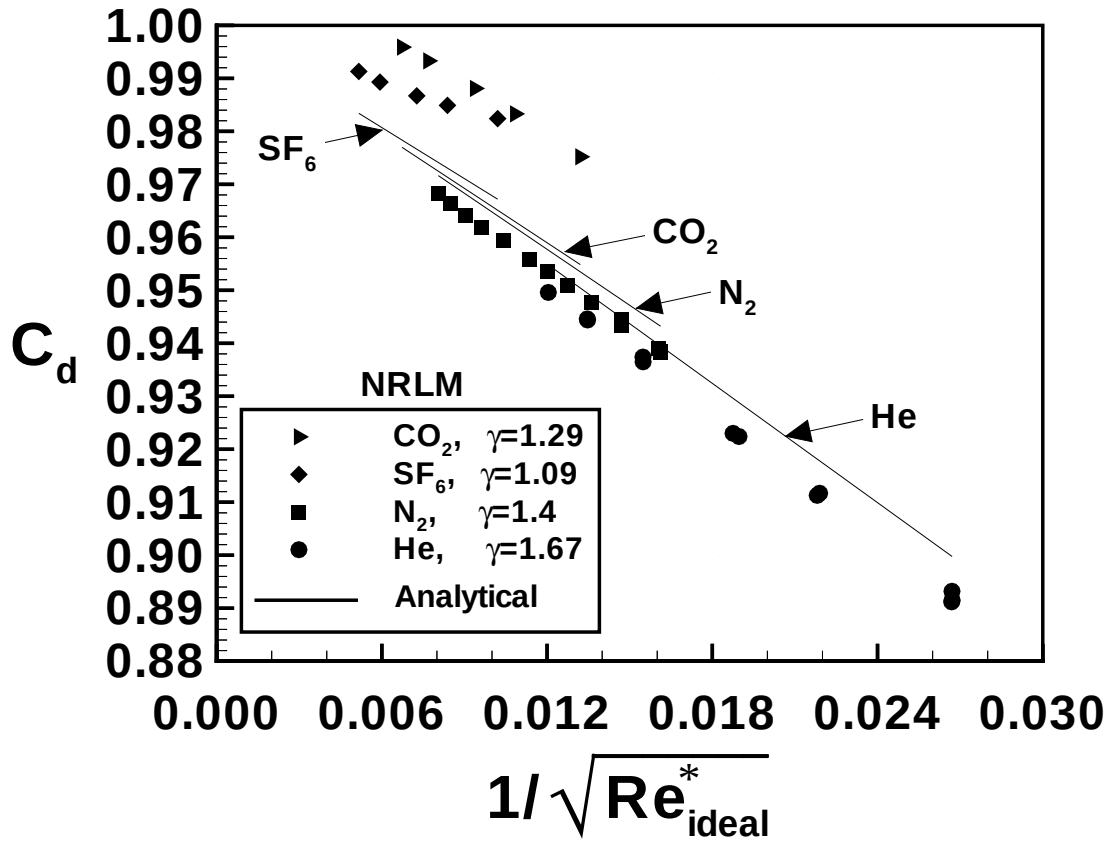

Figure 1.6. Comparison of experimental calibration data with predictions from analytical models.

observations [34, 39], the calibration data has been linearized by plotting C_d versus $1/\sqrt{Re^*_{ideal}}$ (see Eq. 1.11). This method of linearization works because C_d (to first order) is directly proportional to the displacement thickness, δ^*, which varies inversely with the square root of Reynolds number for laminar flows. The experimental data also depicts how viscous effects influence the discharge coefficient. At high Reynolds numbers (*i.e.,* low $1/\sqrt{Re^*_{ideal}}$) the boundary layer thins and C_d increases for all the gases considered.

Accurate gas flow measurement ultimately depends on characterizing the discharge

coefficient over a range of different operating conditions. Understanding the boundary layer development along the nozzle wall, and the curvature of the sonic line are at the heart of accurately predicting and understanding the influence of different operating conditions on the discharge coefficient. The analytic models discussed in this section have aided experimental calibration by determining some of the important dimensionless parameters necessary to characterize the discharge coefficient. The physical insight obtained through these models has also aided in optimizing the geometrical design of critical nozzles [36]. However, experimental data indicates that calibration curves are significantly affected by gas species, yet the analytical models exhibit only a weak dependence on gas species. Furthermore, extrapolating the experimental data in Fig. (1.6) to higher Reynolds numbers (*i.e.,* lower $1/\sqrt{Re^*_{ideal}}$) suggest that the experimental C_d values will be larger than unity for some gases (*e.g.,* CO_2) . The larger than unity experimentally extrapolated C_d values occur in spite of the fact that the discharge coefficient is normalized by the one-dimensional, inviscid mass flow, $\dot{m}_{virial}$. Thus, for the first time we observe experimental data in which the actual mass flow exceeds the ideal flow. This result is totally unexpected based on the well developed analytical works, and there is no physical understanding explaining this phenomenon.

1.6 Research Objectives

The objective of this investigation is to compare the accuracy of C_d predictions from conventional analytical models (discussed in Section 1.5) against numerically

calculated full Navier-Stokes solutions. In doing so we will assess the effectiveness of the various analytical correlations used in predictive models and attempt to identify the reasons for the very poor analytical C_d predictions of certain gases (*e.g.,* CO_2 and SF_6). Additionally, the numerical analysis will be used to study how various mechanisms affect the mass flow in an attempt to develop models capable of predicting mass flow to accuracy levels approaching those of primary mass flow standards.

The numerical investigation may provide insight that will improve existing calibration methods. Calibration data has been shown to be species dependent at lower Reynolds numbers [35]. Previously published analytical models have had only limited success characterizing this phenomenon. By solving the full Navier-Stokes equations we alleviate the need for many of the simplifying assumptions used in analytical methods. Numerical methods are expected to be flexible enough to include a more complete physical description (*i.e.,* temperature dependent specific heat, real gas effects, non-unity Prandtl number, a more physical non-adiabatic wall thermal boundary condition, upstream pipeline installation effects, coupling between the various non-ideal mechanisms, possible non-equilibrium effects due to rapid flow expansion through the nozzle, etc.). Systematic comparisons between the CFD and the experimental data will aid in determining which, if any, of these physical mechanisms lead to improved predictive capabilities. Additionally, the analysis will help to quantify the degree of error introduced by various simplifications used in analytical models. Ultimately, improved predictive capabilities for a wider number of gas species and flows could

lead to use of numerical methods to calibrate critical nozzles for applications where experimental calibration is impractical or infeasible.

Chapter 2

MATHEMATICAL FORMULATION

For the nozzle flows of interest in this investigation the Reynolds numbers range varies from 2 000 to 131 000. Experimental evidence indicates that transition to turbulent flow occurs at much higher Reynolds numbers (10^6) for toroidal throat critical nozzles [37]. As a result the fluid motion is governed by the compressible, axisymmetric laminar Navier-Stokes equations. Moreover, this research identifies that the flow physics for certain gas species involve interactions between gas dynamic processes and molecular energy exchange processes. Thus, the gas dynamic equations are coupled to the equations describing the molecular energy exchange between the vibrational and translational energy modes. Such non-equilibrium processes occur in critical nozzle flows when the vibrational modes of a polyatomic molecule relax slowly relative to flow processes. The numerical treatment of the Navier-Stokes equations is presented first in Section 2.1 through Section 2.3, followed by the numerical treatment of the vibrational relaxation phenomenon in Section 2.4, non-equilibrium thermodynamic relations in Section 2.5, and finally the appropriate boundary conditions in Section 2.6.

2.1 Scalar Equations of Motion

The unsteady, axisymmetric (*i.e.,* $u_\theta = 0$ and $\frac{\partial}{\partial\theta} = 0$) representation of the conservation equations in terms of the heat flux vector, q'', and the viscous stress tensor, τ, are given in scalar form by

$$\frac{\partial \rho}{\partial t} + \frac{\partial}{\partial x}(\rho u_x) + \frac{\partial}{\partial r}(\rho u_r) = -\frac{\rho u_r}{r} \tag{2.1}$$

$$\frac{\partial}{\partial t}(\rho u_x) + \frac{\partial}{\partial x}(\rho u_x^2 + p) + \frac{\partial}{\partial r}(\rho u_x u_r) = -\frac{\rho u_x u_r}{r} + \frac{\partial \tau_{xx}}{\partial x} + \frac{\partial \tau_{rx}}{\partial r} + \frac{\tau_{rx}}{r} \tag{2.2}$$

$$\frac{\partial}{\partial t}(\rho u_r) + \frac{\partial}{\partial x}(\rho u_r u_x) + \frac{\partial}{\partial r}(\rho u_r^2 + p) = -\frac{\rho u_r^2}{r} + \frac{\partial \tau_{rx}}{\partial x} + \frac{\partial \tau_{rr}}{\partial r} + \frac{\tau_{rr} - \tau_{\theta\theta}}{r} \tag{2.3}$$

$$\frac{\partial e}{\partial t} + \frac{\partial}{\partial x}\left[u_x(e+p)\right] + \frac{\partial}{\partial r}\left[u_r(e+p)\right] = -\frac{u_r(e+p)}{r} + \dot{Q}_{heat} + \dot{W}_{vis} \tag{2.4}$$

where $e = \rho[\epsilon + \frac{1}{2}(u_x^2 + u_r^2)]$ is the total energy per unit volume, a summation of the internal energy and kinetic energy. In these nozzle flows, the contribution of potential energy represents only a small fraction of the total energy and is therefore neglected. Likewise, the gravimetric body force terms are also omitted from the momentum equations (*i.e.,* Eq. 2.2 and Eq. 2.3) since these terms have an insignificant impact on the gas dynamics. In the energy equation (Eq. 2.4) the rate of work done by viscous forces, $\dot{W}_{vis}$, as well as the heat transfer rate, $\dot{Q}_{heat}$, have axisymmetric representations

given by the following expressions:

$$\dot{W}_{vis} = \frac{\partial(u_x\tau_{xx} + u_r\tau_{xr})}{\partial x} + \frac{\partial(u_x\tau_{xr} + u_r\tau_{rr})}{\partial r} + \frac{(u_x\tau_{xr} + u_r\tau_{rr})}{r},$$

$$\dot{Q}_{heat} = -(\frac{\partial q''_x}{\partial x} + \frac{\partial q''_r}{\partial r} + \frac{q''_r}{r}).$$

Following Stoke's hypothesis for a Newtonian fluid (see for example reference [38]) the stress tensor, τ, is directly proportional to the strain rate tensor. Moreover, the molecular viscosity, μ, is the proportionality factor. In an axisymmetric coordinate system the components of τ can be expressed as

$$\begin{aligned} \tau_{xx} &= \mu(\frac{4}{3}\frac{\partial u_x}{\partial x} - \frac{2}{3}\frac{\partial u_r}{\partial r} - \frac{2}{3}\frac{u_r}{r}) \qquad \tau_{rr} = \mu(-\frac{2}{3}\frac{\partial u_x}{\partial x} + \frac{4}{3}\frac{\partial u_r}{\partial r} - \frac{2}{3}\frac{u_r}{r}) \\ \tau_{\theta\theta} &= \mu(-\frac{2}{3}\frac{\partial u_x}{\partial x} - \frac{2}{3}\frac{\partial u_r}{\partial r} + \frac{4}{3}\frac{u_r}{r}) \qquad \tau_{xr} = \mu(\frac{\partial u_r}{\partial x} + \frac{\partial u_x}{\partial r}). \end{aligned} \tag{2.5}$$

where $\tau_{r\theta}$ and $\tau_{x\theta}$ are identically zero. The heat flux vector, q'', follows Fourier's law of heat conduction for a pure substance with axisymmetric components given by

$$\begin{aligned} q''_x &= -k\frac{\partial T}{\partial x} \\ q''_r &= -k\frac{\partial T}{\partial r} \end{aligned} \tag{2.6}$$

where q''_θ is identically zero.

2.2 Vector Equations of Motion

For numerical implementation it is convenient to express the set of scalar equations (Eq. 2.1 through Eq. 2.4) in vector notation. The time-derivative version of the governing set of scalar equations can be expressed in vector notation as given by

$$\Upsilon \frac{\partial Q_p}{\partial t} + \frac{\partial E}{\partial x} + \frac{\partial F}{\partial r} = H + L(Q_p) \tag{2.7}$$

where the inviscid flux vectors are given by

$$E = \begin{pmatrix} \rho u_x \\ \rho u_x^2 + p \\ \rho u_x u_r \\ (e+p)u_x \end{pmatrix}, \qquad F = \begin{pmatrix} \rho u_r \\ \rho u_r u_x \\ \rho u_r^2 + p \\ (e+p)u_r \end{pmatrix}.$$

The dependent vector, $Q_p = [p \ u_x \ u_r \ T]^T$, selected for convenience, together with the conservative vector, $Q_c = [\rho \ \rho u_x \ \rho u_r \ e]^T$ are used to define the Jacobian matrix, $\Upsilon = \partial Q_c / \partial Q_p$, on the left hand side of Eq. (2.7). On the right hand side of Eq. (2.7) the axisymmetric source vector, $H = H_{inv} + H_{vis}$, is divided into both an inviscid and viscous contribution. The inviscid, H_{inv}, and the viscous, H_{vis}, contributions are expressed as

$$H_{inv} = -\frac{1}{r}\begin{pmatrix} \rho u_x \\ \rho u_r u_x \\ \rho u_r^2 \\ u_r(e+p) \end{pmatrix}, \qquad H_{vis} = \frac{1}{r}\begin{pmatrix} 0 \\ h_{vis_2} \\ h_{vis_3} \\ h_{vis_4} \end{pmatrix}$$

where the non-zero components of the viscous axisymmetric flux vector, H_{vis}, are given by

$$h_{vis_2} = -\frac{2}{3}\frac{\partial(\mu u_r)}{\partial x} + \mu\frac{\partial u_x}{\partial r} + \mu\frac{\partial u_r}{\partial x}$$

$$h_{vis_3} = -\frac{2u_r}{3}\frac{\partial \mu}{\partial r} + \frac{4\mu}{3}\frac{\partial u_r}{\partial r} - \frac{4}{3}\frac{\mu u_r}{r}$$

$$h_{vis_4} = -\frac{2}{3}\frac{\partial(\mu u_x u_r)}{\partial x} - \frac{2}{3}\frac{\partial(\mu u_r^2)}{\partial r} + \mu u_x\frac{\partial u_x}{\partial r} + \mu u_x\frac{\partial u_r}{\partial x} - \frac{2\mu u_r}{3}\frac{\partial u_x}{\partial x} + \frac{4\mu u_r}{3}\frac{\partial u_r}{\partial r} + k\frac{\partial T}{\partial r}.$$

Furthermore, the viscous differential operator is denoted by L and is defined as

$$L = \frac{\partial}{\partial x}R_{xx}\frac{\partial}{\partial x} + \frac{\partial}{\partial x}R_{xr}\frac{\partial}{\partial r} + \frac{\partial}{\partial r}R_{rx}\frac{\partial}{\partial x} + \frac{\partial}{\partial r}R_{rr}\frac{\partial}{\partial r} \tag{2.8}$$

where the viscous matrices R_{xx}, R_{xr}, R_{rx}, and R_{rr} consist of

$$R_{xx} = \begin{pmatrix} 0 & 0 & 0 & 0 \\ 0 & \frac{4}{3}\mu & 0 & 0 \\ 0 & 0 & \mu & 0 \\ 0 & \frac{4}{3}\mu u_x & \mu u_r & k \end{pmatrix}, R_{xr} = \begin{pmatrix} 0 & 0 & 0 & 0 \\ 0 & 0 & -\frac{2}{3}\mu & 0 \\ 0 & \mu & 0 & 0 \\ 0 & \mu u_r & -\frac{2}{3}\mu u_x & 0 \end{pmatrix},$$

$$R_{rx} = \begin{pmatrix} 0 & 0 & 0 & 0 \\ 0 & 0 & \mu & 0 \\ 0 & -\frac{2}{3}\mu & 0 & 0 \\ 0 & -\frac{2}{3}\mu u_r & \mu u_x & 0 \end{pmatrix}, R_{rr} = \begin{pmatrix} 0 & 0 & 0 & 0 \\ 0 & \mu & 0 & 0 \\ 0 & 0 & \frac{4}{3}\mu & 0 \\ 0 & \mu u_x & \frac{4}{3}\mu u_r & k \end{pmatrix}.$$

2.3 Numerical Algorithm

In practical application Eq. (2.7) is usually transformed to its equivalent representation in the so called *body–fitted* coordinate system. In the body–fitted coordinate system the coordinate axes, (ξ,η), are aligned with the grid lines, facilitating a straightforward implementation of exterior and interior boundary conditions. While this coordinate transformation introduces several additional terms into the original vector form of the equation, the final *body–fitted* expression can be expressed in a form identical to the Eq. (2.7) by replacing the (x,r) coordinate axis with (ξ,η) and amending the definitions of the inviscid flux vectors E and F, the axisymmetric source vector H, and the viscous matrices R_{xx}, R_{xr}, R_{rx}, and R_{rr}. Details on the transformation to the body-fitted coordinate system can be found in reference [44].

Although our intent is to obtain steady state solutions, the numerical algorithm retains the time derivatives in Eq. (2.7), utilizing a time marching procedure to advance the solution to the desired steady state solution. Time advancement is obtained using first-order, backward finite differences. Spatial discretization, on the other hand, is accomplished using third order up-winded flux differences for the convective terms and central differences for the diffusive terms. In the present work both inviscid and viscous time-derivative preconditioning [45]−[47] are employed for accelerated convergence rates over a wide range of Mach numbers and Reynolds numbers. An approximately factored alternating-direction implicit (ADI) numerical algorithm is implemented to avoid sparse matrices thereby allowing the governing set of equations to be solved in a more efficient manner. The resulting approximately factored (ADI) delta form of the equations (Eq. 2.7) is shown below

$$\left[S + \Delta t \frac{\partial}{\partial x}\left(A \bullet - R_{xx}\frac{\partial}{\partial x}\right)\right] S^{-1} \left[S + \Delta t \frac{\partial}{\partial r}\left(B \bullet - R_{rr}\frac{\partial}{\partial r}\right)\right] \Delta Q_p = -\Delta t R^n \quad (2.9)$$

where ΔQ_p represents the change in the dependent variable between successive time steps, and R^n is the residual of the steady equation at the previous time level (*i.e.,* the steady state portion of Eq. 2.7). The Jacobian matrices on the left hand side, $A = \frac{\partial E}{\partial Q_p}$, $B = \frac{\partial F}{\partial Q_p}$, $D = \frac{\partial H}{\partial Q_p}$, and $S \equiv \Gamma - \Delta t D$ arise due to the choice of the semi-implicit ADI algorithm. These matrices affect convergence rates, but become unimportant as the left hand side tends to zero in the steady state limit. The dot, $\bullet$, in Eq. (2.9) should be taken to mean that differentiation in the x-direction (or r-direction) applies

to the *product* of the Jacobian matrix A (or B) immediately preceding it, and the entire expression *to the right* of the enclosing brackets, [ ]. (*e.g.,* The expression $\frac{\partial}{\partial r}\left[(B\bullet + R_{rr}\frac{\partial}{\partial r})\right]\Delta Q_p$, should be interpreted as $\frac{\partial(B\,\Delta Q_p)}{\partial r} + \frac{\partial}{\partial r}(R_{rr}\frac{\partial \Delta Q_p}{\partial r})$).

When Eq. (2.9) is discretized, the two terms enclosed in brackets, [ ], are observed to be block tridiagonal operators in the x-direction and r-direction respectively. To efficiently solve this system of block tridiagonal operators Eq. (2.9) is expressed as two distinct block tridiagonal systems:

$$\left[S + \Delta t\frac{\partial}{\partial x}\left(A\bullet - R_{xx}\frac{\partial}{\partial x}\right)\right]\Delta Q_p^* = -\Delta t\, R^n \tag{2.10}$$

$$\left[S + \Delta t\frac{\partial}{\partial r}\left(B\bullet - R_{rr}\frac{\partial}{\partial r}\right)\right]\Delta Q_p = S\,\Delta Q_p^* \tag{2.11}$$

where the interim vector, $\Delta\, Q_p^*$, is solved during the first sweep and used as an input on the second sweep. Both block tridiagonal systems are inverted using a block version of the Thomas algorithm [48] at each time step until convergence is achieved.

2.4 Vibrational Relaxation

Gas flow through the converging section of a critical nozzle is accelerated from nearly stagnant upstream conditions to sonic conditions in the vicinity of the nozzle throat. Ideally, this acceleration process is governed by the reversible conversion of thermal energy into kinetic energy. Subsequently, the temperature decreases as the

gas accelerates through the convergent section of the nozzle. In small-scale critical nozzles this acceleration process occurs over small distances (*i.e.,* about 1 mm for the calibration data in Fig. 1.5). Consequently, flow residence times are short (about 10^{-6} seconds), leaving insufficient time for the vibrational energy modes of the flowing gas molecules to equilibrate with the changing thermodynamic environment.[1] This phenomenon is known as *vibrational non-equilibrium* or *vibrational relaxation.*

2.4.1 Conditions Necessary for Vibrational Relaxation

Vibrational relaxation phenomenon can play an appreciable role in the flow processes of select gases through critical nozzles when the following conditions are satisfied:

1. The vibrational relaxation time (*i.e.,* the time necessary for a thermodynamic system to redistribute its vibrational energy when subjected to a new thermodynamic environment) is greater than or equal to the flow residence time ($\tau_{vib} \geq \tau_{res}$).

2. The vibrational energy makes a non-negligible contribution to the overall internal energy of the gas.

These two conditions are not simultaneously realized for all gas species, and hence the effect of non-equilibrium phenomenon varies from gas to gas. Simpler molecules

[1] Translational and rotational modes relax much faster than vibrational modes and therefore equilibrate with the local thermodynamic environment.

(*i.e.,* the diatomic molecules: H_2, O_2, and, N_2) relax slowly, but do not have sufficient vibrational energy at normal operating temperatures (around 300 K) for vibrational relaxation effects to be important (*i.e.,* condition 2 is not satisfied). On the other hand, larger, more complex molecules frequently do have sufficient vibrational energy even at room temperature. Nevertheless, most equilibrate quickly so that condition 1 is not satisfied.

An order of magnitude analysis can be used to determine which gases are likely to experience vibrational relaxation effects. A brief analysis is presented here that quantifies conditions 1 and 2 for selected gases, first for N_2 and then CO_2. To make this analysis definitive we consider the calibration data for the small throat diameter nozzle (*i.e.,* $d = 0.5395$ mm) shown in Fig. (1.5), and we determine the internal energy, the vibrational energy, and the vibrational relaxation time at a suitable reference temperature and pressure of 300 K and 1 atm respectively.

For N_2, the average flow residence time can be estimated by dividing the appropriate length scale (*i.e.,* the distance from the nozzle inlet to the nozzle throat) by the average velocity over this distance. If the average velocity is estimated by using one-dimensional ideal flow theory, then the average flow residence time is on the order of 10^{-6} seconds. The vibrational relaxation time for N_2 (at the reference condition) is on the order of 10^{-5} seconds. Since N_2 equilibrates nearly an order of magnitude slower than the average residence time, vibrational relaxation effects could be important if N_2's vibrational energy levels are sufficiently populated. At the reference temperature

of 300 K, only 0.007 % of N_2's overall internal energy is stored as vibrational energy. Consequently, although condition 1 indicates that N_2 flow is not in vibrational equilibrium, the effect of non-equilibrium flow processes on the gas dynamics is negligible due to the insignificant level of vibrational energy at room temperature.

For CO_2 the vibrational relaxation time is on the same order of magnitude as the average flow residence time so that vibrational relaxation effects are again present in the flow field. Unlike N_2, however, the contribution of vibrational energy of CO_2 at room temperature represents 10.1 % of the overall internal energy. As a result, vibrational non-equilibrium phenomena could play a role in the gas dynamics of CO_2 flow. Results presented later show that indeed relaxation effects do affect the gas dynamics of both CO_2 and SF_6, and that this mechanism explains the unusual C_d behavior shown previously in Fig. (1.6) for these two gases.

2.4.2 Vibrational Relaxation Model

When vibrational non-equilibrium effects are important, they are primarily an issue in the inviscid core region of critical nozzle flows where they alter thermodynamic and flow processes. For example, the isentropic expansion process is rendered irreversible, and notions of equilibrium thermodynamics must be supplemented with non-equilibrium thermodynamics. Initially, prior to flow acceleration in the converging nozzle section, the gas is locally in equilibrium, so that the translational, rotational, and vibrational temperatures are all equal. As the fluid element accelerates through

the converging section of the nozzle, however, the vibrational energy, ϵ_{vib}, does not adjusts to the ever decreasing downstream temperatures, causing the flow to deviate further and further from equilibrium behavior with advancing downstream distances. Consequently, the vibrational temperature, T_{vib}, of the fluid molecules differs from the translational and rotational temperature, T. The resulting non-equilibrium internal energy is a function of the pressure, p, the temperature, T, and the vibrational temperature, T_{vib}.

To account for vibrational non-equilibrium effects in predictive models, the local non-equilibrium value of vibrational energy must be determined throughout the flow field. The molecular energy exchange between vibrational modes and external modes (*i.e.,* translational and rotational modes) can be modeled using the vibrational rate equation which is given as (see reference [49])

$$\frac{D\epsilon_{vib}(T_{vib})}{Dt} = \frac{\epsilon_{vib}(T) - \epsilon_{vib}(T_{vib})}{\tau_{vib}(p,T)} \tag{2.12}$$

where $\epsilon_{vib}(T_{vib})$ is the non-equilibrium level of vibrational energy, $\epsilon_{vib}(T)$ is the equilibrium level of vibrational energy, and $\tau_{vib}(p,T)$ is the vibrational relaxation time. This equation can be formally developed using molecular theory under the following assumptions:

1. Each vibrational mode can be considered a harmonic oscillator.

2. The entire vibrational energy content relaxes at a single relaxation time.

3. Intermolecular collisions can change a molecule's energy level only into the next adjacent higher or lower energy level.

4. The distribution of molecules in their respective vibrational energy levels does not significantly deviate from the equilibrium (*i.e.,* Boltzmann) distribution at the vibrational temperature.

Strictly speaking, the vibrational rate equation as given in Eq. (2.12) is only valid for molecules having only one vibrational degree of freedom (*i.e.,* diatomic molecules). However, ultrasonic absorption and dispersion data for many polyatomic molecules (*e.g.,* CO_2, and SF_6) have demonstrated that the whole of the vibrational energy relaxes at a single relaxation time [50],[51] and is adequately modeled by Eq. (2.12) over the thermodynamic conditions relevant in the present work.

The vibrational model given by Eq. (2.12) is not expected to work equally well for all gases or for any range of thermodynamic conditions. For example, CO_2 gas undergoes multiple relaxation processes at higher temperatures so that individual vibrational modes relax at different rates. For CO_2 near room temperature the vast majority of vibrational energy resides in the bending vibrational mode so that the other vibrational modes need not be considered. At higher temperatures, however, the symmetric and asymmetric vibrational modes of CO_2 play an increased role in molecular energy exchange with the external degrees of freedom. Therefore, to account for the additional vibrational modes it is necessary to solve several vibrational

rate equations, one for each relaxing mode. On the other hand, for SF_6 gas the vibrational frequencies are fairly closely spaced together so that SF_6 is likely to relax with a single relaxation time even at elevated temperatures. Thus, Eq. (2.12) could be used with good confidence to model SF_6 gas at higher temperatures, but not for CO_2 gas.

An expression for the vibrational relaxation time as a function of temperature and pressure has been developed by Landau and Teller [52]. Generally speaking, the vibrational relaxation time decreases with increasing pressure or temperature. Physically, increased pressure results in a higher number of molecular collisions, thereby providing more opportunities for molecular energy exchange. Likewise, increased temperatures result in more energy exchange for each collision which typically reduces the relaxation time.

Gas	K_1 (Pa-sec)	K_2 (K)
CO_2	0.04204828	10635.06
SF_6	0.07599375	0.0

Table 2.1. Constants for vibrational relaxation time of various gases

A commonly used low temperature approximation of the expression for relaxation time developed by Landau and Teller is given in reference [53] as

$$\tau_{vib} = K_1 \frac{exp\left[(K_2/T)^{1/3}\right]}{p} \tag{2.13}$$

where the constants K_1 and K_2 depend on properties of the molecule. In the present work these constants have been determined by curve fitting experimental relaxation time data [54],[55] to Eq. (2.13) at an atmospheric reference pressure over a temperature range from 200 K to 300 K. The value of these constants for various molecules are given in Table (2.1). Note that for SF_6 the relaxation time is independent of temperature over the temperature range of interest indicating that the value for K_2 is identically equal to zero.

vibrational mode (N=3)	g_k	$\theta_k(K)$
bending	2	959
symmetric	1	1920
asymmetric	1	3380

Table 2.2. Degeneracies and characteristic vibrational temperatures for CO_2

vibrational mode (N=6)	g_k	$\theta_k(K)$
1	3	522.0
2	3	753.6
3	3	887.3
4	2	926.1
5	1	1114.4
6	2	1387.8

Table 2.3. Degeneracies and characteristic vibrational temperatures for SF_6

Statistical mechanics can be used to determine a suitable expression for the equilibrium level of molecular vibrational energy [53]. For a polyatomic molecule with

N vibrational degrees of freedom the equilibrium vibrational energy is given by a summation consisting of the molecular vibrational energy of each vibration mode weighted by the degeneracy of each mode

$$\epsilon_{vib}^{eq} = \sum_{k=1}^{N} \frac{g_k \; R_{gas} \; \theta_k}{\exp(\theta_k/T) - 1}. \tag{2.14}$$

In this expression g_k is the number of degeneracies for the k^{th} vibrational mode and θ_k is the characteristic vibrational temperature for the k^{th} vibrational mode. Notice that the vibrational energy is only a function of temperature, given that molecular vibrations in gases do not exert any pressure. Tables (2.2) and (2.3) give the characteristic vibrational temperatures and number of degeneracies for both CO_2 and SF_6 gases.

2.4.3 Numerical Solution of the Vibrational Rate Equation

For the purposes of this research a form of the vibrational rate equation valid for steady flows along a streamline is implemented as given below

$$\Gamma \frac{d\epsilon_{vib}}{dz} = \epsilon_{vib}^{eq} - \epsilon_{vib}. \tag{2.15}$$

In this expression $\epsilon_{vib}^{eq} = \epsilon_{vib}(T)$ is the equilibrium level of vibrational energy, $\epsilon_{vib} = \epsilon_{vib}(T_{vib})$ is the non-equilibrium value of vibrational energy, $z = s/L$ is the dimensionless distance along a streamline, and $\Gamma = \tau_{vib}/\tau_{res}$, is the ratio of local vibrational

relaxation time to the residence time. The local residence time, $\tau_{res} = L/||\vec{u}||$, is defined in terms of $||\vec{u}||$, the local magnitude of fluid velocity, and L, the characteristic length along a streamline.

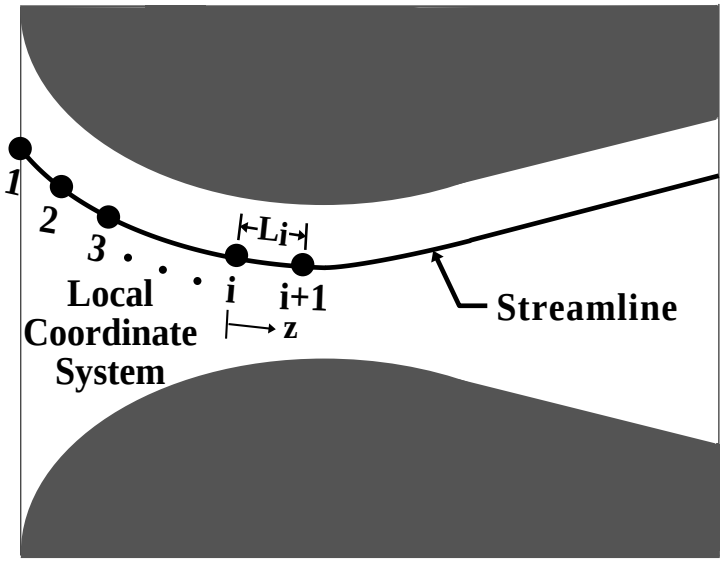

Figure 2.1. Schematic illustrating local coordinate frame used for solving the vibrational rate equation.

In contrast to the Navier-Stokes equations which are expressed in an Eulerian sense, the vibrational rate equation is expressed in a Lagrangian sense. Specifically, Eq. (2.15) describes the rate of relaxation of the vibrational modes of a gas particle of fixed identity as it moves through the flow field. The Lagrangian paths of particles of fixed identity correspond to streamlines in the flow field. The trajectories of these streamlines must be estimated from the Navier-Stokes solution before the vibrational rate equation can be solved. In the coupling procedure between the two equation sets, the streamlines in the flow field are computed after each time step using the

most recent approximation to the Navier-Stokes solution. The vibrational rate equation (Eq. 2.15) is then solved on each streamline by a space-marching procedure that integrates between consecutive points on a streamline (see Fig. 2.1).

Integrating the vibrational rate equation along streamlines provides a convenient method for including relaxation effects, however, this procedure presents a minor difficulty. In general, grid points do not coincide with streamlines and interpolation is necessary to find the streamlines. To improve accuracy and provide a more straightforward integration procedure without interpolation, the grid system was adjusted after each iteration to lie on the streamlines computed from the most recent time-step of the Navier-Stokes equations. The vibrational rate equation was then integrated on this new grid system to obtain the relaxation rates at each point in the flow field. The Navier-Stokes equations were also solved on the new grid at the next time step. As convergence is approached, the grid system becomes stationary, and the Navier-Stokes and the vibrational rate equation are solved on the same, streamline-oriented grid system. Consequently, the need for interpolation is eliminated.

In computing the solution for the vibrational rate equation, the coefficient $\Gamma = \tau_{vib}/\tau_{res}$ and the source term ϵ_{vib}^{eq} are both evaluated from the latest solution of the Navier-Stokes equation. The space-marching procedure starts at the nozzle inlet where the vibrational energy on each streamline (each grid line) is equal to its equilibrium value (*i.e.*, $\epsilon_{vib}^{1} = \epsilon_{vib}^{eq}(T_1)$). The integration procedure (herein done analytically by variation of parameters,[58]) determines ϵ_{vib} at the next grid point. In turn, this

value of ϵ_{vib} serves as an initial condition for the next point, and so on, until the complete streamline has been updated. This process is then repeated for each streamline in the flow field. (The details of this semi-analytic integration procedure are given in appendix 1). The calculated value of vibrational energy, ϵ_{vib}, is used to determine the thermodynamic internal energy, $\epsilon = \epsilon(p, T, \epsilon_{vib})$, which in turn, is used to update the Navier-Stokes equations. Consequently the Navier-Stokes solution depends upon the vibrational rate solution and conversely.

2.5 Thermodynamic Relations for Density and Internal Energy

The solution of the non-equilibrium flow field is obtained by globally iterating between the Navier-Stokes equations (*i.e.,* Eq. 2.1 – Eq. 2.4) and the vibrational rate equation (*i.e.,* Eq. 2.15) in such a manner as to ensure that both are simultaneously satisfied. To close the system of conservation equations, however, it is necessary to develop an equation of state that interrelates thermodynamic variables. Specifically, both the fluid density and internal energy must be related to other thermodynamic quantities. Under equilibrium flow conditions the density and internal energy are completely characterized as a function of the local temperature and pressure in the nozzle. In the case of vibrational non-equilibrium, however, the internal energy must be modified to include non-equilibrium effects. The equation of state for density, on the other hand, remains unchanged. Physically, the molecular vibrational energy is independent of pressure so that relaxation phenomenon does not directly result in

density changes. In this section, both the equation of state (*i.e.*, $\rho = \rho(p, T)$) and the thermodynamic state relationship for the internal energy (*i.e.*, $\epsilon = \epsilon(p, T, \epsilon_{vib})$) are formulated in a general fashion so that they are valid for either the equilibrium or non-equilibrium flow situation.

2.5.1 Density

The generalized equation of state for density, valid for both equilibrium and non-equilibrium flow situations, is given implicitly as a function of both temperature and pressure

$$p = \rho R_{gas} T Z. \tag{2.16}$$

In this expression the density cannot be solved for explicitly as a function of temperature and pressure since the compressibility factor, Z, is given as a power series in ρ as shown below [61]

$$Z = [1 + \rho \mathrm{B} + \rho^2 \mathrm{C} + \rho^3 \mathrm{D} + ...]. \tag{2.17}$$

In Eq. (2.17) the temperature dependent coefficients B(T), C(T), and D(T), are the second, third, and fourth virial coefficients that provide a correction for real gas effects. When corrections for real gas behavior are not too substantial, as is the case in many critical nozzle flow applications, Eq. (2.17) can be truncated after the second term so that the compressibility factor is given by

$$Z = [1 + \rho \mathrm{B(T)}]. \tag{2.18}$$

It follows that the equation of state for density simplifies to the following

$$p = \rho R_{gas} T [1 + \rho \mathrm{B(T)}]. \tag{2.19}$$

Since equation (2.19) is a quadratic equation with respect to density, the quadratic formula can be used to express density explicitly as a function of temperature and pressure

$$\rho = \frac{2\rho_i}{1 + \sqrt{1 + 4\rho_i \mathrm{B(T)}}} \tag{2.20}$$

where $\rho_i = p/(R_{gas}T)$ is the *ideal* fluid density.

Gas	C_0	C_1	C_2	C_3	C_4	C_5	MW
Ar	-15.706	-59.676	-8.881	-3.1653	4.8214	-4.8895	39.949
CO_2	-123.76	-276.72	-73.164	-102.95	-953.5	-504.22	44.010
H_2	14.581	-6.6384	-7.7302	32.962	-52.828	26.617	2.016
N_2	-4.8208	-59.578	-10.834	10.157	-16.034	7.2891	28.013
SF_6	-279.24	-647.19	-231.67	-21.247	-1640.8	2211.2	146.056

Table 2.4. Polynomial Curve Fit Data for the Second Virial Coefficient over a temperature range from 200 K to 300 K.

In determining the density from known values of temperature and pressure, it is necessary to specify the second virial coefficient, B(T), as a function of temperature. In this research experimental data [60] for the second virial coefficient, B(T), was characterized by using fifth degree polynomial curve fits for several gases

$$T_{ref} = 298.15\,\mathrm{K}, \qquad \theta = \frac{T_{ref}}{T} - 1$$

$$B(T) = A_0 + A_1\theta + A_2\theta^2 + A_3\theta^3 + A_4\theta^4 + A_5\theta^5 \tag{2.21}$$

where the C_i's in Table (2.4) are related to the A_i's in Eq. (2.21) by a conversion factor $A_i = C_i\ (10^3/MW)$ so that B(T) has SI units of (m^3/kg).

2.5.2 Internal energy

To develop an expression for the internal energy that is valid for both vibrational equilibrium and non-equilibrium flows, the internal energy is expressed in terms of its molecular components as follows[2]

$$\epsilon = \epsilon^{eq}_{trans} + \epsilon^{eq}_{rot} + \epsilon_{vib} \tag{2.22}$$

where ϵ^{eq}_{trans} is the equilibrium molecular translational energy, ϵ^{eq}_{rot} is the equilibrium molecular rotational energy, and ϵ_{vib} is the non-equilibrium molecular vibrational energy. Because relaxation rates of translational and rotational energy modes are fast relative to rates of flow processes both ϵ^{eq}_{trans} and ϵ^{eq}_{rot} are taken to be in equilibrium.

[2]The expression for internal energy given in Eq. (2.22) omits the electronic energy which makes only a negligible contribution over the temperature range of interest.

On the other hand, vibrational relaxation processes (for some molecules) may be slow in comparison to flow processes, so that depending on the gas specie and flow conditions, ϵ_{vib} could have, in general, either equilibrium or non-equilibrium values. Therefore, to account for both the equilibrium and non-equilibrium flow processes, ϵ_{vib} is specified as its non-equilibrium value, but it defaults to the equilibrium value for the appropriate flow conditions.

The equilibrium level of internal energy can be determined by adding the equilibrium level of vibrational energy to the translational and rotational energy modes resulting in the following expression

$$\epsilon^{eq} = \epsilon^{eq}_{trans} + \epsilon^{eq}_{rot} + \epsilon^{eq}_{vib} \tag{2.23}$$

where the equilibrium value of vibrational energy, ϵ^{eq}_{vib}, has been defined previously in Eq. (2.14). It follows that arbitrarily adding and subtracting ϵ^{eq}_{vib} to the right hand side of Eq. (2.22) yields the following expression for the non-equilibrium internal energy

$$\epsilon = (\epsilon^{eq}_{trans} + \epsilon^{eq}_{rot} + \epsilon^{eq}_{vib}) + (\epsilon_{vib} - \epsilon^{eq}_{vib}). \tag{2.24}$$

The first set of terms in the parentheses on the right hand side of Eq. (2.24) is recognized as the equilibrium level of internal energy energy, $\epsilon^{eq} = \epsilon^{eq}(T, p)$ – taken to be a function of temperature and pressure herein. The second set of terms in the parentheses accounts for vibrational non-equilibrium effects. Equation (2.24) therefore relates the non-equilibrium internal energy, $\epsilon = \epsilon(T, p, \epsilon_{vib})$, to the equilibrium

internal energy, $\epsilon^{eq}(T,p)$, as given by

$$\epsilon(T,p,\epsilon_{vib}) = \epsilon^{eq}(T,p) + (\epsilon_{vib} - \epsilon^{eq}_{vib}). \tag{2.25}$$

In the special case of vibrational equilibrium (*i.e.*, $\epsilon_{vib} = \epsilon^{eq}_{vib}$) the last two terms in Eq. (2.25) cancel so that this general formulation of non-equilibrium internal energy reduces to the equilibrium situation.

Finally, to make use of Eq. (2.25) in the determination of the non-equilibrium value of internal energy, $\epsilon(T,p,\epsilon_{vib})$, it is necessary to determine an expression for the equilibrium internal energy, $\epsilon^{eq}_{vib}(T,p)$. In the present research the equilibrium internal energy is determined through its thermodynamic relationship to the equilibrium enthalpy, $h^{eq}(T,p) \equiv \epsilon^{eq}(T,p) + p/\rho$. From a manipulation of Maxwell's thermodynamic relations [61] the equilibrium enthalpy can be shown to have the following form[3]

$$h^{eq}(T,p) = \int_{T_{ref}}^{T} c_{p_i}(\tilde{T})\, d\tilde{T} + \rho R_{gas} T\,[\mathrm{B(T)} - T\mathrm{B}_T] \tag{2.26}$$

where the first term on the right hand side is the enthalpy change for an ideal gas and the second term is the necessary correction for real gas effects. The ideal gas specific heat at constant pressure, $c_{p_i}(T)$, was determined for several gases using polynomial curve fits to tabulated values given in references [56] and [57]. (Note that B(T) is the second virial coefficient given previously in Eq. 2.21 and B_T is its temperature derivative.)

[3]The constant reference datum for enthalpy is not included since only changes in enthalpy are relevant for gas dynamics calculations.

2.6 Boundary Conditions

In the numerical calculation of axisymmetric critical nozzle flows, boundary conditions are specified at inflow boundaries, outflow boundaries, along viscous walls, and along the centerline. The flow quantities specified at these interfaces are determined utilizing a combination of physical insight and mathematical rigor.

At inflow and outflow boundaries the viscous terms are small and the governing equations (Eq. 2.7) are to a good approximation hyperbolic in time. At these boundaries a locally approximately two-dimensional version of the method of characteristics [59] (MOC) determines the number of (*i.e.,* how many) boundary conditions to specify. The type of boundary condition prescribed is in general dictated by the flow physics. A convenient choice is to specify those flow variables that can be measured experimentally.

At the subsonic inflow boundary of a critical nozzle, MOC requires three flow quantities to be specified. The choice of variables is not unique, and in fact, any three independent flow quantities are sufficient; however, not all variable choices work equally well numerically. In order to mimic experimental calibration procedures for a critical nozzle (see Section 1.4) as closely as possibly, we specify the stagnation temperature, T_0, and stagnation pressure, p_0, at the inflow boundary. As the third boundary condition the inlet flow angle, a function of u_r/u_x, is specified. Although there is little physical basis for setting the flow angle, it is well-posed mathematically, simple to

implement, and (as will be demonstrated in Chapter 3) works well for the purposes of the present study. For an arbitrary equation of state the form of the upstream inflow boundary conditions are given as

$$\int_{p}^{p_0} \frac{d\tilde{p}}{\rho(\tilde{p}, s)} = \frac{1}{2}(u_x^2 + u_r^2) \tag{2.27}$$

$$\int_{T}^{T_0} \frac{\rho c_p}{\rho_{\tilde{T}} \tilde{T}} d\tilde{T} = -\frac{1}{2}(u_x^2 + u_r^2) \tag{2.28}$$

$$\eta_x u_x + \eta_r u_r = 0 \tag{2.29}$$

where η_x and η_r are metrics associated with the transformation to the body-fitted coordinate system and the variables denoted by "˜" are dummy variables of integration. Note that stagnation boundary conditions are expressed in integral form when real gas behavior is considered. The integrand of these integral expressions should be integrated with the entropy, s, held fixed; however these expressions cannot be evaluated until a suitable equation of state is selected. In the case of an ideal gas with constant specific heats, these integral expressions can be simplified to algebraic expressions. The algebraic expressions that result for the assumption of a calorically perfect ideal gas can also be utilized as an good approximation for real gas behavior when the inlet Mach number is significantly less than unity (*i.e.,* $M < 0.1$).

The procedure for specifying outflow boundary conditions is identical to that of

inflow boundary conditions. The number of outflow boundary conditions depends on the local Mach number in the direction of the exiting flow. For locally supersonic flow no physical boundary conditions are imposed, and the flow status is determined by solving the equations of motion at the exit boundary. However, for locally subsonic flow at the exit boundary, MOC requires specifying one boundary condition at the nozzle exit. By convention the back pressure, p_b is generally prescribed. In this study of choked nozzles we take the exiting flow to be supersonic and accordingly, solve the equations motion at the exit.

Along the nozzle wall viscous effects result in boundary layer development and the MOC does not apply. Physical intuition is used to prescribe the viscous wall boundary conditions. These boundary conditions include no velocity slip (*i.e.,* $u_x = 0$), impermeable nozzle wall (*i.e.,* $u_r = 0$), zero normal pressure gradient (commonly assumed in thin boundary layer theory, $\partial p/\partial n = 0$), and an appropriate thermal boundary condition such as an adiabatic wall or uniform wall temperature. For convenience the effect of the wall thermal boundary condition is denoted by the dimensionless wall temperature, T_{wall}/T^*. (In a later section we will assess the effects of this parameter on mass flow). Boundary conditions are implemented along the nozzle centerline as follows

$$\frac{\partial p}{\partial r} = 0, \quad \frac{\partial u_x}{\partial r} = 0, \quad u_r = 0, \quad \frac{\partial T}{\partial r} = 0. \tag{2.30}$$

Chapter 3

EVALUATION OF EQUILIBRIUM CFD MODEL

One of the primary objectives of this research is to compare the performance of CFD models based on the full Navier-Stokes equations to both the existing analytical models and to calibration data. Comparisons of CFD predictions with analytical predictions will help to assess the ramifications of various assumptions used in analytical models, while comparisons between CFD and experimental data will serve to assess the predictive capabilities of various CFD algorithms.

In the first part of this investigation a dimensional analysis is used to determine the functionality of the discharge coefficient. Following this, C_d is computed numerically and compared to predictions based on existing analytical models and experimental measurements. The results of the dimensional analysis are used for a parametric study to determine the influence of various dimensionless parameters on C_d. A physical explanation is provided to summarize the numerical results and describe the overall impact of important dimensionless parameters on C_d.

3.1 Dimensional Analysis

Traditionally experimental calibration curves give the discharge coefficient as function of only the throat Reynolds number for a given nozzle geometry. However, experimental studies by Nakao *et al.* have shown that at low Reynolds numbers (1 000 to 40 000) the discharge coefficient has a functional dependence on gas composition [35]. That is, each gas has a uniquely different calibration curve.

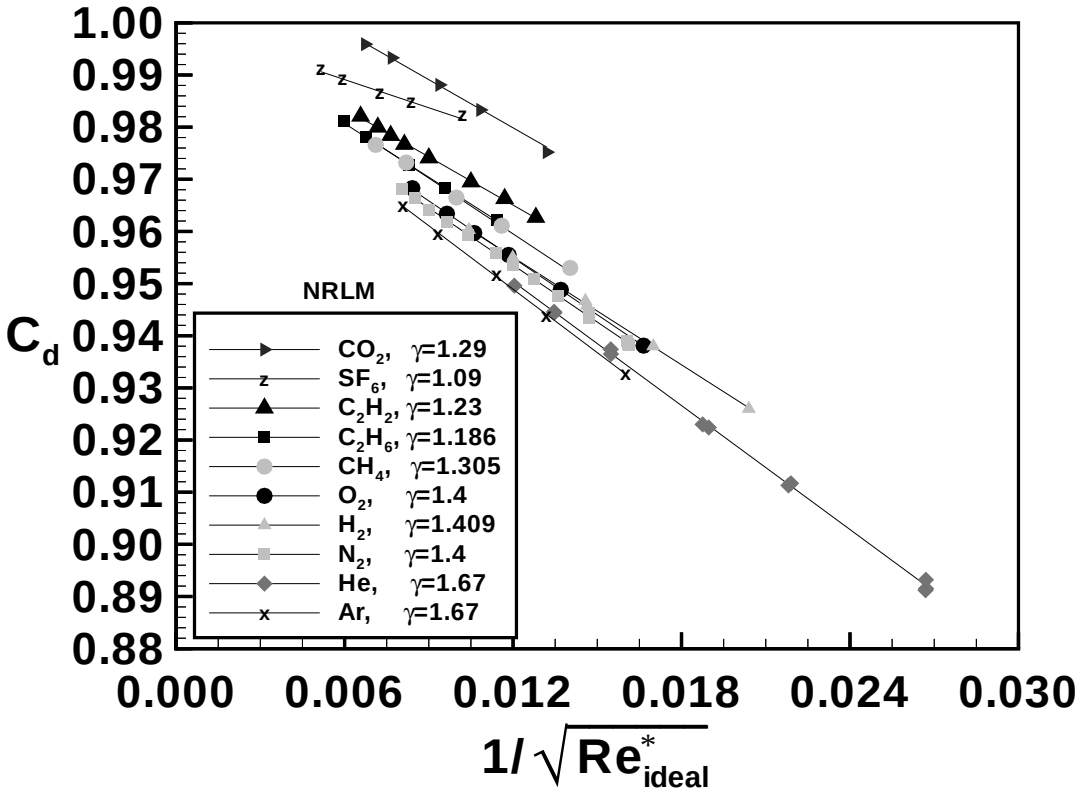

Figure 3.1. Calibration curve illustrating the effect of gas species on discharge coefficient (Uncertainty of data is less than 0.2 percent)

Figure (3.1) shows typical calibration data of several gas species where the data

is linearized by plotting C_d versus $1/\sqrt{Re^*_{ideal}}$. The experimental data shows that C_d can vary by more than three percent for different gas compositions at the same Reynolds number (*e.g.,* compare the CO_2 calibration curve to the Ar calibration curve in Fig. 3.1). Existing analytical models have made some progress toward explaining this effect by characterizing the discharge coefficient in terms of both Re^*_{ideal} and γ. However, a complete explanation of the physical mechanisms responsible for this effect has yet to be determined. An understanding of this phenomenon could lead to improved calibration. In particular, calibration might be made species independent – allowing calibration data of a given gas composition to be utilized for other gas compositions.

In this section a dimensional analysis is done to determine the primary dimensionless parameters that influence the discharge coefficient for arbitrary operating conditions and gas composition. In what follows, the important dimensionless parameters are determined by normalizing the governing gas dynamic equations from the previous chapter. In a later section a parametric study is used to investigate the functionality of the discharge coefficient on these dimensionless parameters. In this way many of the simplifying assumptions used in analytical models can be quantitatively assessed for their effect on the discharge coefficient.

We start by considering the complete set of governing equations, including the conservation equations (Eq. 2.1–2.4), constitutive equations (Eq. 2.5–2.6), and boundary conditions (Eq. 2.27–2.30). The dimensionless form of these equations reveal the

important dimensionless quantities characterizing the discharge coefficient. In this development we assume that the gas remains in thermodynamic equilibrium (an assumption we investigate in more detail in Chapter 4) as it flows through the nozzle, but we make no assumption about the thermodynamic equation of state. Therefore, the resulting expression for the discharge coefficient includes dimensionless parameters that account for real gas behavior. Later, however, the functionality of the discharge coefficient is simplified by invoking the ideal gas assumption.

The four components of the solution vector $Q_p = [p, u_x, u_r, T]^T$ are normalized by p^*, a^*, a^*, T^* respectively, where "a" is the speed of sound and the superscript, " * ", indicates evaluation of flow variables based on one-dimensional inviscid nozzle flow theory of a calorically perfect ideal gas at $M = 1$ (*i.e.,* the condition at the nozzle throat under ideal assumptions). Under these conditions, the sound speed at the nozzle throat is related to the square root of temperature, $a^* = \sqrt{\gamma R_{gas} T^*}$. The molecular viscosity, μ, following previous works, is normalized by μ_0, the value of molecular viscosity evaluated at the stagnation conditions. Similarly, the thermal conductivity, k, is normalized by k_0, the value of thermal conductivity evaluated at the stagnation conditions.

The specific heat at constant pressure, c_p, is normalized by a reference value, c_{p_i}, taken at 25 degrees Celsius for an ideal gas. Note that the subscript "i" in the reference value of specific heat denotes ideal gas behavior so that $c_{p_i} = R_{gas}\gamma/(\gamma - 1)$. In addition, the length scales in both the axial and radial directions are normalized

by the nozzle throat diameter, d, and time is normalized by, $\tau_{flow} = d/a^*$, the time it takes a fluid particle moving at sonic velocity to travel one nozzle throat diameter. Accordingly, we introduce the following dimensionless variables denoted by the superscript "$\hat{}$":

$$\hat{x} = \frac{x}{d}, \qquad \hat{r} = \frac{r}{d}, \qquad \hat{t} = \frac{t}{\tau_{flow}},$$

$$\hat{p} = \frac{p}{p^*}, \qquad \hat{u} = \frac{u_x}{a^*}, \qquad \hat{v} = \frac{u_r}{a^*}, \qquad \hat{T} = \frac{T}{T^*}, \tag{3.1}$$

$$\hat{\mu} = \frac{\mu}{\mu_0}, \qquad \hat{k} = \frac{k}{k_0}, \qquad \hat{c}_p = \frac{c_p}{c_{p_i}}$$

The density is normalized by $\rho^* = p^*/(R_{gas}T^*)$ so that the dimensionless density is related to temperature and pressure by the following equation of state

$$\hat{\rho} = \frac{\hat{p}}{Z\hat{T}} \tag{3.2}$$

where Z is the compressibility factor – a dimensionless factor that accounts for real gas effects.

The governing equations (Eq. 2.1–2.4) are repeated in this section in their dimensionless form to emphasize the pertinent dimensionless parameters that arise. This set of equations is expressed as

$$\frac{\partial \hat{\rho}}{\partial \hat{t}} + \frac{\partial \hat{\rho}\hat{u}_x}{\partial \hat{x}} + \frac{\partial \hat{\rho}\hat{u}_r}{\partial \hat{r}} = -\frac{\hat{\rho}\hat{u}_r}{\hat{r}} \tag{3.3}$$

$$\hat{\rho}\frac{D\hat{u}_x}{D\hat{t}} = -\frac{1}{\gamma}\frac{\partial\hat{p}}{\partial\hat{x}} + \frac{1}{Re^*_{ideal}}(\hat{\nabla}\cdot\hat{\tau})_x \tag{3.4}$$

$$\hat{\rho}\frac{D\hat{u}_r}{D\hat{t}} = -\frac{1}{\gamma}\frac{\partial\hat{p}}{\partial\hat{r}} + \frac{1}{Re^*_{ideal}}(\hat{\nabla}\cdot\hat{\tau})_r \tag{3.5}$$

$$\hat{\rho}\hat{c}_P\frac{D\hat{T}}{D\hat{t}} = \left(\frac{\gamma-1}{\gamma}\right)\hat{\beta}\hat{T}\frac{D\hat{p}}{D\hat{t}} - \frac{1}{Re^*_{ideal}\,Pr}(\hat{\nabla}\cdot\hat{q}'') + \frac{(\gamma-1)}{Re^*_{ideal}}\Phi \tag{3.6}$$

where both the *material derivative*, $D/D\hat{t} = \partial/\partial\hat{t} + \hat{u}_x\partial/\partial\hat{x} + \hat{u}_r\partial/\partial\hat{r}$, and the dimensionless *del operator*, $\hat{\nabla} = \vec{i}_x\partial/\partial\hat{x} + \vec{i}_r\partial/\partial\hat{r} + (1/\hat{r})\vec{i}_\theta\partial/\partial\theta$, have been introduced for compactness. While this dimensionless system of equations is mathematically equivalent to the original scalar system (Eq. 2.1 through Eq. 2.4), notice however, that the energy equation (*i.e.,* Eq. 2.4) has been replaced, for convenience, by Eq. (3.6), the dimensionless heat equation – a linear combination of the energy equation and the velocity inner product of the momentum equation. In the momentum equations the divergence of the shear stress tensor, $(\hat{\nabla}\cdot\hat{\tau})_x$ and $(\hat{\nabla}\cdot\hat{\tau})_r$, represents the net viscous forces per unit volume in the x-direction and r-direction respectively. In an analogous fashion the divergence of the heat flux vector, $(\hat{\nabla}\cdot\hat{q}'')$, in Eq. (3.6) represents the local efflux of heat. The viscous dissipation, Φ, is the rate of heat production due to the irreversible conversion of kinetic energy into internal energy. The mathematical

representations of these terms are shown below

$$(\hat{\nabla}\cdot\hat{\tau})_x = \frac{\partial}{\partial\hat{x}}\left(\frac{4}{3}\hat{\mu}\frac{\partial\hat{u}_x}{\partial\hat{x}}\right)+\frac{\partial}{\partial\hat{x}}\left(-\frac{2}{3}\hat{\mu}\frac{\partial\hat{u}_r}{\partial\hat{r}}\right)+\frac{\partial}{\partial\hat{r}}\left(\hat{\mu}\frac{\partial\hat{u}_r}{\partial\hat{x}}\right)+\frac{\partial}{\partial\hat{r}}\left(\hat{\mu}\frac{\partial\hat{u}_x}{\partial\hat{r}}\right) +\frac{1}{3}\frac{\hat{\mu}}{\hat{r}}\frac{\partial\hat{u}_r}{\partial\hat{x}}-\frac{\hat{\mu}}{\hat{r}}\frac{\partial\hat{u}_x}{\partial\hat{r}}-\frac{2}{3}\frac{\hat{u}_r}{\hat{r}}\frac{\partial\hat{\mu}}{\partial\hat{r}}$$

$$(\hat{\nabla}\cdot\hat{\tau})_r = \frac{\partial}{\partial\hat{x}}\left(\hat{\mu}\frac{\partial\hat{u}_r}{\partial\hat{x}}\right)+\frac{\partial}{\partial\hat{x}}\left(\hat{\mu}\frac{\partial\hat{u}_x}{\partial\hat{r}}\right)+\frac{\partial}{\partial\hat{r}}\left(-\frac{2}{3}\hat{\mu}\frac{\partial\hat{u}_x}{\partial\hat{x}}\right)+\frac{\partial}{\partial\hat{r}}\left(\frac{4}{3}\hat{\mu}\frac{\partial\hat{u}_r}{\partial\hat{r}}\right) +\frac{4}{3}\frac{\hat{\mu}}{\hat{r}}\frac{\partial\hat{u}_r}{\partial\hat{r}}-\frac{4}{3}\frac{\mu\hat{\hat{u}}_r}{\hat{r}^2}-\frac{2}{3}\frac{\hat{u}_r}{\hat{r}}\frac{\partial\hat{\mu}}{\partial\hat{r}}$$

$$\nabla\cdot\hat{q}'' = -\frac{\partial}{\partial\hat{x}}\left[\hat{k}\frac{\partial\hat{T}}{\partial\hat{x}}\right]-\frac{\partial}{\partial\hat{r}}\left[\hat{k}\frac{\partial\hat{T}}{\partial\hat{r}}\right]-\hat{k}\frac{\partial\hat{T}}{\partial\hat{r}}$$

$$\Phi = 2\hat{\mu}\left[\left(\frac{\partial\hat{u}_x}{\partial\hat{x}}\right)^2+\left(\frac{\partial\hat{u}_r}{\partial\hat{r}}\right)^2+\left(\frac{\hat{u}_r}{\hat{r}}\right)^2+\frac{1}{2}\left(\frac{\partial\hat{u}_x}{\partial\hat{x}}+\frac{\partial\hat{u}_r}{\partial\hat{x}}\right)^2\right]-\frac{2}{3}\hat{\mu}\left[\frac{\partial\hat{u}_x}{\partial\hat{x}}+\frac{\partial\hat{u}_r}{\partial\hat{r}}+\frac{\hat{u}_r}{\hat{r}}\right].$$

To complete the dimensional analysis the boundary conditions must also be considered. Normalizing the boundary conditions (see Section 2.6) follows the same procedure outlined above. The normalized wall temperature, T_{wall}/T^*, characterizes the wall thermal boundary condition, and the normalized back pressure, p_b/p^*, accounts for the case when the flow exits the nozzle at subsonic velocities. In the present study, however, the flow is taken to exit the nozzle at a supersonic velocity so that p_b/p^* is not relevant. This assumption is reasonable since experiments have not detected any changes in mass flow due to pressure perturbations downstream of the nozzle throat.

Neither the inlet boundary condition nor the centerline boundary condition yields any additional dimensionless parameters. Therefore, based on the set of governing equations the dimensionless parameters of interest include:

1. $Re^*_{ideal} = (4\ \dot{m}_{ideal})/(\pi\ d\ \mu_0)$, (Reynolds Number)
2. $\gamma = c_{Pi}/(c_{Pi} - R_{gas})$, (Specific Heat Ratio)
3. T_{wall}/T^*, (Thermal Boundary Condition)
4. $\hat{c}_P = c_P/c_{Pi}$, (Variation in Specific Heat)
5. $\hat{\mu} = \mu/\mu_0$, (Normalized molecular viscosity)
6. $\hat{k} = k/k_0$, (Normalized thermal conductivity)
7. $Pr = (\mu\ c_P)/k$, (Prandtl Number)
8. Z, (Compressibility Factor)
9. βT, (Normalized Coefficient of Volumetric Expansion)

Mathematically, the normalized solution vector, $\hat{Q}_p$, can be expressed as a function of the indicated dimensionless parameters as shown below

$$\hat{Q}_p = fnc(\hat{x}, \hat{r}, Re_{ideal}, \gamma, \frac{T_{wall}}{T^*}, \hat{c}_P, \hat{\mu}, \hat{k}, Pr, Z, \beta T). \tag{3.7}$$

The mass flow through the critical nozzle can be calculated by integrating the mass flux, ρu, over the throat cross sectional area as given by

$$\dot{m} = \int_0^{\frac{d}{2}} 2\pi r \rho u_x dr. \tag{3.8}$$

Dividing Eq. (3.8) by $\dot{m}_{ideal}$, C_d is given as

$$C_d = 8 \int_0^{\frac{1}{2}} \hat{r}\hat{\rho}\hat{u_x} d\hat{r}. \tag{3.9}$$

It follows that the functionality of the discharge coefficient is given in terms of the following dimensionless parameters

$$C_d = f_1 (Re^*_{ideal}, \gamma, \frac{T_{wall}}{T^*}, \hat{c}_P, \hat{\mu}, \hat{k}, Pr, Z, \beta T, geometry). \tag{3.10}$$

Thus, in critical nozzle flows where real gas behavior is important, the discharge coefficient is a function of nine dimensionless parameters in addition to the nozzle geometry. This set of dependent parameters can be reduced to six if the gas is considered to be a calorically perfect ideal gas (*i.e.* $c_P = constant$, $\rho = p/(R_{gas}T)$). In this case $\hat{c}_P$, βT, and the compressibility factor are unity and the functionality reduces to

$$C_d = f_2 (Re^*_{ideal}, \gamma, Pr, \frac{T_{wall}}{T^*}, \hat{\mu}, \hat{k}, geometry). \tag{3.11}$$

The simplified expression for the discharge coefficient given in Eq. (3.11) applies for gases that behave nearly ideally over the range of thermodynamic conditions typical of critical nozzle flows. However, this expression can also be used for gases where real gas effects are important by using the modified definition of the discharge coefficient

introduced by Johnson [21]–[24] and defined previously in Eq. (1.14). In the following sections we will define the procedure used for numerically calculating the discharge coefficient and compare numerical C_d predictions against both experimental data and analytical C_d predictions. Later, in Section 3.6 the effect that the dimensionless parameters in Eq. (3.11) have on the discharge coefficient is assessed.

3.2 Numerical Calculation of C_d

In experimental calibration procedures the discharge coefficient is defined as the ratio of the measured mass flow to a theoretical mass flow (refer to Eq. 1.3 or Eq. 1.14). For numerical predictions of the discharge coefficient, however, the computed mass flow, $\dot{m}_{CFD}$, is used in place of the measured mass flow, $\dot{m}_{exp}$. This section will discuss the procedure used for determining $\dot{m}_{CFD}$ from converged solutions of the Navier-Stokes equation. Convergence stipulations and treatment of discretization errors are also discussed.

The numerically predicted mass flow, $\dot{m}_{CFD}$, is determined by integrating the mass flux over an appropriate surface area within the nozzle. In the present work, the assumed symmetry about the nozzle centerline allows the surface integral for mass flow to be reduced to a path integral. For convenience the path of integration is taken to coincide with the grid lines that subdivide the nozzle at various cross sections (*i.e.,* grid lines of constant ξ). Thus, the computed mass flow passing through the i^{th} cross section is denoted by $\dot{m}_{CFD_i}$. Under steady state steady flow conditions,

$\dot{m}_{CFD_i}$ should theoretically remain the same constant value at each and every cross section. However, for numerical computations errors due to incomplete convergence and discretization errors result in a slight variation of the computed mass flow, $\dot{m}_{CFD_i}$, from one cross section to the next. These errors must be minimized in order to obtain the highest accuracy C_d predictions.

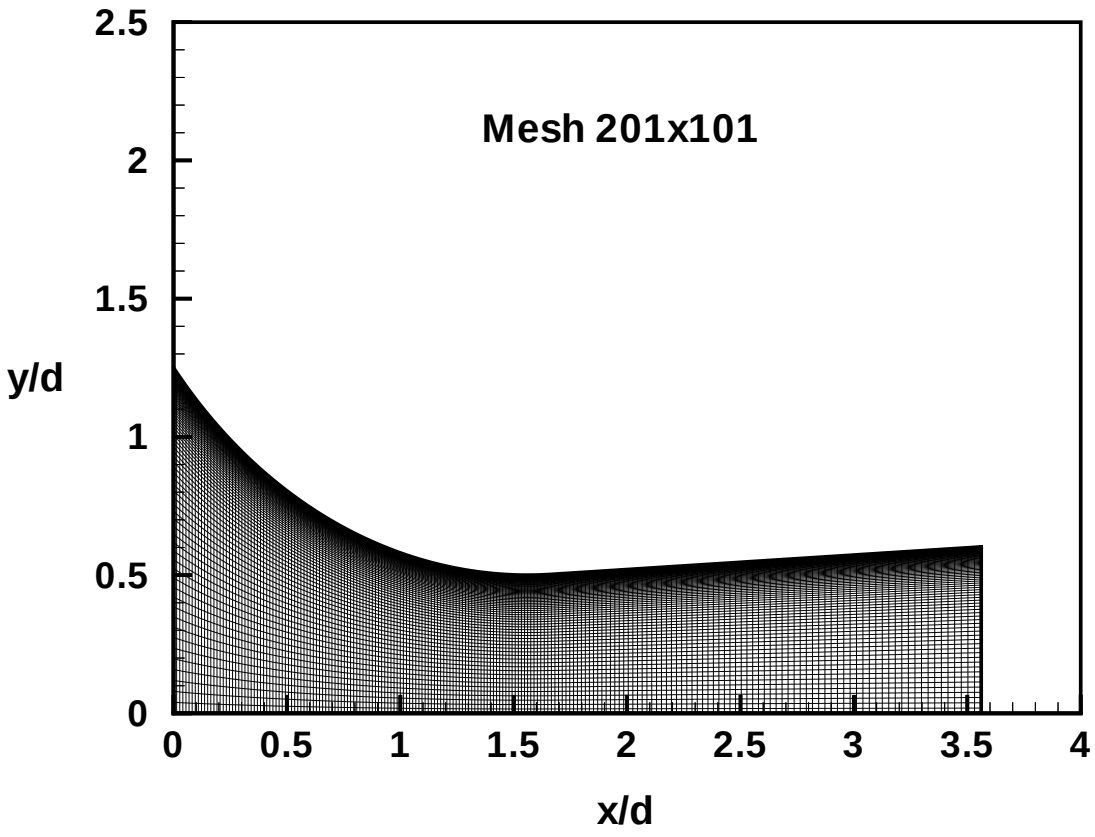

Figure 3.2. Mesh of nozzle geometry (201 by 101), $d = 0.5935\,\text{mm}$ and $\theta = 3\,\text{degrees}$.

To minimize the axial variation in the computed mass flow, the CFD simulations were converged to near machine accuracy and the grid mesh density was refined until $\dot{m}_{CFD_i}$ remained constant to within $\pm 0.005\,\%$ of the mean value at every cross

section where the mass flow was computed. Three different mesh densities varying from coarse to fine were used to assess the effect of discretization errors on mass flow predictions. The coarse grid consisted of 101 grid points in the axial direction and 51 grid points in the radial direction (*i.e.,* 101 by 51). In a similar manner, the mesh densities of the two finer grids consisted of 201 by 101 grid points and 401 by 201 grid points respectively. The same critical nozzle geometry was used for all three mesh densities. For these studies the upstream piping section was excluded so that the computational domain included only the converging-diverging nozzle section as shown schematically by the 201 by 101 mesh in Fig. (3.2).

Figure (3.3) compares the computed mass flow, $\dot{m}_{CFD_i}$, at several axial locations for the three mesh densities considered. The computed mass flow predictions correspond to N_2 gas flowing through a (d = 0.5935 mm) critical nozzle at $Re_{ideal} = 3847.4$. In the figure the normalized computed mass flow, $\dot{m}_{CFD_i}/\dot{m}_{ideal}$ is plotted versus the dimensionless advancing distance along the nozzle centerline, x/d, where d is the nozzle throat diameter. Of the three mesh densities considered, the finest mesh (401 by 201) yielded the most uniform $\dot{m}_{CFD_i}$ profile. For the finest mesh the maximum variation in $\dot{m}_{CFD_i}$ was less than 0.008 % excluding the nozzle inlet cross section (*i.e.,* the first grid point) where the computations of mass flow are expected to be adversely affected as a result of neglecting the inlet piping section. The mass flow at the inlet plane for both of the coarser meshes (*i.e.,* 201 by 101 and 101 by 51) was also affected by the inlet boundary condition. Figure (3.3) shows the disparity between $\dot{m}_{CFD_i}$ at

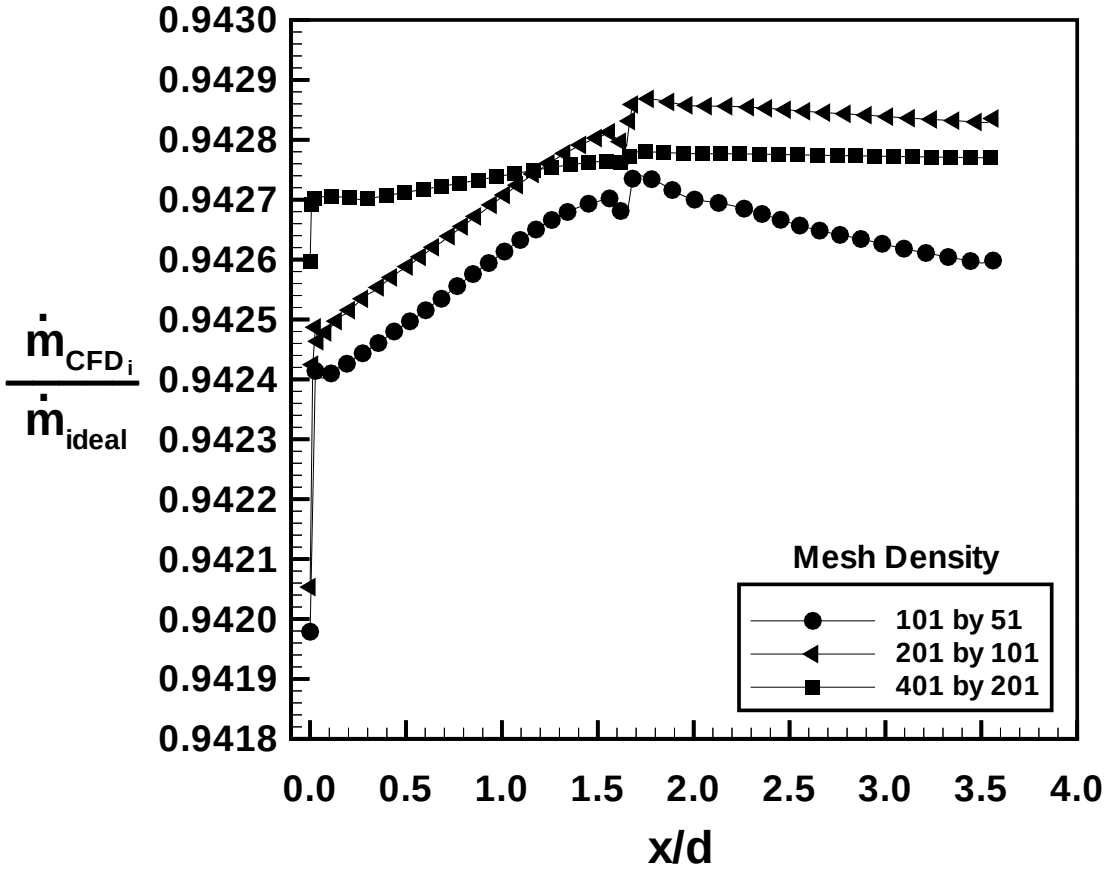

Figure 3.3. Axial variation in computed mass flow for three mesh densities.

the nozzle inlet and the remainder of the nozzle for each mesh density. In Section 3.6.5 it will be shown that including the piping section upstream of the nozzle inlet plane has a small effect on C_d and can be neglected.

When the Navier-Stokes equations have been converged to near machine accuracy, any remaining variation in $\dot{m}_{CFD_i}$ from one cross section to the next is primarily due to discretization errors. Figure (3.3) illustrates this point showing smaller variations of $\dot{m}_{CFD_i}$ as the mesh density increases. Note, however, that slight variations in the

computed mass flow persisted even at the highest mesh density, and therefore $\dot{m}_{CFD_i}$ was arithmetically averaged as given by

$$\dot{m}_{CFD} = \frac{1}{I_{max}} \sum_{i=1}^{I_{max}} \dot{m}_{CFD_i} \tag{3.12}$$

where I_{max} is the number of axial grid points. The average computed mass flow, $\dot{m}_{CFD}$, differs by only 0.0044 % (neglecting the first grid point) between the (401 by 201) mesh and the (201 by 101) mesh. Given that the percent difference in mass flow is almost two orders of magnitude less than the 0.2 % experimental uncertainty, and noting the considerable advantage in computation time efficiency, we chose to utilize the 201 by 101 grid size for all mass flow computations.

In this research the numerically predicted discharge coefficient is defined by

$$C_{d_{CFD}} = \frac{\dot{m}_{CFD}}{\dot{m}_{ideal}}. \tag{3.13}$$

Since we will be investigating small changes in C_d as a function of the previously mentioned dimensionless parameters we maintain a level of consistency by utilizing the same mesh density in all cases. By taking these precautions the CFD should faithfully indicate the correct C_d trends for various gas compositions and flow conditions.

3.3 Validation of Numerical Results.

In this section an equilibrium CFD model is used to compute the discharge coefficients for Ar, N_2, H_2, SF_6, and CO_2 gases over a range of Reynolds numbers varying from 2 000 to 40 000. The accuracy of these numerical predictions is determined by direct comparison against experimental calibration data. As explained previously in Section 1.5.3 of Chapter 1, real gas effects have been accounted for in the experimental calibration data so that to a good approximation the CFD model need not consider these effects. Subsequently, the equilibrium CFD model assumes a calorically perfect ideal gas (*i.e.,* $p = \rho R_{gas} T$ and $\gamma = constant$). In a later section, the equilibrium CFD model uses a real gas equation of state to ensure real gas behavior has been adequately accounted for using the approximate method discussed in Chapter 1.

The equilibrium CFD results follow the experimental calibration procedures whereby the Reynolds number is set by adjusting the stagnation pressure at a fixed stagnation temperature of $298.15\,K$. The wall thermal boundary condition is taken to be adiabatic and the molecular viscosity and thermal conductivity are determined from experimental data [56]. (The effect of assuming an adiabatic nozzle wall will be investigated in a later section.) As explained in Section 2.6 of the previous chapter, stagnation boundary conditions are prescribed at the nozzle entrance and the flow exiting the nozzle is taken to be fully supersonic.

The gases modeled in the numerical investigation (*i.e.,* Ar, H_2, N_2, SF_6, and CO_2)

have been selected to demonstrate the variable degree of difficulty of predicting the calibration performance of different gas species. Comparisons between the analytical model and the experimental data have indicated that certain gases are particularly difficult to model while others are fairly straightforward (see Fig. 1.6). There has been no explanation offered in the literature that explains why the analytical model works well for some gases but poorly for others. Furthermore, there is no criterion (besides direct comparison to experimental data) that distinguishes those gases that can be modeled using analytical techniques from those gases that are not suitable for analytical methods.

This investigation considers gases for which the analytical predictions compared well with experimental data (*e.g.,* Ar, H_2, and N_2) as well as gases where the agreement between the analytical model and calibration data was poor (*e.g.,* SF_6 and CO_2). Excluding the two problematic gases SF_6 and CO_2, the analytical predictions are within a fraction of a percent of the experimental data for all of the gases in Fig. (3.1). In spite of the good agreement for these gases (*i.e.,* Ar, He, O_2, H_2, N_2, C_2H_2, CH_4, and C_2H_6), the analytical C_d predictions exhibited a systematic bias based on the molecular structure of the gas. The discharge coefficient of the monatomic and diatomic gases (*e.g.,* Ar, He, O_2, H_2, and N_2) was slightly overpredicted by the analytical model. In contrast, for the polyatomic gases (*e.g.,* C_2H_2, CH_4, C_2H_6) the analytic model slightly underpredicted the experimental C_d values. In the case of SF_6 and CO_2 gases the underprediction was quite large, exceeding one percent for SF_6 and greater

than two percent for CO_2. Thus, the gases selected for this investigation should help assess if the equilibrium CFD model is capable of providing insight explaining the slight overprediction of C_d noted for the monatomic and diatomic gases or explaining the drastic underprediction observed for SF_6 and CO_2 gases.

In the remainder of this section the equilibrium CFD model is compared to the analytical model. Next, the equilibrium CFD results are compared to calibration data to assess any levels of improvement over analytical results. These comparisons are used to provide insight that could be useful for making improvements to the computational model. Finally, a sensitivity analysis is done to ascertain the sensitivity of various parameters on the discharge coefficient.

3.3.1 Comparison between Analytical and Equilibrium CFD Flow Model

Comparisons between the numerically predicted calibration curves, the analytical calibration curves [34], and the experimental calibration curves [35] are shown in Fig. (3.4) for the five gases considered. In each one of the five calibration plots the $\times$'s label the numerical data, the dashed line (- - -) represents the analytical data [34], and the $\bullet$'s label the experimental results [35]. The size of the $\bullet$'s represents the uncertainty of the experimental measurements. Note that the uncertainty due to nozzle throat diameter ($\pm$ 0.337%) is not included and will be discussed in detail in Section 3.6.6. In this section Fig. (3.4) is used to to compare the equilibrium CFD model to the analytical model.

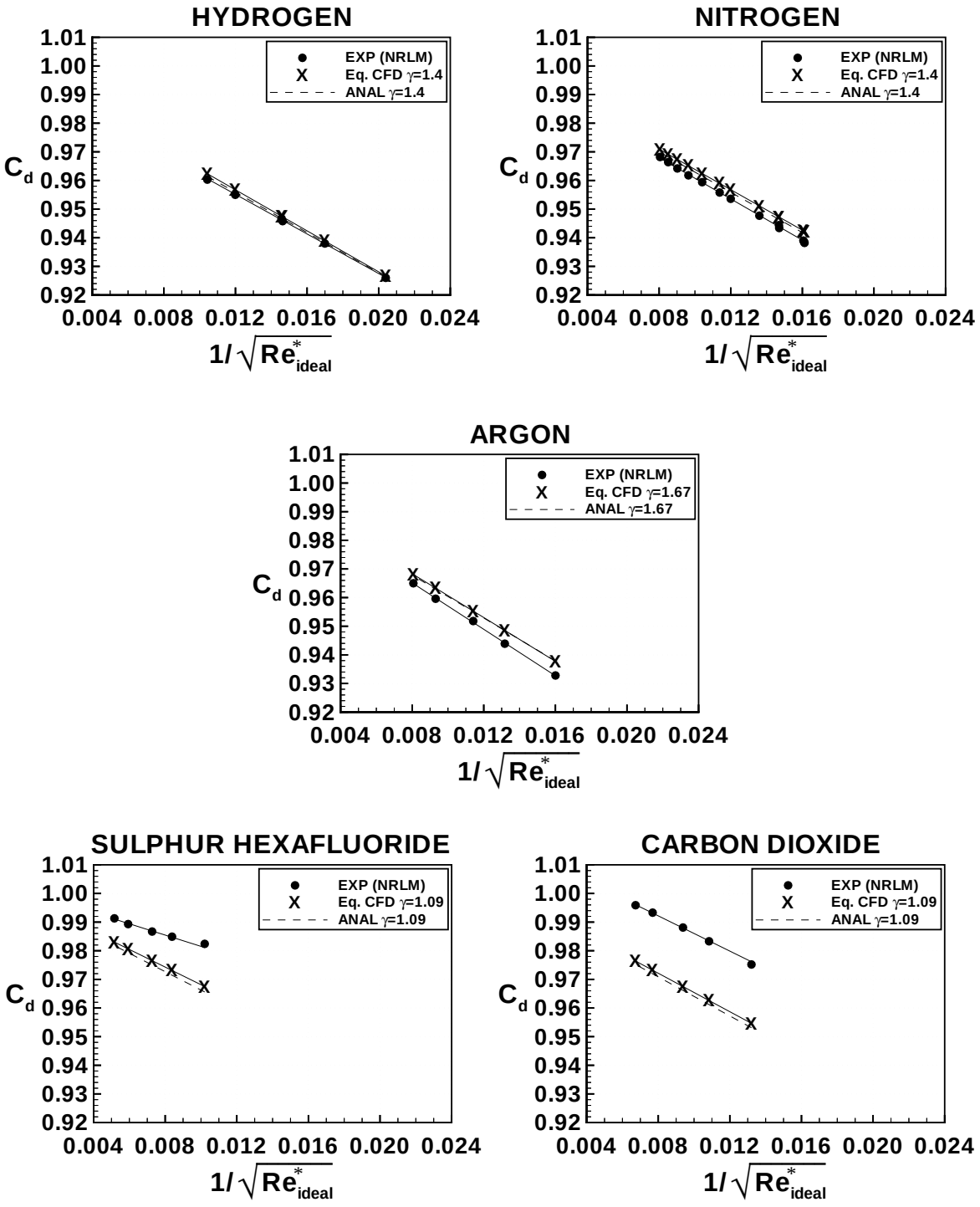

Figure 3.4. Comparison between analytical [22], equilibrium CFD, and experimental [23] sonic nozzle discharge coefficients for five gas species. (Adiabatic nozzle wall assumed in computations). $\gamma_{H_2} = 1.409$, $\gamma_{N_2} = 1.4$, $\gamma_{Ar} = 1.67$, $\gamma_{SF_6} = 1.09$, $\gamma_{CO_2} = 1.29$.

Figure (3.4) shows that the equilibrium CFD results are in good agreement with the analytical model of Ishibashi and Takamoto [34] for all the gases considered. In particular, both the numerical and analytical results exhibit a linear trend that agrees well in both slope and intercept. The largest difference between the two sets of data is less than 0.14 % in magnitude. This suggests that the composite boundary layer/inviscid core model of Ishibashi and Takamoto yields the same order of accuracy as the full equilibrium Navier-Stokes equations. Given that the analytical model is simpler to implement and less expensive to use, it should be used instead of the more involved CFD methods to make C_d predictions for those gases (*i.e.,* the monatomic and diatomic gases and some polyatomic gases) for which the analytical techniques are known to provide sufficiently accurate results.

Although the equilibrium CFD analysis did not improve upon analytical predictions, the equilibrium CFD model still provides useful information. The close agreement between the analytical and CFD results suggest that the various simplifications used in the analytical model (see Section 1.5) have little effect on C_d predictions. However, to eliminate the possibility that the good agreement between the analytical and numerical predictions could be caused by self-canceling errors attributed to the numerous assumptions used in the analytical model, the equilibrium CFD model is used to perform a sensitivity study of the various analytical assumptions. The result of the sensitivity analysis (performed in Section 3.6) confirms that the assumptions used in the analytical model are generally adequate over the range of thermodynamic

conditions considered.

3.3.2 Comparison between Calibration Data and Equilibrium CFD Model

A comparison between the experimental data [35] and the numerical results in Fig. (3.4) indicate fairly good qualitative agreement (*i.e.,* their slopes are similar). However, throughout the range of Reynolds numbers the two sets of data differ by a nearly constant offset. The direction (sign) of the offset follows the same trend observed in the analytical results. For the monatomic and diatomic gases, Ar, H_2, and N_2 the equilibrium CFD results slightly overpredict (*i.e.,* positive offset) the experimental C_d values. For these gases the maximum amount of the offset between the two sets of results is given by the following: +0.49 % Ar, +0.20 % H_2, and +0.43 % N_2. In contrast, the numerical predictions for the polyatomic gases CO_2 and SF_6 underpredict (*i.e.,* negative offset) the experimental measurements, and the largest magnitude of this error (-2.15 % for CO_2 and -1.76 % for SF_6) is several times larger than the errors observed for the other gases.

The adiabatic wall assumption, which is used in both the analytical and equilibrium CFD model, provides a plausible explanation for the modest overprediction observed for Ar, H_2, and N_2. The effect of the adiabatic wall boundary condition (as will be demonstrated in Section 3.6.2) is to increase the actual C_d values by approximately 0.05% to 0.3%. An increase in C_d of this magnitude could partially explain why the analytical and numerical models overpredict the experimentally measured discharge

coefficients. On the other hand, the predicted C_d values for both SF_6 and CO_2 gases are significantly lower than experimental observations, and there are no obvious explanations to account for these dramatic differences.

Further insight about the noted discrepancies for CO_2 and SF_6 gases can be obtained by comparing the values of slope and y-intercept for calibration curves shown in Fig. (3.4). Linear regression is used to determine the slope and y-intercept of the calibration data so that C_d is given by a two parameter model

$$C_d = \alpha - \beta/\sqrt{Re^*_{\text{ideal}}}. \tag{3.14}$$

where the parameter α is the y-intercept of the calibration curve (see Fig. 3.4) and β is the magnitude of its slope. Physically, α represents the discharge coefficient for an inviscid flow (*i.e.*, $Re^*_{\text{ideal}} \to \infty$) and it is a measure of the influence of multi-dimensional phenomenon on the discharge coefficient. The parameter β is proportional to the reduction in C_d due to viscous effects and is therefore related to the displacement thickness.

Gas	α_{exp}	α_{num}	$\alpha_{\%diff}$	β_{exp}	β_{num}	$\beta_{\%diff}$
Ar	0.9976	0.9990	+0.14	4.053	3.830	-5.50
N_2	0.9970	0.9992	+0.22	3.618	3.531	-2.40
H_2	0.9967	0.9995	+0.28	3.458	3.568	+3.18
SF_6	0.9990	0.9998	+0.08	1.744	3.085	+76.89
CO_2	1.0168	0.9989	-1.76	3.077	3.370	+9.52

Table 3.1. Functionality of two-parameter calibration curves on gas species.

Because α and β have physical interpretations, the magnitude of these quantities have physical implications that hint toward some possible explanations for the poor C_d predictions noted for SF_6 and CO_2 gases. Table (3.1) shows both the numerical and experimental values of α and β for the five gas species considered. Similar to the trends observed for C_d, the equilibrium CFD model slightly overpredicts α for Ar, N_2, and H_2 while marginally underpredicting α for SF_6 and grossly underpredicting α for CO_2. Moreover, the experimental value of α for CO_2 is greater than unity. The larger than unity value for the experimental inviscid discharge coefficient, α_{exp}, cannot be explained by traditional inviscid compressible flow mechanisms which predict less than unity α values. A likely explanation for this contradiction points toward physical mechanisms existing in the actual flow that have not been adequately accounted for in either the analytical model or equilibrium CFD analysis.

The comparison between the experimental and numerical values for β in Table (3.1) show adequate agreement for Ar, H_2, and N_2, slightly poorer agreement for CO_2, and very poor agreement for SF_6. Furthermore, the experimental value of β for SF_6 is significantly different from the values of β_{exp} noted for the other gases. Given that β is related to the displacement thickness, one possible explanation for the sub par C_d predictions for SF_6 could be attributed to unique boundary layer phenomenon occurring for this gas. This explanation, however, seems unlikely, based on the theoretical understanding of boundary layer development.

For critical nozzle flow through a given nozzle geometry, the predominant dimensionless parameters that govern boundary layer development include the Reynolds number, the Prandtl number, the specific heat ratio, the wall thermal boundary condition, and to a lesser extent the variable (*i.e.,* non-uniform) transport properties. It follows that the discharge coefficient is a function of these parameters as demonstrated previously by Eq. (3.11). In general, each gas has a unique value for Prandtl number, and specific heat ratio, etc. so that the discharge coefficient will vary for each gas species even at a specified Reynolds number. However, the results of the sensitivity analysis done in Section 3.6 show that the functional dependence of the discharge coefficient on these parameters is relatively weak and not sufficient to explain the noted discrepancies for SF_6 gas.

A second possible explanation again points toward the possibility that neither the analytical model nor the equilibrium CFD model takes into account all of the important physical mechanisms occurring in the real flow. The traditional flow mechanisms considered to affect the discharge coefficient include viscous effects, multi-dimensional phenomenon, and real gas behavior. However, if flow mechanisms other than those considered traditionally can affect the calibration performance of certain gas species, understanding the pertinent physics governing these mechanisms would seem to be of significant interest to the flow metering community. Such knowledge would greatly increase the practical value of both analytical and computational predictive models. In particular, gases could be classified according to whether or not their calibration

performance is affected by *non-traditional* flow mechanisms. For gases affected only by *traditional* flow mechanisms, the existing analytical techniques suffice to provide reliable C_d predictions. For gases affected by both *traditional* and *non-traditional* flow mechanisms, modified CFD algorithms could be used to provide improved C_d predictions.

3.4 NIST Measurements for CO_2

Both CO_2 and SF_6 gases exhibited very unique calibration characteristics in comparison to the other gases shown in Fig. (3.1). The two parameter model showed that the experimental β parameter for SF_6 deviated by nearly 100 % with β_{exp} values for the other gases (see Table 3.1). Moreover, the experimental data yielded a greater than unity value for the inviscid discharge coefficient, α_{exp}, for CO_2 gas. This larger than unity value of α is in contradiction with the less than unity values predicted by well established compressible flow theories. In light of these peculiarities, it is important to verify that the reported calibration data is repeatable and can be reproduced in another laboratory before searching for physical explanations for the unique calibration characteristics. Therefore, the NRLM experimental measurements for CO_2 were replicated in the NIST calibration laboratory.

In the experiment conducted at NIST a small throat diameter nozzle was calibrated using a piston prover primary standard [10] over a range of Reynolds numbers similar to the NRLM calibrations. Two different types of nozzles were used for these

experiments. The NIST experiment used a cylindrical throat nozzle while the NRLM experiment used a toroidal throat nozzle (refer to Fig 1.2 and Fig 1.3 shown previously in Chapter 1). Although the nominal throat diameter of both the NIST nozzle ($d = 0.3\,mm\ \pm 2\,\%$) and the NRLM nozzle ($d = 0.5935\,mm\ \pm 0.167\,\%$) were comparable, the uncertainty in the throat diameter of the NIST nozzle was more than an order of magnitude larger than that of the NRLM nozzle. The larger uncertainty for the NIST nozzle significantly affected the absolute values of the measured discharge coefficients (see Eq. 1.2 and Eq. 1.3) and ultimately prevented the NIST measurements from being directly compared to the NRLM measurements.

The net effect of uncertainties in the nozzle throat diameter is to vertically shift the entire calibration curve (see Section 3.6.6). The calibration curve will be shifted upwards if the diameter used to calculate $\dot{m}_{ideal}$ (*i.e.,* the theoretical mass flow used in the definition of the discharge coefficient, $C_d = \dot{m}_{exp}/\dot{m}_{ideal}$) is smaller than the actual diameter and the calibration curve will be shifted downwards if the diameter used to calculate $\dot{m}_{ideal}$ is larger than the actual diameter. In either case, the measured C_d values will be offset by the nearly the same amount over the entire range of Reynolds numbers regardless of the calibration gas. Therefore, the NIST experiments were used to calibrate the cylindrical throat nozzle for two gases, both CO_2 and N_2. The experimental results compared the magnitude of the C_d offset between the two gases to the C_d offset measured in the NRLM data set between the same two gases.

The NIST calibration curves for CO_2 and N_2 are shown in Fig. (3.5). The 3 % offset

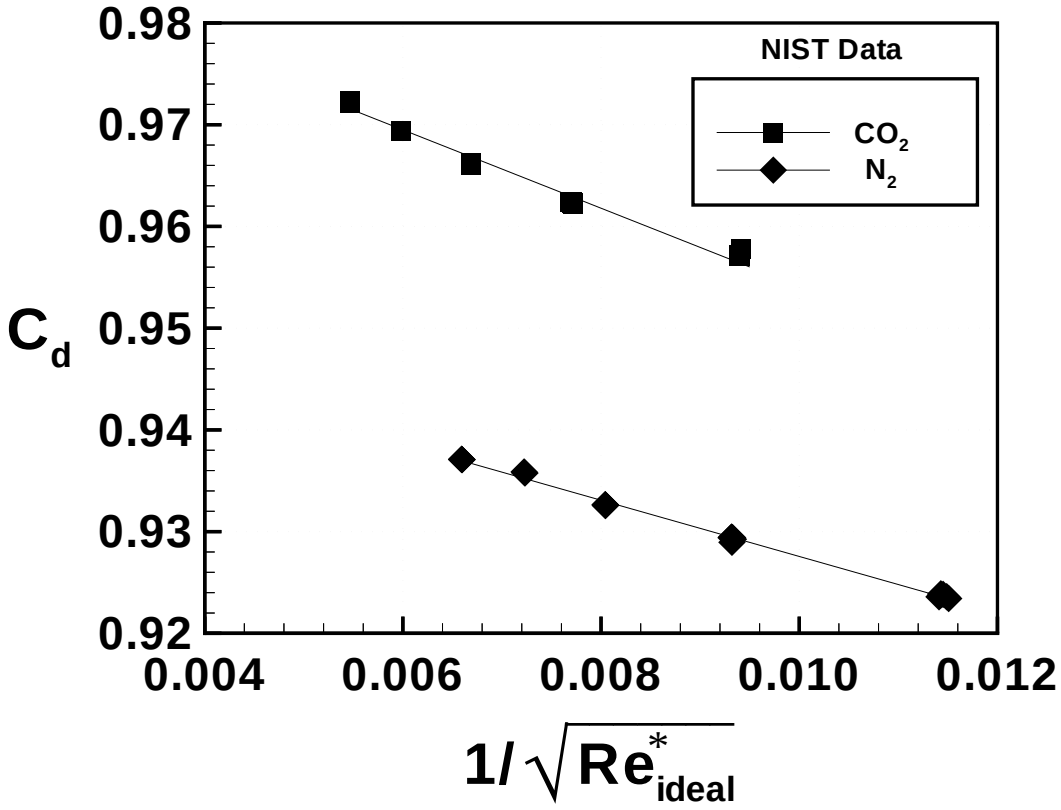

Figure 3.5. NIST comparison between calibration curves for CO_2 and N_2 gases.

observed between CO_2 and N_2 calibration curves in the NIST data was nearly identical to the 2.8 % offset between the same two gases observed in the NRLM data (compare Fig. 3.1 to Fig. 3.5). Hence, the NIST data helped confirm that the unusual calibration characteristics observed for CO_2 gas can be attributed to a physical phenomenon and not due to experimental bias.

3.5 The Effect of Real Gas Behavior on C_d

Thus far real gas effects have not been accounted for directly within the CFD model. Instead, real gas effects have been taken into account in an approximate manner by appropriately weighting the measured values of the discharge coefficient as explained in Section 1.5.3. This approximate method of accounting for real gas behavior yields its best results for those gases (*e.g.,* Ar, H_2, and N_2) that behave nearly ideally over the range of thermodynamic conditions. On the other hand, for gases such as CO_2 and SF_6, real gas effects are more significant and this approximate method is less accurate, and could in part be responsible for the inability to predict the calibration characteristics of CO_2 and SF_6 gases. In this section a new set of computations based on the equilibrium CFD model is made and presented. For these new computations a real gas equation of state is used.

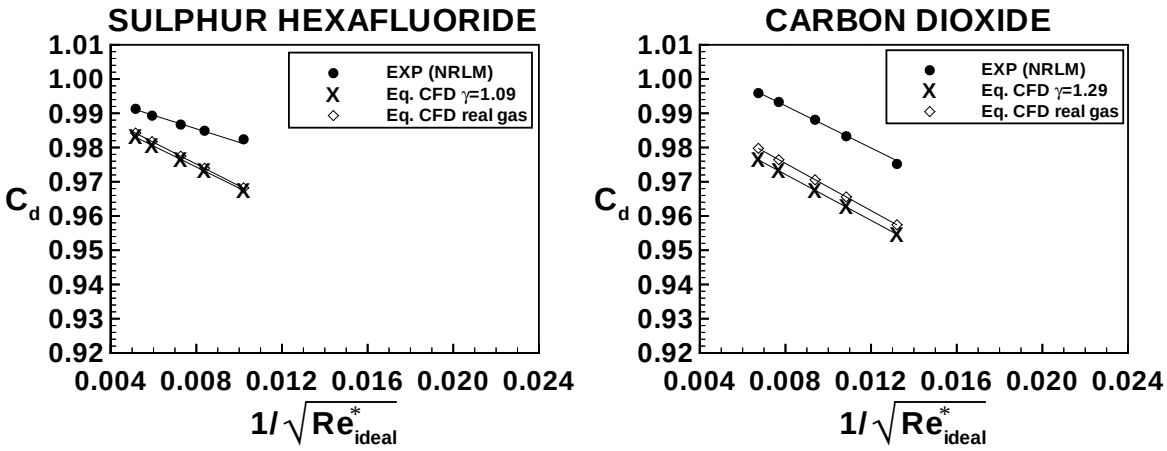

Figure 3.6. Comparison between equilibrium CFD with ideal gas equation of state and $\gamma = 1.29$, equilibrium CFD with real gas equation of state, and experimental [23] sonic nozzle discharge coefficients for CO_2 and SF_6 gases. (Adiabatic nozzle wall assumed in computations).

Figure (3.6) compares the results of two CFD simulations (*i.e.,* ideal gas and real gas) to experimental data. Comparisons between the ideal gas CFD model and the real gas CFD model indicate that real gas effects have not been totally accounted for by using the approximate method discussed in Section 1.5.3. Furthermore, for both SF_6 and CO_2 gases, including real gas behavior in the CFD model slightly improves the level of agreement between C_d predictions and measured values. Thus, including real gas effects directly in the computational model yielded an improvement of 0.3 % for CO_2 gas and a 0.1 % improvement for for SF_6 gas. However, the improvement is not nearly enough to explain the unique calibration behavior for either CO_2 or SF_6 gas.

3.6 Effect of Various Dimensionless Parameters on C_d

The discharge coefficient of critical nozzle flows has traditionally been considered to be fully characterized by the following three mechanisms: viscous effects, multi-dimensional phenomenon, and real gas behavior. However, the discharge coefficient of certain gases, such as CO_2 and SF_6, can not be fully explained in terms of these traditional flow mechanisms. In Chapter 4 we will show that vibrational relaxation is responsible for the unique calibration characteristics of these polyatomic gases. On the other hand, gases that are not affected by vibrational relaxation (*e.g.,* monatomic gases, diatomic gases, and some polyatomic molecules) have been shown to be well characterized by the traditional flow mechanisms.

The analytical model has been used to make reasonably accurate C_d predictions for gases that are not affected by vibrational relaxation phenomenon. The analytical model, however, makes numerous simplifying assumptions in order to obtain closed-form solutions (see Section 1.5). Many of these assumptions can not be physically justified and there is no way of quantifying their effects on analytical C_d predictions. The dimensional analysis done in Section 3.1 gives the functionality of the discharge coefficient in terms of the Reynolds number, the Prandtl number, the wall thermal boundary condition, the specific heat ratio, and the variable transport properties (see Eq. 3.11). The following sections will assess the importance of these parameters by determining their influence on C_d. Of particular interest is the magnitude of C_d change as a result of varying these parameters, the direction of the C_d change (*i.e.,* increase or decrease), and the physical mechanisms responsible for the effect. In this way we can evaluate the merit of various assumptions used in the analytical model with regard to the model's overall accuracy.

3.6.1 Effect of Prandtl Number

The analytical treatment of viscous effects [28]–[34] (described previously in Section 1.5.2 of Chapter 1) makes the fundamental assumption of equality between the magnitudes of molecular and thermal diffusivity (*i.e.,* $Pr = 1$). Although most gases used in critical nozzle applications have $Pr \approx 0.7$ over a wide range of thermodynamic conditions (see Ref. [53]), the unity Prandtl number assumption appears to be

warranted based on the close agreement between numerical and analytical results [34] shown earlier in Fig. (3.4). In what follows, a sensitivity analysis is performed to quantify the effect between $Pr = 1.0$ (*i.e.,* assumed in analytical models) and $Pr = 0.7$ (*i.e.,* actual value for most gases) on C_d. For this comparison the 201 by 101 mesh is used, the nozzle wall is taken to be adiabatic, and upstream stagnation boundary conditions are enforced. We assume constant specific heat and determine density via the ideal gas equation of state. The experimental data [56] is used to determine the molecular viscosity as a function of temperature, and the thermal conductivity is determined for the selected (constant) value of Prandtl number (*i.e.,* $k = \mu c_P/Pr$). The results here presented are for N_2, but their implications apply to other gas species as well.

Under the assumptions of ideal gas and unity Prandtl number, the rate of work done by viscous forces is balanced by the conduction heat losses within the thermal boundary layer. When $Pr < 1$, the ability of a thermal boundary layer to effectively diffuse heat generated by viscous dissipation is enhanced. Consequently, radial conduction distributes heat over a larger affected volume (*i.e.,* a thicker thermal boundary layer) leading to lower temperatures near the wall and slightly higher temperatures near the free stream. Fig. (3.7) compares the normalized throat radial temperature distributions, T/T^*, for $Pr = 1$ and $Pr = 0.7$, illustrating this effect. The figure only illustrates the behavior close to the wall given that outside of the thermal boundary layer the influence of Pr is negligible.

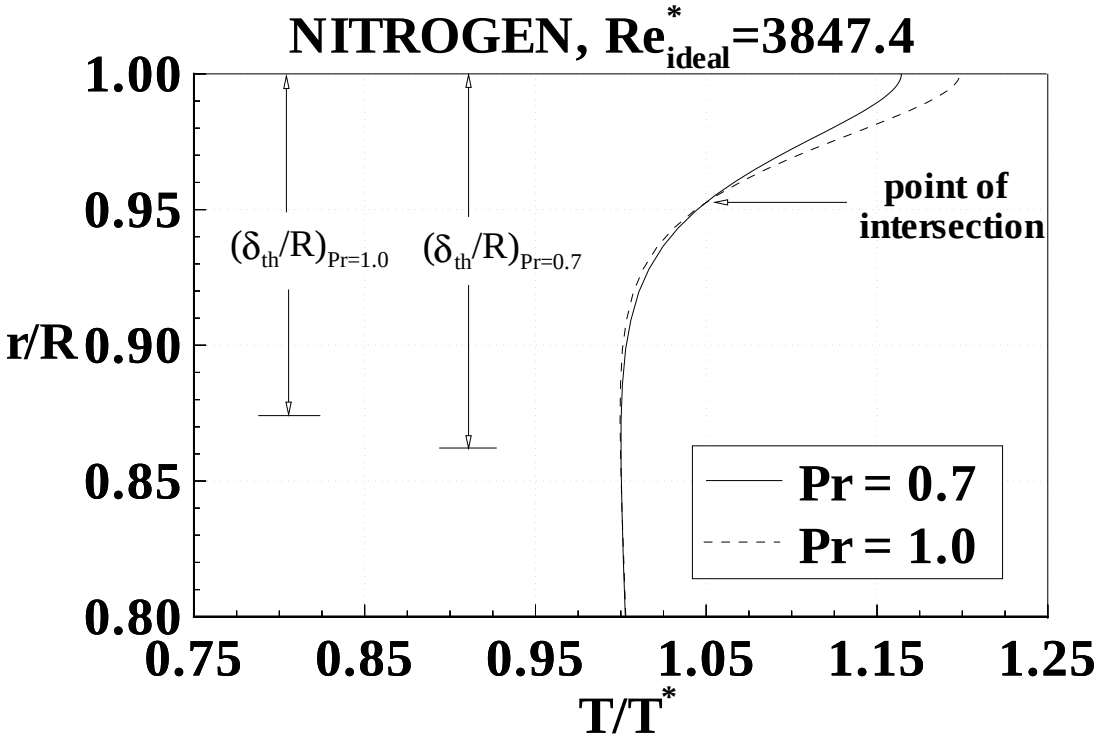

Figure 3.7. Effect of Prandtl number on heat dissipation near the wall (nozzle throat radial temperature profiles). —— $Pr = 0.7$; - - - $Pr = 1.0$. [Included in the figure are the thermal boundary layer thicknesses: $(\delta_{\rm th}/{\rm R})\big|_{\rm Pr=0.7} = 0.138$; $(\delta_{\rm th}/{\rm R})\big|_{\rm Pr=1.0} = 0.126$).]

As shown in Fig. (3.7) the temperature distribution within the thermal boundary layer only changes slightly when Pr is reduced from $Pr = 1$ to $Pr = 0.7$. Specifically, $T_{Pr=0.7}$ is lower than $T_{Pr=1.0}$ near the wall ($\approx 2.8\,\%$ lower) while the trend reverses further away from the wall ($0.862 \geq r/R \geq 0.952$) where $T_{Pr=0.7}$ is $\approx 0.33\,\%$ higher than $T_{Pr=1.0}$. The changes in pressure and velocity due to changes in Pr are small, and therefore the density varies nearly inversely with temperature, increasing near the wall ($+2.77\,\%$) and decreasing slightly ($-0.49\,\%$) near the free stream. The difference in the radial density profile when $Pr < 1$ is the predominant factor controlling the difference in the streamwise throat mass flux distribution (*i.e.*, not velocity). The

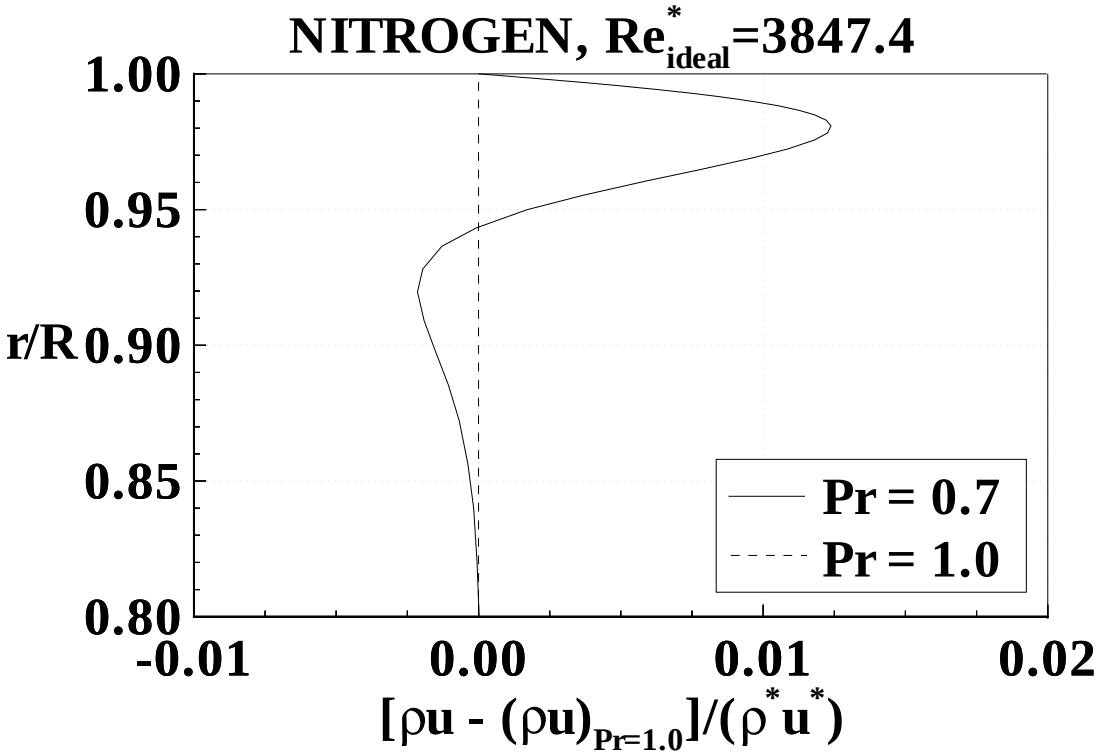

Figure 3.8. Difference in streamwise mass flux for $Pr = 0.7$ and $Pr = 1.0$ (adiabatic wall condition)

difference in the mass flux profiles between $Pr = 0.7$ and $Pr = 1.0$ is shown in Fig. (3.8). (Note that the abscissa has been chosen so that integrating across the throat cross section yields the difference in C_d between the two Pr). This figure shows that the increase of mass flux near the wall more than compensates for the deficit of mass flux near the free stream, and thus, the overall average mass flux increases as Pr decreases from unity.

The mass flux profiles of Fig. (3.8) were integrated across the throat cross section to determine C_d, and the functionality of C_d with Pr is shown in Fig. (3.9). In addition to $Pr = 0.7$ and $Pr = 1.0$, we considered $Pr = 0.1$ and $Pr = 10.0$ (although not physically attainable for most gases) to clearly illustrate the effect of Pr on C_d

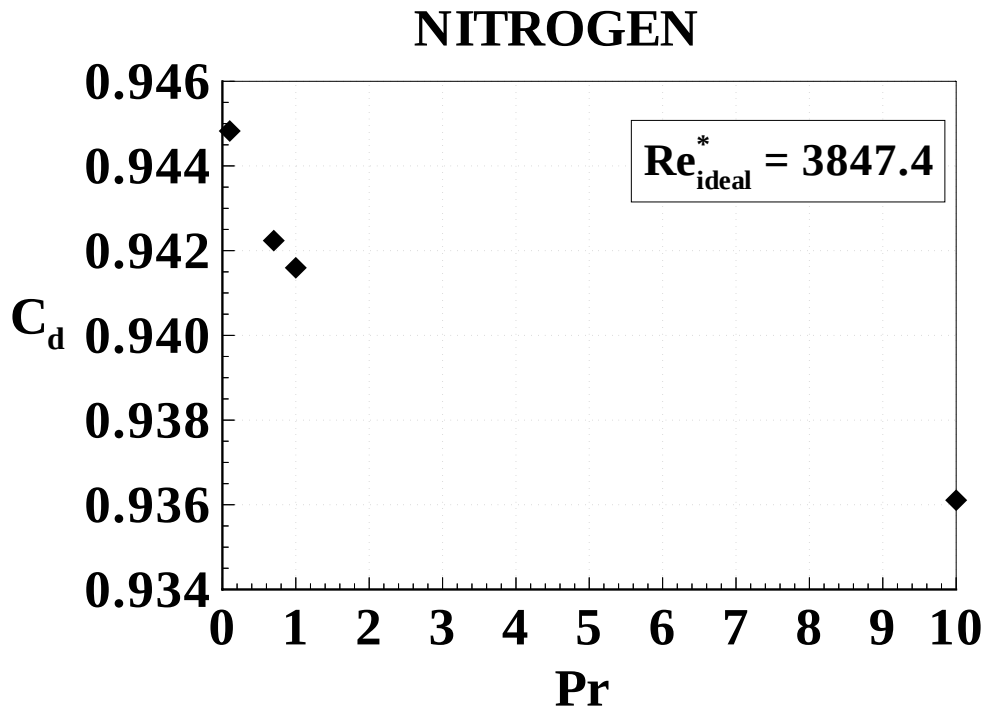

Figure 3.9. C_d variation versus Pr (adiabatic wall condition)

for an adiabatic wall condition. The figure shows that C_d increases monotonically as Pr is decreased. The difference between C_d for the value of $Pr = 1.0$ (used in analytic models) and $Pr = 0.7$ (value for most gases) is 0.06 %. The 0.06 % is a moderately sized factor in comparison to the $0.2\dot{\%}$ experimental uncertainty. However, this error is expected to decrease at higher Reynolds numbers where boundary layer phenomenon is less significant for the determination of mass flow. Therefore, the unity Prandtl number assumption is warranted in analytical models (especially at high Reynolds numbers) given the dramatic simplifications it allows while introducing only a relatively small error.

3.6.2 Effect of Wall Thermal Boundary Condition

The adiabatic wall condition ($\partial T/\partial n = 0$) is used in the composite analytical model of Ishibashi and Takamoto [34], as well as in the equilibrium CFD computational model. For critical nozzles under normal calibration conditions ($T_{\text{amb}} = T_0$, $Re^*_{\text{ideal}} >> 1$, and $Pr \approx 0.7$) the adiabatic wall assumption seems to be justified by the relatively good agreement between experimental [34] and numerical results shown previously in Fig. (3.4). However, the assumption is not strictly valid. Under normal calibration conditions the ambient temperature is slightly larger than the adiabatic wall temperature (*i.e.,* the wall temperature profile for an insulated wall) and heat flows from the environment into the fluid. Since even small changes in C_d (*i.e.,* less than a fraction of a percent) are of interest here, we will investigate the effect of the wall thermal boundary condition on the discharge coefficient. The sensitivity of the discharge coefficient to wall thermal boundary conditions is determined by comparing C_d predictions for an adiabatic wall condition with predictions for a "hot" wall condition, $T_{\text{wall}} = T_{\text{amb}}$ (298.15 K). Note that this analysis applies only for normal calibration conditions where the inlet stagnation temperature is equal to the ambient temperature.

Physically, the hot wall condition ($T_{\text{wall}} = T_{\text{amb}}$) represents the maximum attainable wall temperature (under normal calibration conditions). Therefore, this investigation determines the maximum possible influence that the adiabatic wall assumption can have on the discharge coefficient. For the hot wall condition the effect of heat transfer

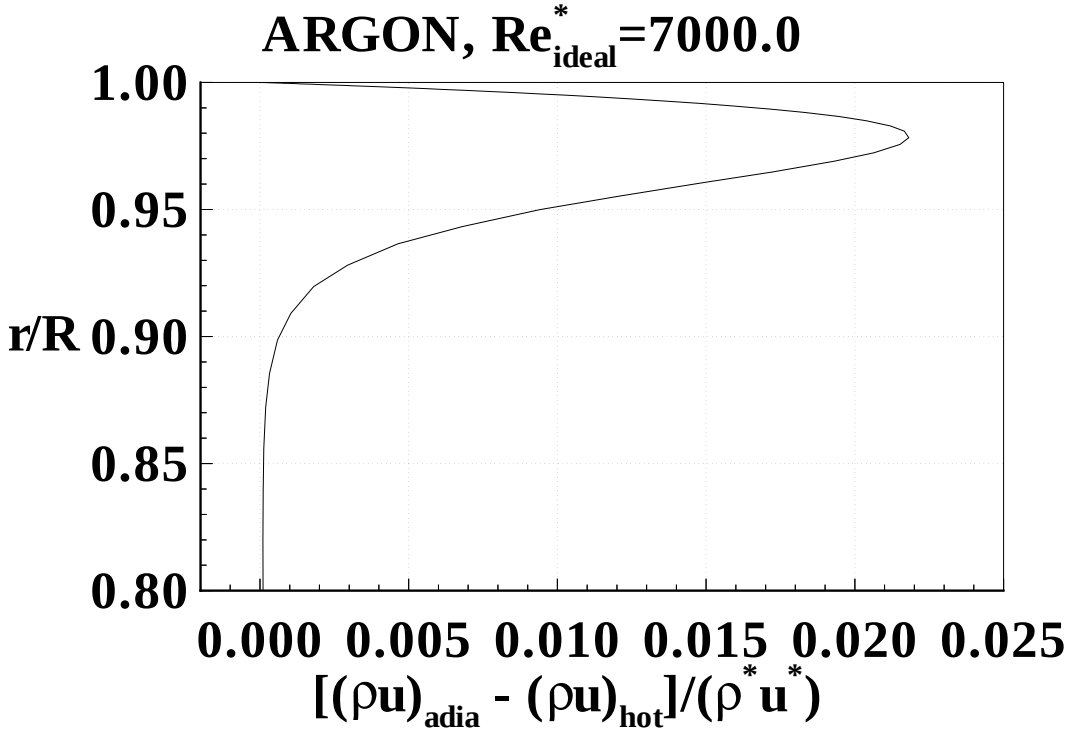

Figure 3.10. Difference of mass flux between an adiabatic wall and a hot wall at the nozzle throat for $Re^*_{\text{ideal}} = 7\,000$.

is predominately confined to a thin region near the wall denoted as the thermal boundary layer. Increased temperatures in this region decrease both the density, and to a lesser extent, the flow velocity, thus resulting in a lower mass flux. Figure (3.10) shows the difference in throat mass flux profiles within the thermal boundary layer between the adiabatic wall condition and the hot wall condition for a typical flow. For the adiabatic wall condition the mass flux through the thermal boundary layer is larger than the mass flux for the hot wall condition so that the corresponding adiabatic wall condition discharge coefficient is larger than the hot wall discharge coefficient (*i.e.*, $C_{d,\text{adia}} > C_{d,\text{hot}}$).

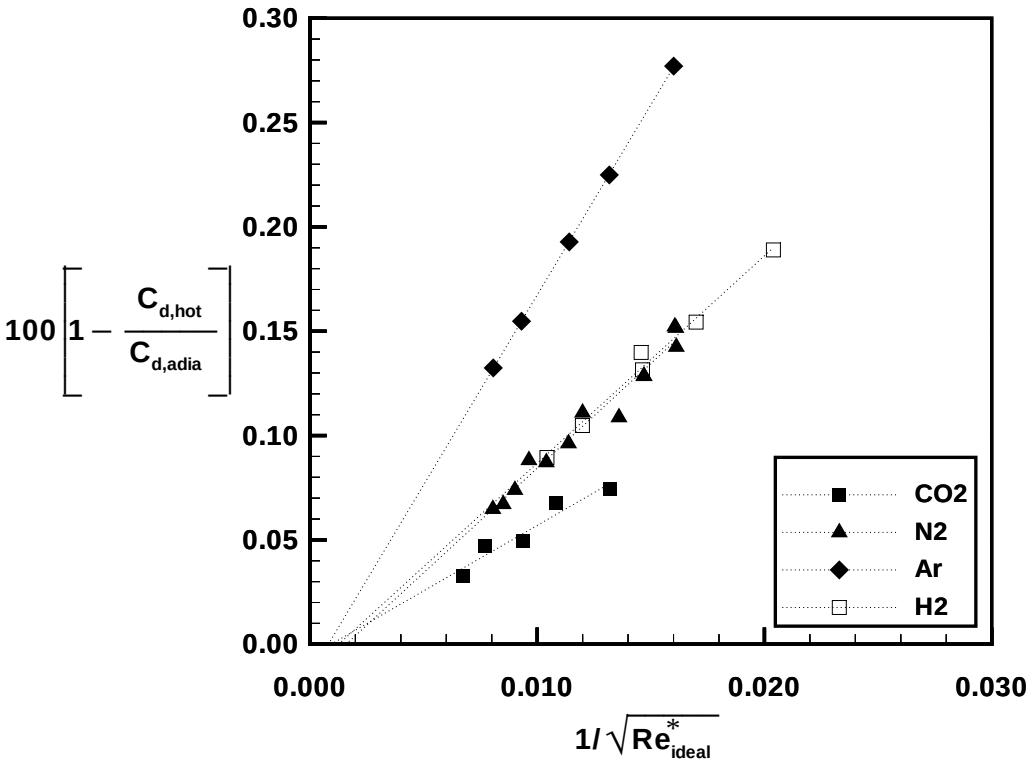

Figure 3.11. Percent change in numerical discharge coefficient versus throat Reynolds number for Ar, H_2, N_2, and CO_2 for an adiabatic wall and hot wall.

The sensitivity of discharge coefficient on the wall thermal boundary condition depends on both γ and Re^*_{ideal}. Note that the Prandtl number also plays a role, but the variation in Pr among gases is small (*i.e.,* most gases have $Pr \approx 0.7$), thereby reducing the significance of this parameter. Figure (3.11) shows the numerical results for the change in C_d between an adiabatic wall and a hot wall for Ar, H_2, N_2, and CO_2. The effect of the wall thermal boundary condition is seen to be greatest at the lowest Re^*_{ideal} for all the gas species. At larger Re^*_{ideal}, forced convection heat transfer from the nozzle wall is enhanced, thus shrinking the thermal boundary layer

and decreasing the effect of heat transfer. In the limit $Re^*_{\text{ideal}} \to \infty$ the difference in C_d becomes negligible ($\Delta C_d \to 0$) which indicates that C_d has little sensitivity to the wall thermal boundary condition at large Re^*_{ideal}.

The sensitivity of C_d to the wall thermal boundary condition increases for gas species with larger γ. The effect that gas species have on the wall thermal boundary condition is also shown in Fig. (3.11). Gases with larger γ are more significantly affected by the wall thermal boundary condition since larger γ's result in lower free stream throat temperatures, which in turn, cause the temperature difference responsible for heat transfer to increase. Increased heat transfer leads to decreased mass flux throughout the thermal boundary layer, and therefore, gases with larger γ are more sensitive to the wall thermal boundary condition than gases with lower γ.

3.6.3 Effect of Specific Heat Ratio

The specific heat ratio, γ, plays an important role in determining the discharge coefficient. Specifically, for gases that are not expected to be affected by vibrational non-equilibrium phenomenon (*e.g.,* monatomic, diatomic and some polyatomic gases) experimental data shows that the discharge coefficient tends to increase as γ decreases (see Fig.3.1). To quantify the magnitude and direction of this effect a sensitivity analysis is performed where all relevant parameters except the specific heat ratio are held constant.

For the sensitivity analysis N_2 gas with $\gamma = 1.4$ was used as the baseline case. Two other simulations were also done where the specific heat ratio was arbitrarily set equal to $\gamma = 1.1$ and $\gamma = 1.67$ to determine the sensitivity of C_d to changes in γ. While γ was systematically varied, the other important dimensionless parameters affecting the discharge coefficient (*i.e.,* Reynolds number and Prandtl number) were maintained at the same constant value so that any change in C_d is due to only to value of γ. Note that the transport properties for N_2 gas are used in all simulations and the wall thermal boundary condition was taken as adiabatic. Real gas effects are accounted for in the weighting of the experimental discharge coefficients so that the CFD model uses a calorically perfect equation of state.

Figure (3.12) shows numerically predicted calibration curves for the three different values of γ. The results of the numerical simulations are in good agreement with experimental findings in that the numerically predicted C_d values are larger for lower values of γ. The largest offset between the three calibration curves occurs at the lowest Reynolds numbers where the difference between the $\gamma = 1.1$ simulation and the $\gamma = 1.67$ simulation is almost two percent. The magnitude of this offset, however, decreases to within a few tenths of a percent at the highest Reynolds numbers.

The effect of the specific heat ratio on the discharge coefficient is primarily a boundary layer phenomenon. Therefore, the calibration curves shown in Fig. (3.12) converge toward one another at higher Reynolds numbers where the boundary layer thins. Physically, the thinner boundary layer occurring at the higher Reynolds numbers

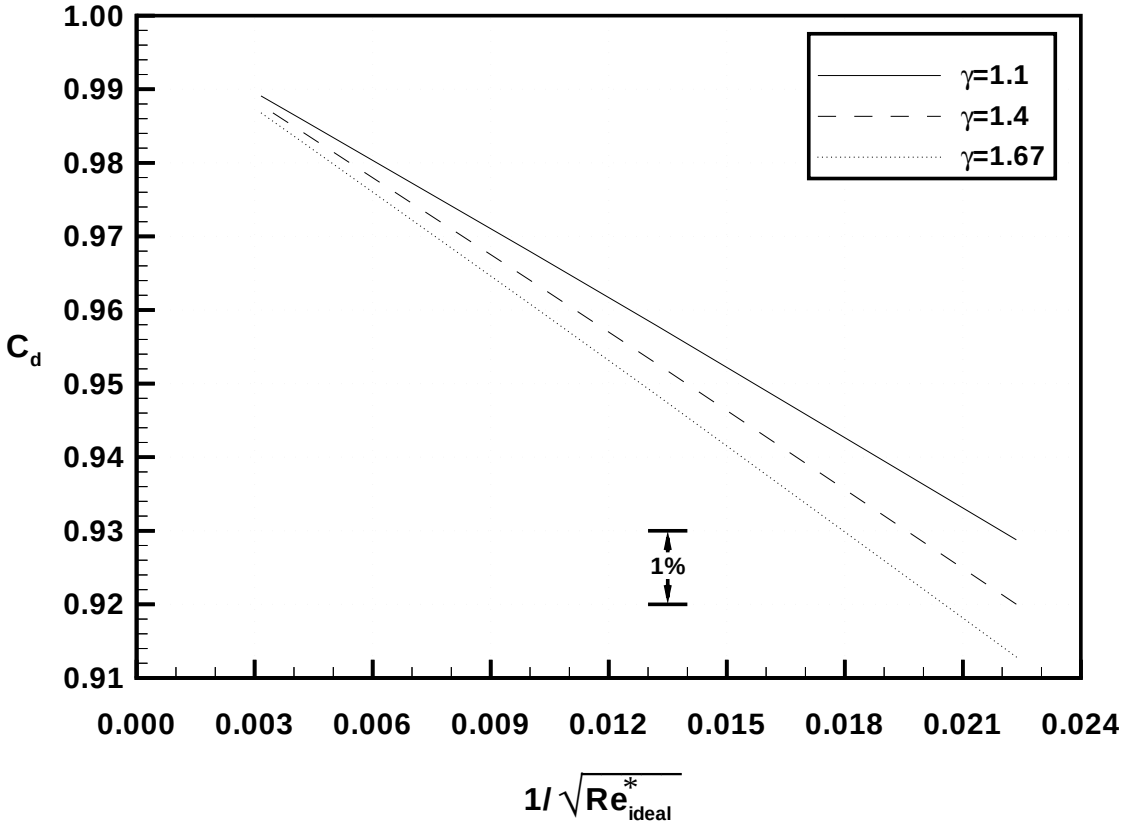

Figure 3.12. Numerically predicted calibration curves for $\gamma = 1.1$, $\gamma = 1.4$, and $\gamma = 1.67$

diminishes the effect of γ on C_d. As shown in Eq. (3.6) the magnitude of viscous dissipation increases as γ increases. Consequently, larger values of γ result in a larger value of the normalized temperature, T/T^*. The larger normalized temperature throughout the boundary layer results in lower normalized densities, ρ/ρ^*, and ultimately lower discharge coefficients.

3.6.4 Effect of viscosity ratio and thermal conductivity ratio

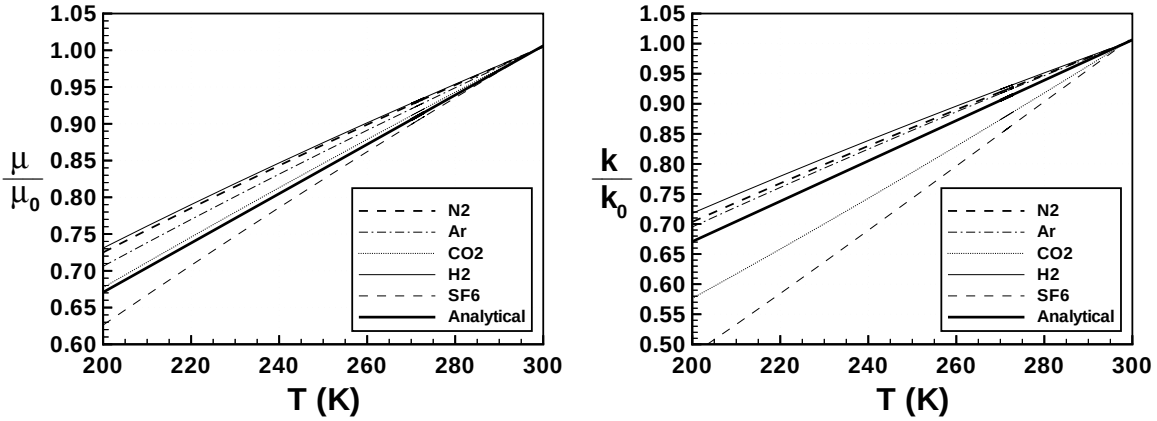

Figure 3.13. Transport properties for various gases as a function of temperature.

As shown in the dimensional analysis of Section 3.1 the discharge coefficient has a functional dependence on the viscosity ratio, μ/μ_0, and the thermal conductivity ratio, k/k_0. Analytical models assume that the transport properties of all gas species have the same linear functional dependence on temperature. That is, μ/μ_0 and k/k_0 maintain the same linear dependence on temperature regardless of gas species. However, while the variation between the analytical and actual values are relatively small, neither the viscosity ratio nor the thermal conductivity ratio exactly follows the analytically assumed temperature distribution. Instead, μ/μ_0 and k/k_0 vary for each gas according to the plots shown in Fig. (3.13). The change in the discharge coefficient as a result of the variation in μ/μ_0 and k/k_0 for different gases is considered in this section.

First, the effect of the viscosity ratio was assessed by systematically varying the value of μ/μ_0 in the CFD simulations. In particular, the numerical simulations compared predicted C_d values resulting from two different values of viscosity ratio, that of N_2 gas, $(\mu/\mu_0)_{N_2}$, and that of SF_6 gas, $(\mu/\mu_0)_{SF_6}$. These gases were selected since the difference in the viscosity ratio between these two gases represents the largest change in the viscosity ratio among the gases considered (see Fig. 3.13). Thus, this comparison should indicate the largest possible effect of the viscosity ratio on C_d.

With the exception of the systematic variation of the viscosity ratio, the baseline fluid properties of N_2 gas were used for these simulations. The results of the simulations showed that the numerically predicted discharge coefficients increased slightly with decreasing values of viscosity ratio. In particular, at a Reynolds number of 2 000 the predicted discharge coefficient increased by 0.043 % when the larger viscosity ratio of N_2 gas was replaced by the lower SF_6 viscosity ratio, $(\mu/\mu_0)_{SF_6}$. At a larger Reynolds number of 100 000, the increase in C_d resulting from the lower μ/μ_0 value was only 0.007 %. Thus, as expected the effect of viscosity diminished at larger Reynolds numbers where the boundary layer is thinner. Even at the lower of the two Reynolds numbers, however, the relatively small difference observed in the C_d predictions due to variation of the viscosity ratio among different gas species supports the use of the linear relationship between viscosity and temperature (see Fig. 3.13) used in analytical works.

The effect of the thermal conductivity ratio was also assessed by using various

functional forms of k/k_0 in the CFD simulations. In particular, the numerical simulations compared the predicted C_d values using the thermal conductivity ratio for N_2 gas versus the values obtained using the thermal conductivity ratio for SF_6 gas (see Fig. 3.13). Again, except for the systematic variation of k/k_0, these simulations were performed using the baseline fluid properties for N_2 gas at the same two Reynolds numbers as the viscosity study, 2 000 and 100 000. The results of the simulations showed that the numerically predicted discharge coefficients decreased with decreasing k/k_0 values. Physically, at lower values of conductivity ratio, heat generated by viscous dissipation is not diffused as far into the free stream so that the thermal boundary layer is warmer, resulting in a slightly lower density, and subsequently lower value of C_d. At a Reynolds number of 2 000 the C_d predictions using k/k_0 for SF_6 gas were only 0.017 % lower than C_d predictions using k/k_0 of N_2 gas. This value decreased to 0.002 % at a Reynolds number of 100 000. Similar to the viscosity results, in both cases the relatively small difference found in C_d predictions due to the variation of thermal conductivity among different gas species supports the linear relationship between k/k_0 and temperature used in analytical works.

3.6.5 Effect of Inlet Piping

In the simulations thus far, we have excluded the piping upstream of the nozzle entrance, considering only the nozzle geometry itself as the computational domain.

While this is computationally more efficient than including the upstream piping section, we investigate the error introduced by using this assumption in this section. Physically, the upstream section dictates the flow angle at the inlet to the nozzle. In the nozzle only computations we arbitrarily set the flow angle at the inlet parallel to the grid lines. The computations with the inlet section included determines the flow angle from the physics of the nozzle inlet interaction.

Four diameters of upstream pipe meshing were added to the nozzle geometry shown previously in Fig. (3.2). The upstream piping section used 75 000 nodes to ensure grid independent solutions. Stagnation boundary conditions were implemented at the upstream piping inlet along with a parallel flow inlet velocity profile. By including the upstream piping geometry the appropriate inlet boundary layer thickness could be calculated at the nozzle inlet. However, when the nozzle upstream was included the discharge coefficient changed by less than 0.023 % versus the calculations performed excluding the upstream geometry. Therefore, neglecting the upstream piping section is a convenient and adequate assumption for C_d calculations.

3.6.6 Effect of Uncertainty in Nozzle Throat Diameter

Using either computational or analytical methods to make high accuracy critical nozzle mass flow predictions requires a sufficiently accurate description of the nozzle geometry. In particular, a highly accurate value of the nozzle throat diameter is required. Any deviation between the actual value of the throat diameter and the

value used in predictive models will introduce additional uncertainty components into the analysis. This section will address how uncertainties in the nozzle throat diameter affect comparisons between quantitative predictions and measured values of the discharge coefficient.

The uncertainty in the nozzle throat diameter affects the discharge coefficient via uncertainties in the theoretical mass flow, $\dot{m}_{ideal}$, as well as the calibration Reynolds number, Re^{*}_{ideal}, both of which depend on diameter. The Reynolds number varies linearly with diameter while the theoretical mass flow varies with the square of diameter. Given that the theoretical mass flow is used as the normalizing parameter in the definition of the discharge coefficient, uncertainties in $\dot{m}_{ideal}$ add additional uncertainty to the experimentally measured C_d values. In particular, experimentally measured C_d values vary inversely with the square of the nozzle diameter (*i.e.*, $C_{d_{exp}} \propto d^{-2}$) so that any uncertainty in the throat diameter results in twice the uncertainty in $C_{d_{exp}}$. Thus, the uncertainty in the normalizing mass flow affects the entire calibration curve, shifting the measured C_d values vertically (upwards or downwards) by the magnitude of the uncertainty. Therefore, the $\pm 1\,\mu$m machining tolerance for the $d = 0.5935\,$mm critical nozzle produces an additional $\mp 0.337\,\%$ uncertainty in the measured C_d values.

The uncertainty in nozzle diameter also affects the experimentally calculated Reynolds number, which in turn affects the predicted C_d values. The effect of this uncertainty on predicted C_d values is a result of satisfying dynamic similarity, whereby the Reynolds

number used in predictive models is set equal to the Reynolds number of the actual flow. However, since the discharge coefficient is relatively insensitive to small changes in the Reynolds number, the uncertainty attributed to this effect is generally quite small. For example, for a critical nozzle flow having a nominal Reynolds number of 2 000 with an uncertainty component of $\pm 0.1685\,\%$ (attributed to the uncertainty in the nozzle diameter), the corresponding uncertainty in predicted discharge coefficient is less than $\pm 0.007\,\%$. Furthermore, this level of uncertainty decreases to even smaller values at larger Reynolds numbers. Thus, for the range of Reynolds numbers considered in this investigation (*i.e.,* 2 000 to 131 000) only the uncertainty resulting from $\dot{m}_{ideal}$ needs to be considered. Hence, the total uncertainty resulting from the $\pm 0.1685\,\%$ uncertainty in the nozzle throat diameter is $\mp 0.337\,\%$

3.6.7 Summary of Parametric Study

Parameter	direction of C_d change	% change in C_d
$(Pr \approx 0.7)$ inc Pr	dec C_d	0.01 – 0.11 %
inc γ	dec C_d	0.2 – 1.5 %
inc μ/μ_0	dec C_d	0.006 – 0.043 %
inc k/k_0	inc C_d	0.002 – 0.017 %
adiabatic wall	overpredict C_d	0 – 0.3 %
upstream piping	———	± 0.0230 %
diam uncertainty $\pm 1685\,\%$	dec or inc C_d	$\mp 0.337\,\%$

Table 3.2. Summary of parameters affecting C_d predictions.

In this section the results of the parametric study are summarized in tabular format. Table (3.2) indicates the direction (*i.e.,* increase or decease) and the percent change in C_d as a result of changes in the following parameters: Prandtl number ($Pr = \mu_0 c_{P_i}/k_0$), viscosity ratio (μ/μ_0), thermal conductivity ratio (k/k_0), and specific heat ratio (γ). The table also shows how C_d is affected by neglecting the piping upstream of the nozzle inlet, by the adiabatic nozzle wall assumption, and by uncertainty in the nozzle throat diameter. The percent change in C_d due to these various effects reflects a Reynolds number range from 2 000 to 100 000. In all cases the smallest percentage C_d change occurs at Reynolds number of 100 000 while the larger percentage C_d change occurs at Reynolds number of 2 000. Thus, the table gives insight as to how C_d is affected by the slight variation in these parameters caused by differing gas species.

Chapter 4

VIBRATIONAL RELAXATION MODELS

Experimental data taken for several gas species (shown previously in Fig. 3.1) shows that traditional calibration curves (*i.e.,* C_d versus Re^*_{ideal} plots) are species dependent. That is, the calibration curve for each gas can vary significantly (*i.e.,* by more than a percent) from that of other gases. While minor differences in C_d values are due to wall heat transfer, Prandtl number effects, and different γ values among gases as shown in Chapter 3, this chapter will demonstrate the rather large effect that vibrational relaxation can have on the discharge coefficient of certain gas species in critical nozzle flows.

First, the two limiting conditions of vibrational non-equilibrium flow are discussed to provide insight on how vibrational relaxation phenomena affect the mass flow. Next, a vibrational non-equilibrium CFD model is validated by direct comparison with the experimental data of Nakao *et al.*[35] for SF_6 and CO_2 gases. The same non-equilibrium model is used to predict C_d values for gases not affected by relaxation effects to demonstrate the model's flexibility of handling a wide variety of gases. As in the equilibrium CFD results these numerical simulations follow the experimental calibration procedure, holding the stagnation temperature fixed ($T_0 = 298.15\,\mathrm{K}$) while varying the stagnation pressure ($0.5\,\mathrm{atm} \leq p_0 \leq 3\,\mathrm{atm}$) to yield the desired

Reynolds number. Lastly, vibrational relaxation effects are confirmed by two independent experiments.

4.1 Limiting Cases of Non-Equilibrium Flow

Vibrational non-equilibrium flow phenomenon involves an inherent coupling between gas dynamic flow processes and molecular energy exchange processes. As a result of this coupling, a rigorous consideration of vibrational non-equilibrium behavior requires computer modeling. However, a qualitative understanding of how non-equilibrium phenomenon affects the discharge coefficient of critical nozzle flows can be obtained by considering the two limiting cases of vibrational non-equilibrium flow, *equilibrium flow* and *frozen flow*.

Mathematically, both of the limiting cases for equilibrium flow and frozen flow are controlled by $\Gamma = \tau_{vib}/\tau_{res}$, the ratio of relaxation time to residence time (refer to Eq. 2.15). Equilibrium flow occurs in the limit as Γ tends toward zero (*i.e.,* $\Gamma \to 0$). In the equilibrium flow limit the gas molecules comprising the fluid element immediately adjust their vibrational energy level to correspond to the surrounding fluid temperature. Mathematically, the left hand side of Eq. (2.15) vanishes (*i.e.,* a singular perturbation problem) so that the vibrational energy equals its equilibrium value.[1]

Frozen flow, on the other hand, occurs in the limit as the ratio of relaxation time

[1] At the nozzle inlet the ϵ_{vib} is in equilibrium so that a perturbation analysis not necessary.

to residence time tends toward infinity (*i.e.,* $\Gamma \to \infty$). In the frozen flow limit the gas molecules comprising the fluid element have no time to adjust their vibrational energy level to the decreasing free stream temperatures. Consequently, the vibrational energy remains *frozen* at its upstream equilibrium value. Mathematically, as Γ tends toward infinity, the right hand side of Eq. (2.15) vanishes (*i.e.,* a regular perturbation problem) so that the spatial derivative of ϵ_{vib} on the left hand side is identically zero, and ϵ_{vib} remains constant (*i.e.,* $\epsilon_{vib} = constant$) throughout the flow field. Moreover, since the flow is initially in equilibrium at the nozzle inlet, the constant value of vibrational energy is equal to the inlet equilibrium value.

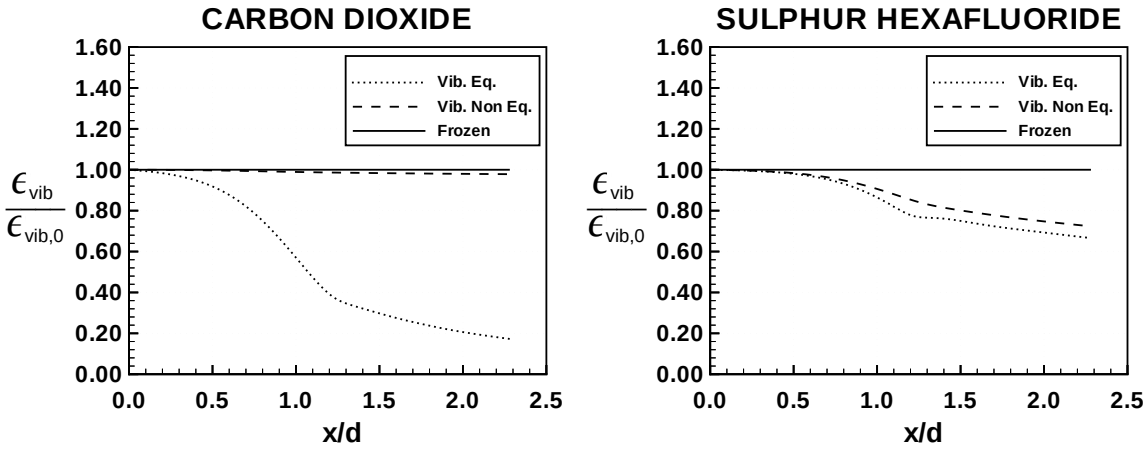

Figure 4.1. Normalized vibrational energy along the nozzle centerline for frozen flow, equilibrium flow and vibrational non-equilibrium flow for CO_2 at $Re^*_{\text{ideal}} = 2\,402$ and SF_6 at $Re^*_{\text{ideal}} = 18\,926.1$.

Figure (4.1) compares numerical computations of the nozzle centerline vibrational energy for frozen flow (——), vibrational equilibrium flow ($\cdots$), and vibrational non-equilibrium flow (- - -) for CO_2 gas at a Reynolds number of 2 402 (left) and for SF_6 gas at a Reynolds number of 18 926.1 (right). The vibrational energy for both

CO_2 and SF_6 has been normalized by the vibrational energy at the nozzle inlet so that the normalized vibrational energy, $\epsilon_{vib}/\epsilon_{vib,0}$, is unity at the nozzle entrance for all three cases. For the frozen flow case the normalized vibrational energy remained unity for the entire distance along the nozzle centerline for both gases. Physically, the rate of molecular energy exchange between vibrational modes and translational modes is infinitely slow relative to the rate of flow processes. Thus, the energy in the vibrational modes at the nozzle inlet remains trapped in these modes.

In the case of equilibrium flow the centerline vibrational energy decreases for both CO_2 and SF_6 as a result of the decrease in the centerline temperature. The decrease in the vibrational energy is more substantial for CO_2 gas, however, given that it has a larger γ and therefore expands to lower temperatures as the gas accelerates through the nozzle.

The vibrational energy for the non-equilibrium case lies between the equilibrium flow limit and the frozen flow limit for both gases. This non-equilibrium situation will exist whenever the value for $\Gamma = \tau_{vib}/\tau_{res}$ is finite but non-zero. Since CO_2 gas relaxes more than an order of magnitude slower than SF_6 gas, it lies closer to its frozen flow limit than does SF_6 in Fig (4.1). Note, however, that the vibrational energy for both gases would be shifted closer to the equilibrium flow limit if Γ is decreased. The value of Γ can be decreased by either increasing the stagnation pressure or by increasing the length over which the gas is accelerated. Increasing the stagnation pressure decreases the relaxation time, τ_{vib}, by increasing the number of molecular collisions and,

subsequently, increasing the rate of molecular energy exchange. On the other hand, increasing the nozzle length increases the residence time, τ_{res}, allowing more time for the gas to achieve equilibrium. Implementing either one of these conditions results in a decrease in Γ.

A qualitative assessment of the effect of non-equilibrium flow processes on mass flow can be determined by evaluating the mass flow at both of the limiting conditions. At either of the two limiting conditions the gas dynamic equations can be solved uncoupled from the vibrational rate equation. Therefore, a simple way to understand how the mass flow rate is affected is by considering how γ changes between the two limiting cases for non-equilibrium flow. An expression for the specific heat ratio that is valid for both equilibrium and frozen flow of a perfect gas is given by

$$\gamma = 1 + \frac{R_{gas}}{c_V}. \tag{4.1}$$

where R_{gas} is the gas constant and c_V is the constant volume specific heat. To evaluate the equilibrium value of the specific heat ratio, $\gamma = \gamma^{eq}$, the constant volume equilibrium specific heat, c_V^{eq}, is used in Eq. (4.1). Likewise, to evaluate the frozen flow value for the specific heat ratio, $\gamma = \gamma^{fr}$, the constant volume frozen flow specific heat, c_V^{fr}, is used in Eq. (4.1).

For the equilibrium flow of a rotationally fully excited perfect gas the constant

volume equilibrium specific heat is given by [53]

$$c_V^{eq} = \frac{R_{gas}}{2}\left(3 + N_{rot} + \sum_{k=1}^{N} \frac{g_k \ \exp(\theta_k/T) \ (\theta_k/T)^2}{[\exp(\theta_k/T) - 1]^2}\right) \tag{4.2}$$

where the second term in the brackets, N_{rot}, is the number of active rotational degrees of freedom, and the third term in the brackets represents the contribution of vibrational energy modes to the constant volume specific heat. Note that $N_{rot} = 2$ for linear molecules and $N_{rot} = 3$ for non-linear molecules. The characteristic temperature of vibration for the various molecular vibrational modes, θ_k, and the degeneracy for each vibrational mode, g_k, are both given for CO_2 and SF_6 previously in Table (2.2) and Table (2.3). The electronic contribution to the equilibrium specific heat is negligible over the temperature range of interest and has been omitted from Eq. (4.2).

For the frozen flow case the vibrational energy remains constant so that the vibrational contribution to c_V^{fr} is identically zero and the constant volume specific heat is given by [53]

$$c_V^{fr} = \frac{R_{gas}}{2}\left(3 + N_{rot}\right). \tag{4.3}$$

The absence of the vibrational terms in c_V^{fr} ensures that the constant volume frozen specific heat is always less than the equilibrium specific heat (*i.e.*, $c_V^{fr} < c_V^{eq}$). The inverse relationship between the specific heat ratio and the constant volume specific heat given in Eq. (4.1) requires that γ increases for smaller values of c_V so that

$\gamma^{fr} > \gamma^{eq}$. With all other conditions fixed (*i.e.,* stagnation conditions, nozzle geometry, and the gas constant) the larger values of γ occurring in the frozen flow limit result in an increase in the mass flow through the nozzle (*i.e.,* $\dot{m}_{fr} > \dot{m}_{eq}$).

To estimate the magnitude of the increase in mass flow between the two limiting cases the one-dimensional inviscid mass flow equation for a choked nozzle flow given previously in Eq. (1.2) is used. The mass flow is evaluated at the equilibrium specific heat ratio, γ^{eq}, and at the frozen specific heat ratio, γ^{fr}. As an example, the increase in mass flow between equilibrium and frozen flow limits is estimated for CO_2 gas flow. For definiteness the CO_2 gas is assumed to be rotationally fully excited with $N_{rot} = 2$ at a reference temperature of 298.15 K so that $\gamma^{eq} = 1.30$ (nominally) and $\gamma^{fr} = 1.40$. The increase in mass flow between the equilibrium flow and the frozen flow is estimated to be 2.9 %. This magnitude of mass flow increase is of the right magnitude and in the right direction to explain why the equilibrium CFD model underpredicted the experimental data by more than two percent in Fig. (3.4) .

The amount that the mass flow increases from the equilibrium flow limit to the frozen flow limit represents the maximum possible change in mass flow. In the intermediate situation (*i.e.,* vibrational non-equilibrium flow) the mass flow achieves some intermediate value between the two limiting mass flows. In the next section the vibrational non-equilibrium CFD model will be used to predict C_d values for CO_2 and SF_6 gases.

4.2 Vibrational Relaxation Results for CO_2 and SF_6 Gases

The results of the equilibrium CFD model in Chapter 3 underpredicted the experimental calibration curves for both CO_2 and SF_6 gases. Furthermore, the experimental calibration curves of these two gases exhibited unique calibration behavior relative to the experimental calibration curves of other seemingly similar gases (see Fig. 3.1). In the previous section, the two limiting cases of vibrational non-equilibrium flow were used to demonstrate that vibrational relaxation effects are the likely explanation for the observed underprediction in mass flow exhibited by the equilibrium CFD model for CO_2 gas. In this section we compare the results of the vibrational non-equilibrium CFD model to experimental data, focusing on the marked improvement in C_d predicitions for those gases expected to be affected by vibrational relaxation phenomenon.

The calibration curves shown in Fig. (4.2) compare the C_d predictions of the various predictive models to experimental data for H_2, N_2, CO_2, and SF_6 gases. Each of the three mathematical models shown in Fig. (4.2) offers a different level of complexity. The composite boundary layer/inviscid core model of Ishibashi and Takamoto represented by the dashed line (– – –) uses a constant value of specific heat ratio (*i.e.*, $\gamma = constant$) to permit a closed form algebraic expression for the discharge coefficient. A closely related but slightly more refined analysis (—×—) uses a version

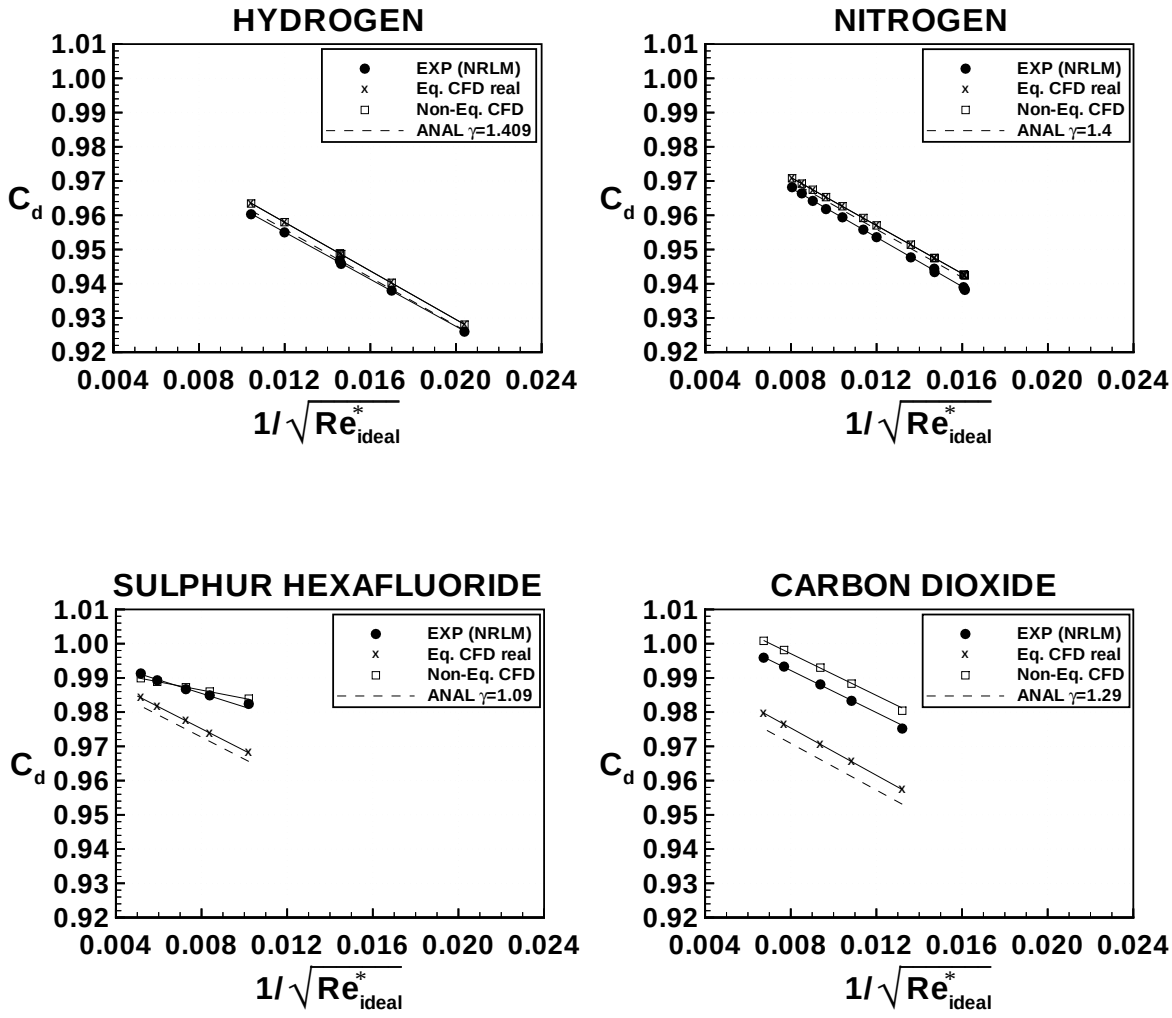

Figure 4.2. Comparison between mathematical models and experimental data for various gases flowing through an ISO critical nozzle ($d = 0.5395$ mm and $\theta = 3$ degrees): NRLM analytical model with $\gamma = constant$ (– – –), equilibrium CFD model with real gas effects (—×—), non-equilibrium CFD model (—□—), and experimental data (—●—).

of the equilibrium CFD model that accounts for real gas behavior to predict C_d behavior. The results of both of these models have been shown previously in Chapter 3 (see Fig. 3.4), but are repeated here to illustrate the marked level of improvement rendered by the vibrational non-equilibrium CFD model (—□—) for CO_2 and SF_6 gases. The three predictive models are compared against the experimental data labeled by the •'s where the size of the symbol is indicative of the 0.2% experimental uncertainty.

The C_d predictions for all three models are found to be in good qualitative agreement with the experimental data over the entire range of Re^*_{ideal} for all of the gases considered. Of particular interest, however, is the level of agreement between the results of the vibrational non-equilibrium model and the experimental data for the various gases. As expected for the diatomic gases H_2 and N_2, no improvement was observed when using the vibrational non-equilibrium CFD model instead of the equilibrium CFD model. At room temperature the negligible level of vibrational energy for these diatomic gases yields almost identical C_d predictions for the equilibrium and non-equilibrium models as observed in Fig. (4.2). On the other hand, for CO_2 and SF_6 gases the vibrational non-equilibrium CFD model yielded an almost two percent improvement over either the analytical or equilibrium CFD results. Thus, the vibrational non-equilibrium model provides a general model with which the discharge coefficient is predicted to better than one half of one percent for all of the gases considered.

The close agreement between the vibrational non-equilibrium model and the experimental data lends support to the validity of the model. In fact, the slight C_d overprediction for CO_2, and over most of the Reynolds number range for SF_6 in Fig. (4.2) is consistent with overpredictions observed when the analytical model [34] (or equilibrium flow model [63]) is used to predict C_d behavior for Ar, H_2, and N_2 – gases not affected by vibrational relaxation. Therefore, it is plausible that the slight C_d overprediction is caused by physical mechanisms absent in all three models. For example, the sensitivity study in Chapter 3 determined that the adiabatic wall boundary condition used in the computations results in an estimated overprediction of C_d ranging from 0.0% to 0.3% depending on Reynolds number and gas species. This could offer a partial explanation for the slight C_d overpredictions. The remaining discrepancy might be attributed to the $\pm 0.1685\,\%$ uncertainty in the nozzle throat diameter. This amount of uncertainty in the nozzle throat diameter results in a $\mp 0.337\,\%$ additional uncertainty in the measured C_d values (see Section 3.6.6), a margin large enough to account for the overprediction observed for all predicted C_d values, and to bring the C_d values predicted with the vibrational non-equilibrium model within the limits of experimental uncertainty for all the gases considered.

Non-equilibrium flow processes are responsible for the nearly 2 % increase in C_d predictions between the equilibrium flow model (—×—) and the non-equilibrium flow model (—□—) for CO_2 gas and the more than 1 % increase for SF_6 gas shown previously in Fig. (4.2). Physically, vibrational relaxation effects induce increased mass flows,

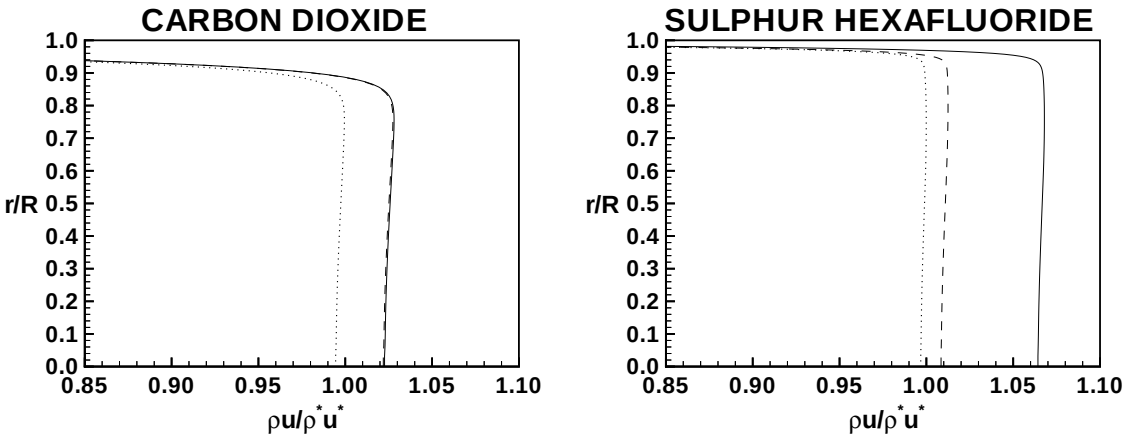

Figure 4.3. Comparison of the normalized throat mass flux profile for the equilibrium CFD model (·····), the non-equilibrium CFD (– – –) model, and the frozen flow CFD model (——) for CO_2 at $Re_{ideal} = 2402.2$ (left) and SF_6 at $Re_{ideal} = 18926.1$ (right).

which in turn, lead to increased C_d predictions. The reason for the increase in mass flow is two fold: First, flow acceleration processes are augmented, resulting in a higher free stream throat velocity. Second, the flow expansion through the critical nozzle is diminished leading to higher free stream throat densities. The combined effect is illustrated in Fig. (4.3), which compares the non-equilibrium radial mass flux profile (– – –) to the corresponding equilibrium profile (·····) and frozen flow profile (——) at the nozzle throat for CO_2 gas at $Re^*_{ideal} = 2\,402$ (left) and for SF_6 gas at $Re^*_{ideal} = 18\,926.1$ (right). In the figure, ρu has been conveniently normalized by $\rho^* u^*$ (*i.e.,* the predicted mass flux for *ideal* flow conditions) so that an area weighted integration across the throat cross section yields the discharge coefficient. Therefore, the nearly 2 % increase in the free stream mass flux for CO_2, and more than 1 % increase for SF_6 between the equilibrium CFD (·····) and the non-equilibrium CFD results (– – –) observed in Fig. (4.3) directly corresponds to the predicted increase

in C_d values for CO_2 and SF_6 gases shown earlier in Fig. (4.2). Lastly, notice as previously discussed in section 4.1, the non-equilibrium mass flow lies between the equilibrium and non-equilibrium flow limits.

4.3 Experimental Validation of Vibrational Relaxation Model

There has been a significant amount of research [64], [65] done to support applications where vibrational non-equilibrium effects are known to be important, such as flows in hypersonic wind tunnels, chemical lasers, and high temperature gas dynamics. However, the effect that this mechanism has on the discharge coefficient of critical nozzles has not been previously investigated, and prior to this investigation vibrational relaxation effects were not considered to affect the discharge coefficient of critical nozzle flows. Therefore, as a confirmation of the numerical results, two experiments were designed with the intent of verifying the vibrational relaxation explanation proposed for CO_2 critical nozzle flows. Both experiments set out to ascertain the effects that vibrational relaxation has on C_d by controlling $\Gamma = \tau_{vib}/\tau_{res}$ – the primary parameter affecting vibrational relaxation phenomenon. The first experiment, conducted at NRLM, varied Γ by using various nozzle sizes and by adjusting the level of stagnation pressure. In this experiment the measured C_d's were compared to those predicted by the vibrational non-equilibrium CFD model over a wide range of Reynolds numbers. The second experiment, conducted at NIST, reduced Γ by adding small concentrations of water vapor to the CO_2 gas.

For a given gas composition the magnitude of Γ determines the extent of the vibrational non-equilibrium effects in the flow field. For values of Γ significantly less than unity (*i.e.*, $\tau_{vib} << \tau_{res}$) fluid particles equilibrate quickly with the changing thermodynamic surroundings that they encounter while moving along their trajectory. That is, the time that it takes a fluid particle to traverse a certain distance along its trajectory is large relative to the time necessary for molecular collisions to bring the fluid particle into vibrational equilibrium. At larger values of Γ, however, relaxation effects become more important. Physically, fluid particles move along their trajectory passing through their surrounding thermodynamic environment in time periods that are on the same order of magnitude (or shorter) than the time necessary for molecular collisions to bring the level of vibrational energy into equilibrium. Based upon the important role Γ plays in characterizing non-equilibrium flow behavior, both experiments systematically vary this parameter to assess vibrational relaxation effects.

4.3.1 First Experiment; Increasing Nozzle Size

The first experiment utilized a gravimetric calibration facility to measure the discharge coefficient of four different size ISO critical nozzles flowing CO_2 gas [35]. The throat diameters of the four nozzles were 0.2950 mm, 0.5935 mm, 1.1845 mm, and 2.3598 mm respectively. For each nozzle, the stagnation pressure was varied from 0.5 atm to 3 atm while the stagnation temperature remained fixed at 298.15 K. Although there is some overlap of Reynolds number for the different nozzle sizes, in general, the range of Reynolds number differed for each nozzle due to the different

throat diameter sizes. The Reynolds number ranged from a low of 2 500 corresponding to the smallest nozzle size to a high of 131 000 corresponding to the largest nozzle size.

The eight fold increase in throat diameter sizes as well as the six fold increase in stagnation pressure were used to vary $\Gamma = \tau_{vib}/\tau_{res}$. For the ISO toroidal throat nozzles used in this experiment (see Fig. 1.2 shown previously in Section 1.1 of Chapter 1), the larger throat diameters corresponded to longer axial distances between the nozzle inlet and the nozzle throat; therefore, the distance fluid particles had to travel to reach sonic conditions as well as the time necessary to traverse this distance (*i.e.,* flow residence time) increased for larger nozzle sizes. By varying the nozzle sizes the flow residence time can be augmented by a factor of eight, which in turn, leads to an eight fold reduction in Γ. Similarly, the six fold increase in stagnation pressure (at a fixed stagnation temperature of 298.15 K) reduces the vibrational relaxation time (see Eq. 2.13), and consequently Γ by six fold. By varying nozzle size and stagnation pressure together, Γ can be changed by a factor of forty eight, almost two orders of magnitude.

Given that the Reynolds number is proportional to both p_0 and d, varying these parameters to control $\Gamma = \tau_{vib}/\tau_{res}$ result in changes to the Reynolds number as well. In particular, for a fixed gas composition at a constant stagnation temperature

($T_0 = 298.15\,\mathrm{K}$), increasing either p_0 or d[2] decreases Γ, but increases the Reynolds number. As a result, relaxation effects diminish at larger Reynolds numbers where Γ is lower. If non-equilibrium effects are responsible for the unusual calibration characteristics observed for CO_2, a drop off in C_d should be observed in higher Reynolds number calibration data. Specifically, the discharge coefficient should deviate from the linear relationship between C_d and $1/\sqrt{Re^*_{ideal}}$ observed in laminar flow for gases unaffected by vibrational relaxation effects. Furthermore, since the effect of vibrational relaxation is to increase the mass flow through the nozzle, larger than unity C_d's are possible at finite Reynolds numbers. This is in spite of the fact that the discharge coefficient is normalized by $\dot{m}_{ideal}$, the mass flow based on an inviscid analysis.

For gases unaffected by relaxation phenomenon (*e.g.,* air, N_2, Ar, He, and H_2), C_d increases linearly with decreasing $1/\sqrt{Re^*_{ideal}}$ over the entire laminar range of Reynolds numbers (*i.e.,* $Re^*_{ideal} < 10^6$). Experimental documentation of this linear behavior for air has been demonstrated by Ishibashi and Takamoto [34]. These authors fit calibration data to the expression, $C_d = \alpha + \beta/\sqrt{Re^*_{ideal}}$ (where α and β are coefficients determined by the fit), and the scatter along the curve was less than $\pm 0.04\%$ over a Reynolds number range from 10 000 to 250 000. Additional experimental documentation of this linear trend for other gases (*e.g.,* N_2, Ar, He, and H_2) can be found in the work of Arnberg *et al.* [37] This linear behavior is also in agreement with theoretical C_d predictions when either the equilibrium CFD model or the NRLM analytical

[2]ISO nozzles are geometrically scaled so that larger throat diameters correspond to longer distances from the nozzle inlet to the nozzle throat.

model (refer to Eq. 1.11) is used to predict the discharge coefficient for CO_2 flow.

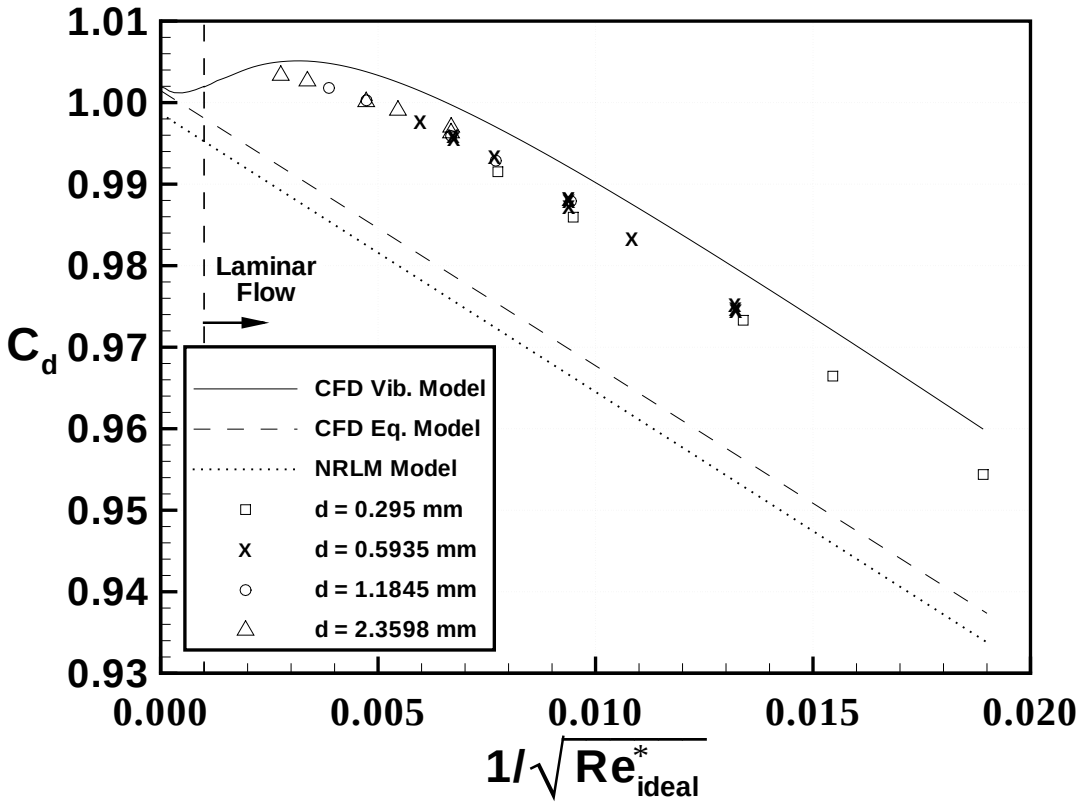

Figure 4.4. Comparison of experimental CO_2 calibration data for various toroidal throat nozzle sizes with predictive models.

Figure 4.4 compares the experimental data to the three predictive models that were discussed in the previous section. The smallest nozzle size ($d = 0.2950\,\text{mm}$) corresponds to the lowest Reynolds number range and is denoted by the □'s, Likewise, the intermediate nozzle sizes $d = 0.5935\,\text{mm}$ and $d = 1.1845\,\text{mm}$ are denoted by the ×'s and ○'s respectively, and the largest nozzle size ($d = 2.3598\,\text{mm}$) denoted by the △'s corresponds to the highest values of Reynolds number. The size of the symbols

is scaled to the 0.2 % experimental uncertainty. The results yielded by the three predictive models are depicted by lines to distinguish them from experimental data. A solid line (——) is used to depict vibrational non-equilibrium CFD results, a dashed line (– – –) depicts the equilibrium CFD results, and the dotted line (· · ·) is used to depict the NRLM analytical model.

Behavior consistent with vibrational relaxation effects can be observed in the CO_2 calibration data (□, ×, ○, and △) in Fig. (4.4). In particular, at the larger Reynolds numbers (*i.e.,* lower $1/\sqrt{Re^*_{ideal}}$) Γ decreases so that the magnitude of the slope of the calibration data begins to decrease and the linear characterization of C_d with $1/\sqrt{Re^*_{ideal}}$ no longer holds. The measured C_d's are less than would be predicted by extrapolating the linear relationship (between C_d and $1/\sqrt{Re^*_{ideal}}$) observed at lower Reynolds numbers.

At higher values of Γ, corresponding to lower Reynolds numbers ($2\,500 \leq Re^*_{ideal} \leq 250\,000$), vibrational relaxation effects are insensitive to changes in Γ – a phenomenon expected of the exponential relaxation processes. As Γ decreases, however, relaxation effects begin to transition toward equilibrium flow behavior, tending to decrease C_d. Given that decreases in Γ correspond to increases in Reynolds numbers, the boundary layer thins, tending to increase C_d. The two competing mechanisms result in a non-linear calibration curve at large Reynolds numbers. In addition to the non-linear calibration behavior, vibrational relaxation effects are also largely responsible for the greater than unity C_d's observed in the calibration data. The larger than unity

experimental C_d values occur because the increase in mass flow due to vibrational non-equilibrium effects is not accounted for in the normalizing theoretical mass flow used in the denominator of the discharge coefficient definition.

Comparison between the calibration data ($\square$, $\times$, $\circ$, and $\triangle$) and the vibrational non-equilibrium CFD model (——) in Fig (4.4) shows that they are in good agreement. The vibrational non-equilibrium CFD model captures both the linear behavior exhibited at the lower Reynolds numbers as well as the non-linear C_d behavior observed at larger Reynolds numbers. The CFD relaxation model overpredicted the calibration data, but by only 0.4 % at the lower Reynolds numbers with better agreement at higher Reynolds numbers. Although the experimental facilities were limited to a maximum Reynolds number of 131 000, the CFD model was extended beyond this value in order to assess the implications of relaxation phenomenon at still higher Reynolds numbers. For simplicity these computations assume that the boundary layer remains laminar even above the transitional Reynolds number of 10^6 (indicated by the vertical dashed line in Fig. 4.4). Strictly speaking, above this value the predictions lose their validity, but they are still useful for developing an understanding of relaxation effects isolated from other mechanisms (*e.g.,* real gas effects and transition to turbulence).

Based on the vibrational non-equilibrium CFD predictions in Fig. (4.4), relaxation phenomenon can be classified into three regimes depending on Γ. For high values of Γ (*i.e.,* lower Reynolds numbers) the discharge coefficient of the nearly frozen flow increases linearly with decreasing $1/\sqrt{Re^*_{ideal}}$, and is approximately 2 % larger

than would be predicted by equilibrium flow models. As Γ decreases, corresponding to larger Reynolds numbers, the flow begins to transition toward equilibrium flow causing a deviation from the linear relationship between C_d and $1/\sqrt{Re^*_{ideal}}$. As a result of this transition, C_d decreases with increasing Reynolds number. At still lower values of Γ relaxation effects become negligible and C_d predictions return to the equilibrium flow behavior, regaining a linear characterization with $1/\sqrt{Re^*_{ideal}}$.

4.3.2 Second Experiment; Mixture of CO_2 and Water Vapor

A second experiment using mixtures of carbon dioxide and water vapor was devised to obtain further evidence that vibrational equilibrium effects are responsible for the observed discharge coefficient phenomenon. It is documented in the literature of vibrational non-equilibrium that small concentrations of water vapor act as a catalyst to CO_2 vibrational relaxation and lead to dramatically smaller values of the vibrational relaxation time, τ_{vib}, and consequently reduced values of Γ [51], [66]. By introducing concentrations of 0.5 % (or less) water vapor on a molar basis into CO_2, significant reductions in the discharge coefficient relative to those for pure CO_2 should be observed.

For the experiment, a 0.3 mm throat diameter critical venturi was calibrated with pure CO_2 and with CO_2 diluted by varying concentrations of water vapor. The mass flow was measured with a pressure-volume-temperature-time primary flow standard at NIST with an uncertainty of 0.10 % [12]. The CO_2 and water vapor mixture was

generated by first adding water vapor to an evacuated tank until the desired partial pressure of water was attained. Then CO_2 was added to the tank until the desired total pressure was attained. The entire experimental apparatus was kept in a room heated to 300 K to prevent condensation of water vapor during the course of the experiment. (The dew point temperature of the 0.5 % water vapor mixture is 286.4 K at the largest operating stagnation pressure of 3 atm). In addition, before and after usage of the gas mixture, an optical hygrometer was used to measure the dew point temperature of the mixture and a total pressure measurement was made at the hygrometer. Using these measurement techniques, the uncertainty of the water vapor concentration is 0.05 % or less.

The results of the CO_2 and water vapor mixture experiment are shown in Fig. (4.5). It can be seen that the addition of 0.5 % water vapor to the CO_2 gas reduced the discharge coefficient by about 1.3 %, moving the discharge curve in the direction anticipated by the vibrational relaxation explanation. The addition of water reduces the vibrational relaxation time of the gas mixture which in turn reduces the mass flux through the venturi throat as explained previously.

In calculating the discharge coefficients in Fig. (4.5), the normalizing theoretical mass flow includes a version of the critical flow function, C_s, based on the methods described by Aschenbrenner [67], (*i.e.,* weighting the pure gas specific heats by their respective mole fractions to obtain the mixture specific heat ratio). Also the gas constant for the mixture was calculated by weighting the pure gas component molecular

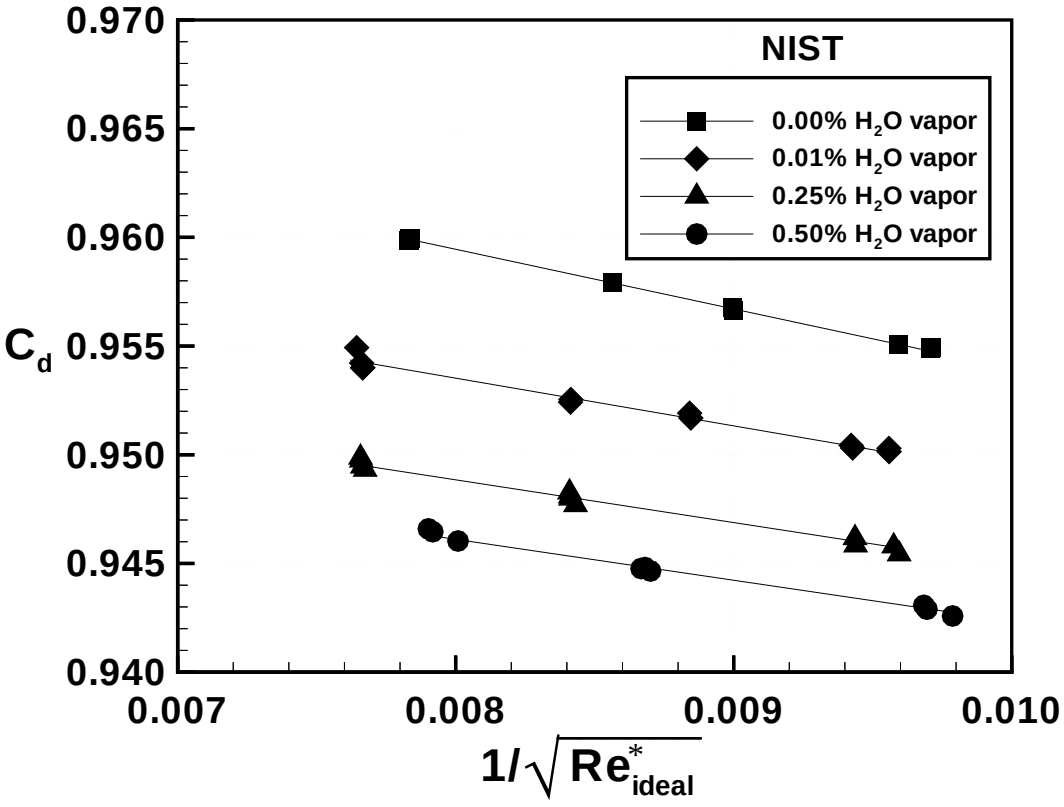

Figure 4.5. NIST experimental data showing the effect of small concentrations of water vapor on the discharge coefficient of CO_2.

weights by the respective mole fractions. In this way, the known major effects on the discharge coefficient have been taken into account in the normalizing quantity of the discharge coefficient and remaining changes in the discharge coefficient can be attributed largely to vibrational relaxation effects.

4.4 Functionality of the C_d for Vibrational Non-Equilibrium Flows

In section 3.1 of Chapter 3 we derived Eq. (3.11) which gave the important dimensionless parameters charactering the discharge coefficient for equilibrium nozzle flows.

For vibrationally non-equilibrium flows, this equilibrium characterization must be extended to include relaxation effects. The vibrational non-equilibrium CFD analysis from Section 4.2 as well as the experimental results from Section 4.3 both demonstrated the importance of the dimensionless parameter $\Gamma = \tau_{vib}/\tau_{res}$ in vibrational non-equilibrium flows. The importance of this parameter was also demonstrated in Section 4.1 where the two limiting cases of vibrational non-equilibrium flow were discussed. The magnitude of Γ determines whether vibrational non-equilibrium effects are present in the flow field. For $\Gamma \to 0$ the flow approaches the equilibrium flow limit. Non-equilibrium effects manifest at positive, finite values of Γ, diverging further away from equilibrium flow as Γ increases, and converging toward the frozen flow limit as $\Gamma \to \infty$.

To fully characterize the effect that vibrational relaxation has on gas dynamic processes, another parameter in addition to Γ is necessary. As previously discussed in Section 2.4.1, vibrational relaxation phenomena (*i.e.,* $\Gamma > 0$) only affects gas dynamic flow processes if the vibrational energy levels of the gas are sufficiently populated. This fact was also demonstrated in Fig. (4.2) where relaxation phenomena had no observable effect on the predicted C_d of the vibrationally unexcited H_2 and N_2 molecules, in spite of the large Γ values of these gases. Therefore, the ratio of vibrational energy to the overall internal energy, ϵ_{vib}/ϵ, also plays a major role in determining how vibrational non-equilibrium phenomena affect C_d predictions. As a result, the following equation gives the full functionality of the discharge coefficient including vibrational

non-equilibrium effects

$$C_d = f_3(Re^*_{ideal}, \gamma, Pr, \frac{T_{wall}}{T^*}, \hat{\mu}, \hat{k}, \Gamma, \frac{\epsilon_{vib}}{\epsilon}, geometry). \tag{4.4}$$

Chapter 5

CONCLUSIONS

The objective of this research was to assess the ability of CFD algorithms to predict the discharge coefficients of various gas species flowing through small throat diameter critical nozzles (*i.e.,* 0.2950 mm, 0.5935 mm, 1.1845 mm, and 2.3598 mm). Five gases were considered including Ar, H_2, N_2, SF_6, and CO_2. For this investigation the Reynolds number ranged from 2 000 to 131 000 so that according to experimental evidence [37] the flow remained laminar within the nozzle. The accuracy of these CFD simulations was determined by direct comparison with experimental data. The following is a summary of the findings of this investigation as well as some conclusions drawn from this study.

A closed-form analytical model [35] was shown to adequately predict the discharge coefficient of monatomic and diatomic gases to within one half of one percent, but had difficulty accurately predicting the discharge coefficient for some polyatomic gases to the same level of accuracy. In particular, the analytical model underpredicted the discharge coefficient of CO_2 gas by more than two percent and of SF_6 gas by almost two percent. Moreover, the performance of the analytical model exhibited a molecular bias or gas species effect, whereby the analytical C_d values overpredicted the calibration data for monatomic and diatomic gases, and underpredicted the calibration data

for polyatomic gases – some by a fraction of a percent and others by a substantially larger amount (*e.g.,* CO_2 and SF_6).

A gas species effect was also noted in the calibration data. Calibration data of various gas species exhibited as much as a 3 % difference in the measured C_d values over the range of Reynolds numbers considered. The observed species effect resulted from unique calibration characteristics exhibited by CO_2 and SF_6 gases. The measured C_d values of these two gases were unusually large relative to the measured C_d values of the other gases. In fact, the measured C_d values for CO_2 gas were even shown to exceed unity at the larger Reynolds numbers, a phenomenon totally unexpected based on the existing analytical models.

In an attempt to assess the reasons for the peculiar calibration characteristics of CO_2 and SF_6 gases, and possibly improve predictive capabilities, the critical nozzle flow field was modeled numerically by solving the full Navier-Stokes equations. Initial computations were based on an equilibrium thermodynamic model with a constant specific heat. This numerical approach had the advantage of avoiding many of the assumptions used in analytical models; however, the equilibrium CFD model showed no significant improvement over the existing analytic methods, and consequently, the inability to accurately model certain gases remained. Real gas effects were implemented into the equilibrium CFD analysis in an attempt to improve the model, but this modification resulted in only slightly better predictive capabilities that fell well short of explaining the unique calibration characteristics for CO_2 and SF_6 gases.

The peculiar C_d characteristics exhibited by CO_2 and SF_6 gases were explained by thermodynamic non-equilibrium effects resulting from vibrational relaxation, a mechanism not previously accounted for in predictive models. In any critical nozzle flow meter the flow accelerates from nearly stagnant conditions at the nozzle upstream to sonic conditions at the nozzle throat. For the geometrically small critical nozzles considered in this in this investigation, this acceleration process occurs over very short distances (*i.e.,* less than 1 mm). As a result, certain gases do not achieve equilibrated thermodynamic conditions during the rapid acceleration process. In particular, polyatomic gases that relax slowly relative to flow acceleration processes and that have sufficiently populated vibrational energy levels (*e.g.,* CO_2 and SF_6) are affected by vibrational relaxation effects. On the other hand, gases that are unaffected by vibrational relaxation processes include rapidly relaxing polyatomic gases, slowly relaxing polyatomic gases that are vibrationally unexcited, diatomic gases near room temperature (*i.e.,* vibrational energy levels are insufficiently populated), and monatomic gases.

For gases unaffected by vibrational relaxation phenomena, the existing analytical techniques agree with experimental data to within a half of one percent. However, analytical models necessarily make numerous simplifying assumptions. To quantify how these assumptions affect C_d predictions, a sensitivity analysis was performed using the equilibrium CFD model. The parametric study investigated the effect of various parameters including the Re^*_{ideal}, γ, Pr, and the wall thermal boundary condition.

For an adiabatic nozzle wall it was determined that the slight variation of Pr among different gas species should have no more than a 0.02 % effect on C_d. The assumption of $Pr = 1.0$ used in analytical models causes a slightly larger error in C_d predictions, ranging from 0.0 %– 0.06 % depending on Reynolds number. The discharge coefficient was most sensitive to the wall thermal boundary condition, especially at the lower Reynolds numbers and larger γ values. For example, the predicted discharge coefficient for Ar gas was shown to decrease by as much as 0.28 % at $Re^*_{\text{ideal}} = 3\,903$, indicating that wall heat transfer effects could play an important role in characterizing the discharge coefficient in low Reynolds number flows.

For gases such as CO_2 and SF_6, vibrational relaxation phenomena are expected to play a role in gas dynamic processes. Therefore, a vibrational non-equilibrium CFD model was implemented to make C_d predictions for CO_2 gas flow over a Reynolds number range from 2 000 to 131 000, and for SF_6 gas flow over a Reynolds number range from 10 000 to 63 000. The vibrational non-equilibrium CFD analysis reduced the error in C_d predictions for both gases by a factor of five over previous models. Although the non-equilibrium CFD results slightly overpredicted the experimental data, this trend was consistent with overpredictions found when using either the analytical model or the equilibrium CFD model to predict C_d values for gases unaffected by vibrational relaxation. For CO_2 and SF_6 gases the vibrational relaxation CFD model agreed to better than 0.4 % with calibration data. Furthermore, since the vibrational non-equilibrium model reduces to the equilibrium model under the appropriate flow

conditions, the vibrational relaxation model was able to predict C_d values to better than 0.4 % for all gases considered over the full range of Reynolds numbers.

The effect of Vibrational relaxation phenomena is to increase the mass flow through a critical nozzle, which in turn increases the discharge coefficient. The increase in mass flow is a result of increased sound speeds and increased gas densities in the non-equilibrium flow. The vibrational non-equilibrium CFD analysis indicated a mass flow increase of more than a two percent for CO_2 gas and slightly less than two percent for SF_6 gas. Therefore, vibrational relaxation mechanism explained the unusually large measured C_d values for both of these gases. Furthermore, since this mechanism is not accounted for in the denominator of the discharge coefficient (*i.e.,* the theoretical mass flow), C_d values exceeding unity are possible.

Two independent experiments were performed using CO_2 gas to confirm the vibrational non-equilibrium hypothesis. Both experiments demonstrated the significance of Γ, the ratio of vibrational relaxation time to flow residence time. The first experiment calibrated progressively larger nozzle sizes to increase the flow residence time and subsequently lower Γ. This experiment verified an anticipated drop off in C_d at low values of Γ. This behavior was in agreement with the vibrational non-equilibrium explanation and it was also predicted by the vibrational non-equilibrium CFD model. The second experiment, which reduced vibrational relaxation effects by diluting CO_2 with small concentrations of water vapor also confirmed an expected decrease in C_d.

Existing analytic models characterize the discharge coefficient as a function of γ and Re^*_{ideal}. Additional parameters must be considered to account for non-equilibrium flow effects. Based on the experimental results and on the vibrational non-equilibrium CFD model, we reason that these additional parameters are $\Gamma = \tau_{vib}/\tau_{res}$, and ϵ_{vib}/ϵ, the ratio of vibrational energy to overall internal energy. The first parameter, Γ, determines if vibrational non-equilibrium effects are present in the flow field. The limiting values of this parameter range from zero (*i.e.,* equilibrium flow) to infinity (*i.e.,* frozen flow), where intermediate values give an indication of how far the flow is from equilibrium. The second parameter, ϵ_{vib}/ϵ, measures the importance of non-equilibrium effects (if they are present) in the flow field.[1] When these additional parameters are considered, non-equilibrium effects can be characterized for all gas species over all flow conditions.

All analysis in this investigation were done for a limited range of temperatures, pressures, and nozzle sizes. Vibrational non-equilibrium would be more important at elevated temperatures given that the contribution of the vibrational energy to the overall internal energy increases. For gases that have non-negligible vibrational energy levels, relaxation phenomenon will be an issue for values of Γ close to (or greater than) unity. Physically, this condition is most likely to occur for small throat diameter ISO nozzles when they are calibrated at low stagnation pressures.

[1] Here it is important that the energy datum is taken to be the energy of the molecule at absolute zero (*i.e.,* the zero-point energy).

REFERENCES

[1] Baker, J., "Chemical Handling Management," *Flow Control Network*, March 1996, 14-20.

[2] Reif, D., "Matching the Flowmeter to the Job," *Flow Control Network*, May 1997, 31-35.

[3] Bridge, S., "An Assessment of the Global Market for Flowmeters," *Flow Control Network*, January 1998, 12-16.

[4] Athane, B., "Implications of Legal Metrology in Flow Measurement for the Utilities," *Flow Measurement and Instrumentation*, November 1994, Vol. 5, 67-69.

[5] Espina, P., I., "Tele-Calibration of Gas Flow Meters," *Proceedings of the 1999 Measurement Science Conference*, Anaheim, CA: MSC 1999.

[6] Athane, B., "Flowmeter Standards and the Holy Grail of Good Data," *Flow Measurement and Instrumentation*, September 1997.

[7] Athane, B., "The Traceability Question," *Flow Measurement and Instrumentation*, October 1997, 14-22.

[8] "ISO International Vocabulary of Basic and General Terms in Metrology," Published by the International Standards Organization, P.O. Box 56, Geneva, Switz, 1984

[9] Jongerius P. F. M., Beek M. P. V. D. , Grinten, J. G. M. V. D. , "Calibration Facilities for Industrial Gas Flow Meters in the Netherlands," *Flow Measurement and Instrumentation*, November 1993, 77-84.

[10] Wright, J. D., and Mattingly, G. E., "NIST Calibration Services For Gas Flow Meters: Piston Prover and Bell Prover Gas Flow Facilities," *NIST SP 250-49,* 1998.

[11] Todd, D. A., "NPSL Method for Calibrating Bell Provers," *Technical Report: Navy Primary Standards Laboratory Code 4.1.4.5.0,* 1996.

[12] Olsen, L. and Baumgarten, G., "Gas Flow Measurement by Collection Time and Density in a Constant Volume, Flow: Its Measurement and Control in Science and Industry," *ISA*, (1971), pp. 1287 - 1295.

[13] Brain T. J. S., Macdonald, L. M., "Evaluation of the Performance of Small Scale Critical Flow Venturis Using the NEL Gravimetric Gas Flow Standard," *Technical Paper: B-3.*

[14] Coleman, H. W., and Steele, W. G., "Experimentation and Uncertainty Analysis for Engineers," *John Wiley and Sons,* 1989.

[15] Wright, J. D., "The Long Term Calibration Stability of Critical Flow Nozzles and Laminar Flowmeters," *NCSL Conference Proceedings*, Albuquerque, NM., (1998), 443-462.

[16] Takamoto, M., Ishibashi, M., Wantanabe, N., Aschenbrenner, A., and Caldwell, S. "Intercomparison Tests of Gas Flow Rate Standards," *Proceedings of the 6th International Conference on Flow Measurement*, Seoul, Korea, October 1993, pp. 75-82.

[17] Mattingly, G. E., "Round-Robin Mass Flow Controller Gas Flow Calibration Test Results Using the NIST-SEMATECH-MARK 1 Gas Flow Measurement Artifact: Final Report," *Tech. Transfer No. 93051631A-ENG, SEMATECH*, Austin, TX, 1993.

[18] Wright, J. D., Mattingly, G. E., Nakao, S. Yokoi, Y., and Takamoto, M., "Intercomparison Tests of NIST Primary Standard with NRLM Transfer Standard for Small Mass Flow Rates of Nitrogen Gas," *Metrologia*, 1998, Vol. 35, pp. 211-221.

[19] Wright, P. H., "The application of sonic nozzles to the automated accuracy testing of gas flow meters," *Proc. International Conference on Flow Measurement*, Australia 1985, 152-156.

[20] Aschenbrenner, A., "A Test Stand for Large-Scale Gas Meters with Supercritical Nozzles as Standard Instrument," *PTB Bericht*, PTB-Me-24 October 1979.

[21] Johnson, R. C., "Calculation of Real-Gas Effects in Flow Through Critical-Flow-Nozzles," *ASME Paper 63-WA-71*, 1963.

[22] Johnson, R. C., "Calculations of Real-Gas Effects in Flow Through Critical Nozzles," *Journal of Basic Engineering*, September 1964, pp. 519.

[23] Johnson, R. C., "Real-Gas Effects in Critical-Flow-Through Nozzles and Tabulated Thermodynamic Properties," *Nasa Technical Note D-2565*, National Aeronautics and Space Administration, Washington, D.C., January 1965.

[24] Johnson, R. C., "Real-Gas Effects in Critical Flow Through Nozzles and Thermodynamic Properties of Nitrogen and Helium at Pressures to $300x10^5$ Newtons Per Square Meter (Approx. 300 atm)," *Nasa Technical Note SP-3046*, National Aeronautics and Space Administration, Washington, D.C., 1968.

[25] Johnson, R. C., "Real Gas Effects in Flowmetering," *Symposium on Flow*, ISA, Pittsburgh, PA, 1971.

[26] Stratford, B. S., "The Calculation of the Discharge Coefficient of Profiled Choked Nozzles and the Optimum Profile for Absolute Air Flow Measurement," *Journal Royal Aeron. Soc.*, Vol. 68, No, 640, April 1964.

[27] Masure, B., "Study of the precision of Measurement of Gas Flow Rates by the Sonic Nozzle Method," *National Aeronautics and Space Administration N69-29669,* June 1969.

[28] Hall, I. M., "Transonic Flow in Two-Dimensional and Axially-Symmetric Nozzles," *Quart. J. Mech. and Applied Math*, Vol. XV, Pt. 4, pp. 487–508, 1962.

[29] Smith, R. E., Matz, R. J., "A Theoretical Method of Determining "Discharge Coefficients for Venturis Operating at Critical Flow Conditions," *Journal of Basic Engineering*, 1962, pp. 434-446.

[30] Tang, S. P., "Theoretical Dependence of the Discharge Coefficients of Axisymmetric Nozzles under Critical Flows," *Technical Report PR-118-PU,* Department of Mechanical Engineering, Princeton Univ., 1969.

[31] Tang, S., "Discharge Coefficients for Critical Flow Nozzles and Their Dependence on Reynolds Numbers," *Ph.D. Thesis*, Princeton Univ., 1969.

[32] Massier, P., F., Back, L. H., Noel, M. B., and Saheli, F., "Viscous Effects on the Flow Coefficient for a Supersonic Nozzle," *AIAA Technical Note,* March 1970, pp. 605-607.

[33] Geropp, D., "Laminare Grenzschichten In Ebenen Und Rotationssymmetrischen Lavalduesen," *Deutsche Luft- Und Raumfart, Forschungsbericht*, pp. 71-90, 1971.

[34] Ishibashi, M., Takamoto, M., "Very Accurate Analytical Calculation of the Discharge Coefficients of Critical Venturi Nozzles with Laminar Boundary Layer," *Proceedings of the FLUCOME*, Hayama, Japan, Sept. 1–4, 1997.

[35] Nakao, S., Hirayama, T., and Takamoto, M., "Effects of Thermalphysical Properties of Gases on the Discharge Coefficients of the Sonic Venturi Nozzle," *Proceedings of the 1997 ASME Fluids Engineering Division Summer Meeting*, Vancouver, British Columbia, Canada, June 22–26, 1997.

[36] Hillbrath, S. H., "The Critical Flow Venturi: An Update," *Technical Report*, The Boeing Company, Seattle, Washington, pp. 407-420.

[37] Arnberg, B.T., Britton, C.L., and Seidl W. F., "Discharge Coefficient Correlations for Circular–Arc Venturi Flowmeters at Critical (Sonic) Flow," *ASME Journal of Fluids Engineering*, June, 1974.

[38] White, F. M., "Viscous Fluid Flow," McGraw-Hill, Inc., 1991.

[39] ISO 9300: 1990 (E)., "Measurement of Gas Flow by Means of Critical Flow Venturi Nozzles," Geneva, Switz., 1990.

[40] John, J. E., "Gas Dynamics," *Allyn and Bacon, Inc, 2nd edition,* Boston, 1984.

[41] Anderson, J. D. Jr., "Modern Compressible Flow with a Historical Perspective," *McGraw-Hill, Inc,* New York, 1982.

[42] Shapiro, A. H., "The Dynamics and Thermodynamics of Compressible Fluid Flow," *Vol. II, The Ronald Press Co.,* New York, 1954.

[43] Kuluva N. M., Hosack G. A., "Supersonic Nozzle Discharge Coefficients at Low Reynolds Numbers," AIAA Journal, Vol. 9, 1971, pp. 1876-1879.

[44] Merkle, C. L., Yu S., "Computational Fluid Dynamics of Inviscid and High Reynolds Number Flows," 1996.

[45] Buelow, P., Venkateswaran, S., and Merkle, C. L., "The Effect of Grid Aspect Ratio on Convergence," AIAA Journal, Vol. 32, 1994, pp. 2401-2406.

[46] Feng, J., and Merkle, C. L., "Evaluation of Preconditioning Methods for Time Marching Systems," AIAA Paper 90-0016, AIAA 28th Aerospace Sciences Meeting, Reno, NV. 1990.

[47] Buelow, P. E. O., "Convergence Enhancement of Euler and Navier-Stokes Algorithms," PhD thesis, Department of Mechanical Engineering, 1995, The Pennsylvania State University, University Park, PA.

[48] Hirsch, C., "Numerical Computation of Internal and External Flows: Volume 1, Fundamentals of Numerical Discretization," *John Wiley & Sons, Inc.*, New York, NY., 1988.

[49] Bhatia A. B., "Ultrasonic Absorption: An Introduction to the Theory of Sound Absorption and Dispersion in Gases, Liquids, and Solids," *Oxford University Press, Inc, London W.*, New York, NY., 1967.

[50] O'Connor L. C., "Thermal Relaxation of Vibrational States in Sulfur Hexafluoride," *The Journal of the Acoustical Society of America*, Volume 26, May, 1954.

[51] Kinsler, L. E., Austin F. R., Alan A. B., and Sanders J. V., "Fundamentals of Acoustics 3rd ed," *John Wiley & Sons, Inc.*, New York, NY., 1982.

[52] Landau, L., and Teller, E., "Zur Theorie der Schalldispersion," *Physik Z. Sowjetunion*, b. 10, h.1, (1936), p. 34.

[53] Kruger, C.H., Walter G.V., "Introduction to Physical Gas Dynamics," *John Wiley & Sons, Inc.*, New York, NY., 1965.

[54] Estrada-Alexanders, A. F., and Trusler, J. P. M., "Speed of sound in $(0.4C_2H_6 + 0.6CO_2)$ at temperatures between T = 22O K and T = 450 K and pressures up to P = 1.2 MPa," *The Journal of Chemical Thermodynamics*, Volume 31, No. 5, May 1999.

[55] Breshears, W. D., and Blair, L. S., "Vibrational relaxation in polyatomic molecules: SF_6," *The Journal of Chemical Physics*, Volume 59, No. 11, December, 1973.

[56] Hilsenrath, J., Beckett, C. W., Benedict, W. S., Fano, L., Hoge, H. J., Masi, J. F., Nuttall, R. L., Touloukian, Y. S., Wooley, H. W., "Tables of Thermal Properties of Gases," *U.S. Department of Commerce NBS Circular 564*, 1955.

[57] Hurly, J. J., Defibaugh, R. D., Moldover, M., "Thermodynamic Properties of Sulfur Hexafluoride," *Nist Technical Publication*, Volume ??, No. ??, December, 19??.

[58] Edwards, C. H., and Penny, D. E., "Elementary Differential Equations With Boundary Value Problems," *Prentice-Hall*, Inc., Englewood, NJ., 1989.

[59] DuChateau, P., and Zachmann, D., "Applied Partial Differential Equations," Harper and Row Publishers, Inc. 1989.

[60] Dymond, J., H., and Smith, E., B., "The Virial Coefficients of Pure Gases and Mixtures; A Critical Compilation," *Clarendon Press*, Oxford, 1980.

[61] Callen, H., C., "Thermodynamics and an Introduction to Thermostatistics," *John Wiley and Sons Inc.*, N.Y., 1985.

[62] Arnberg, A., B., and Seidl, W., F., "A comparison of Errors in Four Methods for Determining Critical Flow Functions for Sonic Flow Nozzles and Venturis," *Proceedings of ASME Fluids Engineering Division Summer Meeting*, June 11-15, 2000, Boston, Massachusetts.

[63] Johnson, A. N., Espina, P. I., Mattingly, G. E., Wright, J. D., Merkle, C. L. "Numerical Characterization of the Discharge Coefficient in Critical Nozzles," *Proceedings of the 1998 NCSL Workshop Symposium*, Albuquerque, NM: NCSL 1998.

[64] Lambert, J. D., "Vibrational and Rotational Relaxation in Gases," *Clarendon Press*, Oxford, Great Britain, 1977.

[65] Wegener, P. P., "Non-Equilibrium Flows, Part 1," *Marcel Kekker, inc.*, New York, NY, 1969.

[66] Herzfeld, K. F., and Litovitz. T. A., "Absorption and Dispersion of Ultrasonic Waves" *Academic Press, Inc.*, New York, NY., 1959.

[67] Aschenbrenner, A., "The influence of Humidity on the Flowrate of Air through Critical Flow Nozzles," *FLOMEKO*, (1983), pp. 61-64.

[68] Stasa, F. L., "Applied Finite Element Analysis for Engineers," *CBS College Publishing*, New York, NY., 1985.

[69] Davis, D. F., Snider, A. D., "Introduction to Vector Analysis, Sixth Edition," *Wm. C. Brown Publishers*, Dubuque, IA., 1991.

Appendix A

INTEGRATION OF THE VIBRATIONAL RATE EQUATION

The numerical procedure used to integrate the vibrational rate equation is explained in this section. We begin with the Eulerian representation of the vibrational rate equation as given by

$$\frac{\partial \epsilon_{vib}}{\partial t} + u_j \frac{\partial \epsilon_{vib}}{\partial x_j} = \frac{\epsilon_{vib}^{eq} - \epsilon_{vib}}{\tau_{vib}} \tag{A.1}$$

where u_j is the local flow velocity, $\tau_{vib}(P,T)$ is the vibrational relaxation time (*i.e.,* a function of temperature and pressure), $\epsilon_{vib}^{eq}(T)$ is the equilibrium vibrational energy (*i.e.,* a function of temperature), and ϵ_{vib} is the non-equilibrium vibrational energy. The partial differential equation represented by Eq. (A.1) can be transformed into an ordinary differential equation if the flow is steady and the equation is evaluated along flow streamlines as given by [69]

$$\Gamma \frac{d\epsilon_{vib}}{dz} + \epsilon_{vib} = \epsilon_{vib}^{eq} \tag{A.2}$$

where $\Gamma = \tau_{vib}/\tau_{res}$ is the ratio of vibrational relaxation time to flow residence time, $\tau_{res} = L/||\vec{u}||$ is the flow residence time, L is a characteristic distance along a streamline, $||\vec{u}|| = \sqrt{u_x^2 + u_r^2}$ is the magnitude of fluid velocity, and $z = s/L$ is the dimensionless distance along a streamline.

In order to solve the first order, non-homogeneous ordinary differential equation

represented by Eq. (A.2), the coefficient in front of the derivative on the left hand side, Γ, and the source term on the right hand side, ϵ_{vib}^{eq}, must first be determined. These parameters are functions of the gas dynamic flow variables (*i.e.,* the pressure, the temperature, and the flow velocity). Therefore, to determine these parameters the Navier-Stokes equations must be solved simultaneously in an iterative manner along with the vibrational rate equation. The coupling between the Navier-Stokes equations and the vibrational rate equation has already been discussed previously in Chapter 2, but the iterative solution procedure is summarized again in this section for completeness.

The solution procedure begins by initializing the flow field with an appropriate velocity, pressure, temperature, and molecular vibrational energy field. Following this initialization step the iterative process begins. The gas dynamic variables (*i.e.,* the pressure, the temperature, and the velocity field) are updated using an implicit time marching Navier-Stokes algorithm. Using the computed velocity field, the streamlines are calculated and the existing grid system is adapted to a streamline oriented grid system having grid lines that coincide with the calculated streamlines. Additionally, the pressure and temperature computed from the Navier-Stokes algorithm are used to evaluate the parameters Γ and ϵ_{vib}^{eq} throughout the flow field. Next, the vibrational rate equation as given in Eq. (A.2) is integrated on the streamline oriented grid system to determine an updated value for the molecular vibrational energy, ϵ_{vib}. The updated molecular vibrational energy is used in conjunction with the molecular translational

and rotational energy to update the overall internal energy, and the Navier-Stokes equations are resolved for the next iteration. This iterative procedure is repeated until both the Navier-Stokes equations and the vibrational rate equation are simultaneously satisfied on the resulting streamline oriented grid system.

The details outlining the numerical procedure for solving the Navier-Stokes are given in Chapter 2. Thus, in this section attention is focused on outlining the numerical procedure used for estimating the solution of the vibrational rate equation. The procedure begins by modifying the exact global representation of the vibrational rate equation given by Eq. (A.2), with an approximate formulation defined on a sub interval (*i.e.*, finite element) between node "i" and node "$i+1$" as given by

$$(\Gamma_i + \Delta\Gamma_i z)\frac{d\epsilon_{vib}^{el_i}}{dz} + \epsilon_{vib}^{el_i} = \epsilon_{vib_i}^{eq} + \Delta\epsilon_{vib_i}^{eq} z$$

$$\epsilon_{vib}^{el_i}(0) = \epsilon_{vib_i} \tag{A.3}$$

$$0 \leq z \leq 1$$

where the superscript "el_i" indicates the "i^{th}" finite element and the following definitions apply, $\Delta\Gamma_i \equiv \Gamma_{i+1} - \Gamma_i$ and $\Delta\epsilon_{vib_i}^{eq} \equiv \epsilon_{vib_{i+1}}^{eq} - \epsilon_{vib_i}^{eq}$ respectively. The variation in ϵ_{vib}^{eq} and Γ across an element is approximated by the following linear interpolation functions, $\epsilon_{vib}^{eq} = \epsilon_{vib_i}^{eq} + \Delta\epsilon_{vib_i}^{eq} z$ and $\Gamma = \Gamma_i + \Delta\Gamma_i z$ respectively. The local boundary condition for each element is determined from the calculated molecular vibrational energy at the end of the previous element. At the nozzle inlet, however, the molecular

vibrational energy is taken to be in thermodynamic equilibrium so that it can be determined from the inlet temperature using Eq. (2.14) from Section 2.4.2 of Chapter 2.

By using the linear interpolation functions the approximate vibrational rate equation given by Eq. (A.3) can be solved analytically using the method of variation of parameters [58] over each finite element. The solution to Eq. (A.3) for the i^{th} element is given by

$$\epsilon_{vib}^{el_i}(z) = c_0 + c_1 z - c_0 \left[1 + \frac{\Delta\Gamma_i z}{\Gamma_i}\right]^{(-\frac{1}{\Delta\Gamma_i})}$$
$$0 \leq z \leq 1 \tag{A.4}$$

where

$$c_0 = \epsilon_{vib_i}^{eq} - \frac{\Delta\epsilon_{vib_i}^{eq}\Gamma_i}{1+\Delta\Gamma_i}$$

$$c_1 = \frac{\Delta\epsilon_{vib_i}^{eq}}{1+\Delta\Gamma_i}$$

The value of the molecular vibrational energy at nodal points $i=1$ to i_{max} is then given by

$$\epsilon_{vib_1} = \epsilon_{vib_1}^{eq}$$

$$\epsilon_{vib_2} = \epsilon_{vib}^{el_2}(0)$$

$$\vdots$$

$$\epsilon_{vib_i} = \epsilon_{vib}^{el_i}(0)$$

$$\vdots$$

$$\epsilon_{vib_{i_{max}}} = \epsilon_{vib}^{el_{i_{max-1}}}(1)$$